Biomass Conversion Strategies and the Renewable Production of Hydrogen using Heterogeneous Metal Catalysts

By

Ronald Carrasquillo-Flores

A dissertation submitted in partial fulfillment of

the requirements for the degree of

Doctor of Philosophy

(Chemical Engineering)

at the

UNIVERSITY OF WISCONSIN-MADISON

2015

Date of final oral examination: July 28, 2015

The dissertation is approved by the following members of the Final Oral Committee:

James A. Dumesic, Professor, Chemical and Biological Engineering

Manos Mavrikakis, Professor, Chemical and Biological Engineering

Thatcher Root, Professor, Chemical and Biological Engineering

Thomas F. Kuech, Professor, Chemical and Biological Engineering

Ive Hermans, Associate Professor, Chemistry

Biomass Conversion Strategies and the Renewable Production of Hydrogen using Heterogeneous Metal Catalysts

Ronald Carrasquillo-Flores

Under the supervision of Professors James A. Dumesic and Manos Mavrikakis
At the University of Wisconsin – Madison

Biomass is a renewable carbon source that can be processed into fuels and chemicals in a biorefinery. However, there are a number of challenges that need to be overcome for biomass utilization to be viable. The work presented herein aims to address two existing challenges in biomass processing schemes namely the efficient utilization of all fractions of lignocellulosic biomass and the renewable production of the hydrogen necessary to reduce the oxygen functionalities native in biomass.

First, lignin was depolymerized using a Pd/C catalyst to produce a phenolic solvent mixture composed primarily of propyl guaiacol and propyl syringol. This solvent in contact with aqueous solutions of furanic compounds was efficient in partitioning the furan molecules into the organic phase. Biphasic reactions were performed with this solvent and aqueous solution of glucose or xylose to produce 5-hydroxymethylfurfural (HMF) and furfural, respectively, at high yields. Using biphasic reactors, HMF and furfuryl alcohol could also be upgraded into levulinic acid at high yields. The observed yields are due to the capacity of the solvent to partition these molecules and prevent their degradation. Second, propyl guaiacol, a component of the lignin-derived solvent, was used for biphasic reactions where ball milled biomass substrates were used. Ball milling of the biomass produces oligomers of the C5 and C6 sugars which produce xylose and glucose, respectively, when heated a mineral acid solution. These oligomers can be

converted to furfural and HMF at high yields due to the high partition of these molecules afforded by the solvent and the on-demand production of glucose and xylose from the oligomers, both of which prevent the formation of humins.

Several studies were performed using heterogeneous catalysts in reactions that can produce hydrogen. A study of the water-gas shift reaction over Pt-based catalysts was conducted. Alloying Pt with Re was found to increase the catalytic activity and microkinetic modeling revealed Pt is a good representation of the active site and Re acts as a promoter slightly destabilizing CO binding. The reaction proceeds through a carboxyl species and the rate-controlling step is water activation. A study on the decomposition of formic acid over Au catalysts was performed. Based on experimental, density functional theory and microkinetic modeling results it was found that the reaction proceeds completely on highly undercoordinated Au atoms with any high coordination atom being largely inert.

Motivated by the results on Au catalysts, the metal-support interaction was investigated for the reverse water-gas shift reaction. Using a combination of infrared spectroscopy, Raman spectroscopy, x-ray absorption spectroscopy, electron microscopy and reaction kinetics measurements it was found that the deposition of an organometallic molybdenum compound occurs at the undercoordinated Au sites to produce interfacial sites that are an order of magnitude more active than Au sites and activate water.

Approved by _____

Professor James A. Dumesic

Approved by _____

Professor Manos Mavrikakis

Date _____

Acknowledgments

The writing of this work marks the culmination of a series of events that have been made possible through the help, collaboration and support of many individuals. I would like to begin by thanking Professor Dumesic and Professor Mavrikakis. Your tireless mentoring, guidance, dedication and unique approaches to research have truly changed me for the better and I have no doubt that I would not have been able to make it this far without both of you. I am forever in your debt for the opportunity to work and learn from the best in the field and to be part of your research lineage.

I would like to thank the past and present Dumesic and Mavrikakis research group members for their support and enlightening conversations. Elif Gürbüz, David Martin Alonso and Yomaira Pagan-Torres deserve particular praise for their patience during my training. I would also like to thank Gretchen, Ricky, Tom, Stephanie, Mrunmayi, Yifei, Ali, Mark, Mei, Jean, Sikander, Max, Zach, Tom G., Brandon, Jesse, Madelyn, Ana, Tony, Yunhai, Jeff, Canan, Sha, Insoo, Duygu and Suyash for the many conversations and collaborations. I would also like to thank the undergraduates Thejas and Zuleika.

In the Chemical Engineering Department I would like to thank Professor Root for his mentoring during my teaching assistantship. Judy Lewison in particular deserves many thanks for being the “unseen” gear that keeps the group running both with her culinary skills and financial knowledge.

Outside of the University of Wisconsin – Madison I would like to thank Professor Rinaldi for being my research advisor and great friend during my research experience in Germany. I greatly appreciate the effort your entire research group put forth to make me feel at home during my stay and your continued help after my return. Professor Cardona

and Professor Suarez deserve special thanks for giving me the opportunity to take my first steps into research work and their guidance on the topic of graduate school.

Rafael Rivera deserves special thanks. We have been great friends for many years and have experienced the “pain” of education together and supported one another through what seemed an endless road.

My family has been instrumental in my education and I want all of you to know that my accomplishments have been enabled by your contributions. My grandmother Virgen has been a second mother to me and I am truly blessed to be your grandson. My grandfather Angel has been gone for a few years now and I hope that I have made him proud. I miss you and will forever remember you. My sisters, Michelle and Nancy, have always been there to support me and I could search the world and never find sisters as special as both of you. My nephews and niece, Kaled, Alexis, Derek and Valentina, are miracles in my life and I treasure all the moments I spend with you. I am truly blessed for having both of my parents, Nancy and Arnaldo, with me. As an adult I now understand all the sacrifices you have made and you are the best examples of dedication, hard work and unconditional love. I love you and thank you.

Finally, behind every great man there is a great woman. I am by no means implying to be a great man but I am sure Selby, my fiancée, is a great woman. Your love and support have been constants during our time together. You understand me better than I do myself and you make me a better man every day I am with you. You are a beautiful person and I am the luckiest man to be able to share my life with you. Thank for your patience and understanding and I look forward to our future with excitement.

- Ronald

To Selby

Table of Contents

List of Figures

List of Tables

Chapter 1: Introduction

1.1 Introduction

The field of catalysis has been instrumental to the development of society as we know it today. The chemical industry in all its forms is dependent on catalytic processes and it is widely recognized that over 90% of all chemical products have at least one catalytic step involved in their manufacture.[1] Today, non-renewable fossil sources of carbon are the preferred feedstocks in the production of the abovementioned chemicals where the vast majority of organic chemicals are produced from the systematic upgrading of key platform chemicals derived from petroleum or natural gas.[2] Over time the increased utilization of these fossil resources has highlighted their finite character and their direct role in the increase in greenhouse gases, making them less attractive from an economic and environmental point of view and ill suited for long-term use. [3-5] While proven reserve estimates change year to year,[6] they provide an approximate timeline for the development of alternative technologies capable of providing sustainable carbon that can initially alleviate and later replace our dependence on fossil resources.

There exist a number of alternative energy technologies including nuclear, hydro, wind and solar all of which are both currently in use and under development for the production of electricity.[7] However, none of these sources can provide the necessary carbon for the production of chemicals and transportation fuels. In this regard, research on biomass has shown its upgrading into platform chemicals, ideologically the same strategy used in the current chemical industry, as a promising alternative to the current energy quandary being both carbon neutral and able to provide renewable carbon.[3, 8, 9] Alternatives such as atmospheric CO_2 capture and its upgrading are available but as it

stands these methods are far off from implementation,[10] leaving biomass as the sole option which we can realistically pursue at this moment.[11]

When we consider biomass it is possible to denote three categories of feedstocks that are appropriate for the production of renewable chemicals and fuels:[12] starches (including sugars), triglycerides and lignocellulosic feedstocks. The main repeating structure for each of these is shown in Figure 1.1 Starches are polymers of glucose connected by α-glycosidic bonds. Starches are found in a variety of food crops including corn, wheat, root vegetables and sugar cane. The α-glycosidic bonds in starch are relatively easy to hydrolyze thereby producing sugar monomers that can be further processed to yield bioethanol. Triglycerides are made up of a glycerol backbone that has three glycerol units connected by ester bonds. Triglycerides can be derived from plant sources such as algae and soybeans, but also from waste oil (*e.g.* yellow grease, trap grease). Using an alcohol it is possible to esterify the fatty acid portion of triglycerides to produce biodiesel.[12] Both of these types of biomass are only available in limited quantities and their large-scale use would lead to similar reserve issues as with fossil resources. In addition, their use for fuel production competes with food production and brings about further complications.

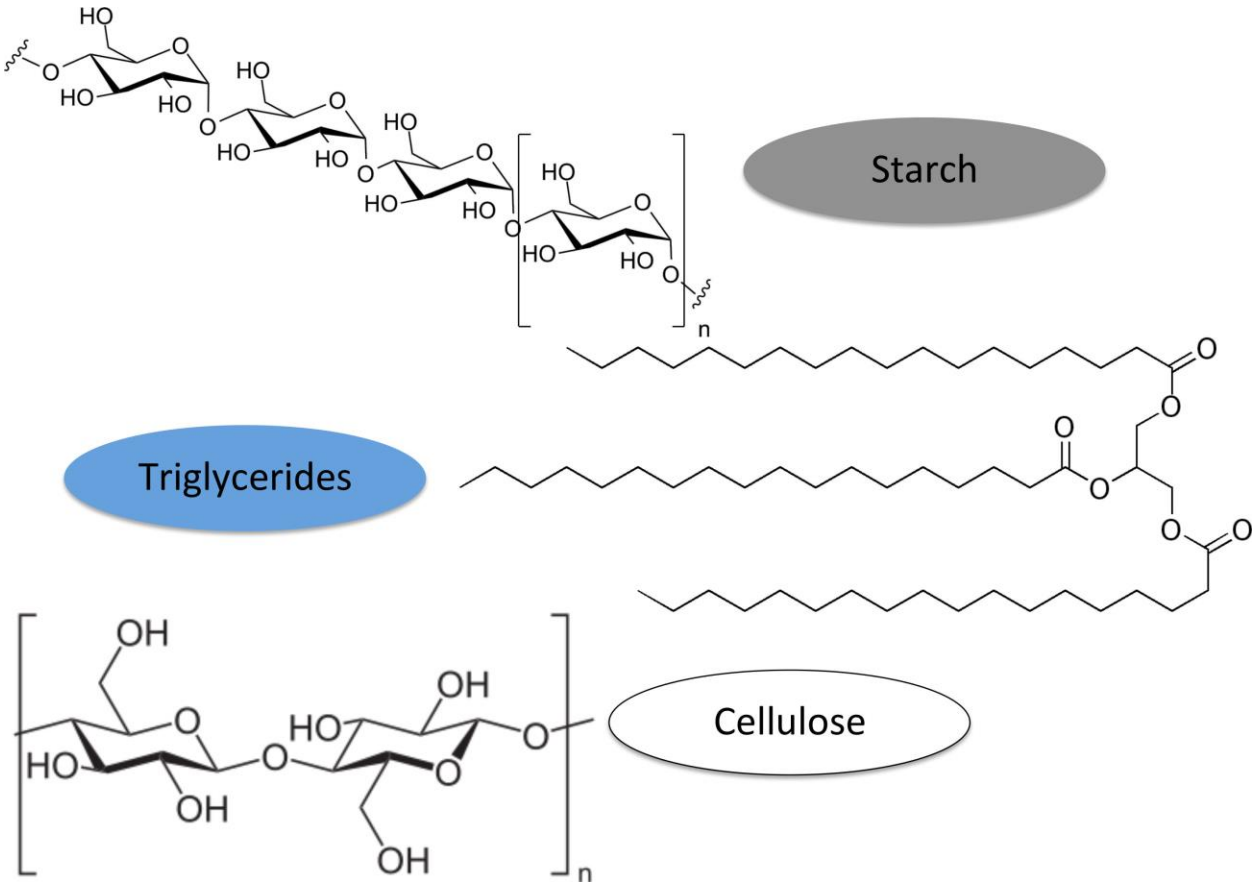

Figure 1.1. Chemical structure of biomass feedstocks.

Lignocellulosic biomass, different from starches and triglycerides, is present in all plant matter and is therefore the most abundant class of biomass. It is composed of three different fractions: cellulose (40-50%), hemicellulose (25-35%), and lignin (15-20%).[13] Figure 1.2 shows the main repeating units for the three fractions. Cellulose is a linear polymer of glucose linked by β-glycosidic bonds and imparts rigid crystallinity that impedes hydrolysis.[4] Hemicellulose is an amorphous polymer composed of five and six carbon sugar monomers with the predominant monomer being the five carbon monomer, xylose.[4] Hemicellulose is found bound to lignin, and strands of cellulose are interlaced with hemicellulose. Lignin is an amorphous polymer composed of methoxylated phenylpropane structures, such as coniferyl alcohol, sinapyl alcohol and coumaryl

alcohol.[14, 15] It provides structural integrity to the plant and a hydrophobic vascular system to transport water and solutes.[14] For the purpose of producing fuels and chemicals, lignocellulosic biomass can be grown as an energy crop or obtained in large amounts as a waste product from agricultural, municipal and wood processing.[13, 16, 17]

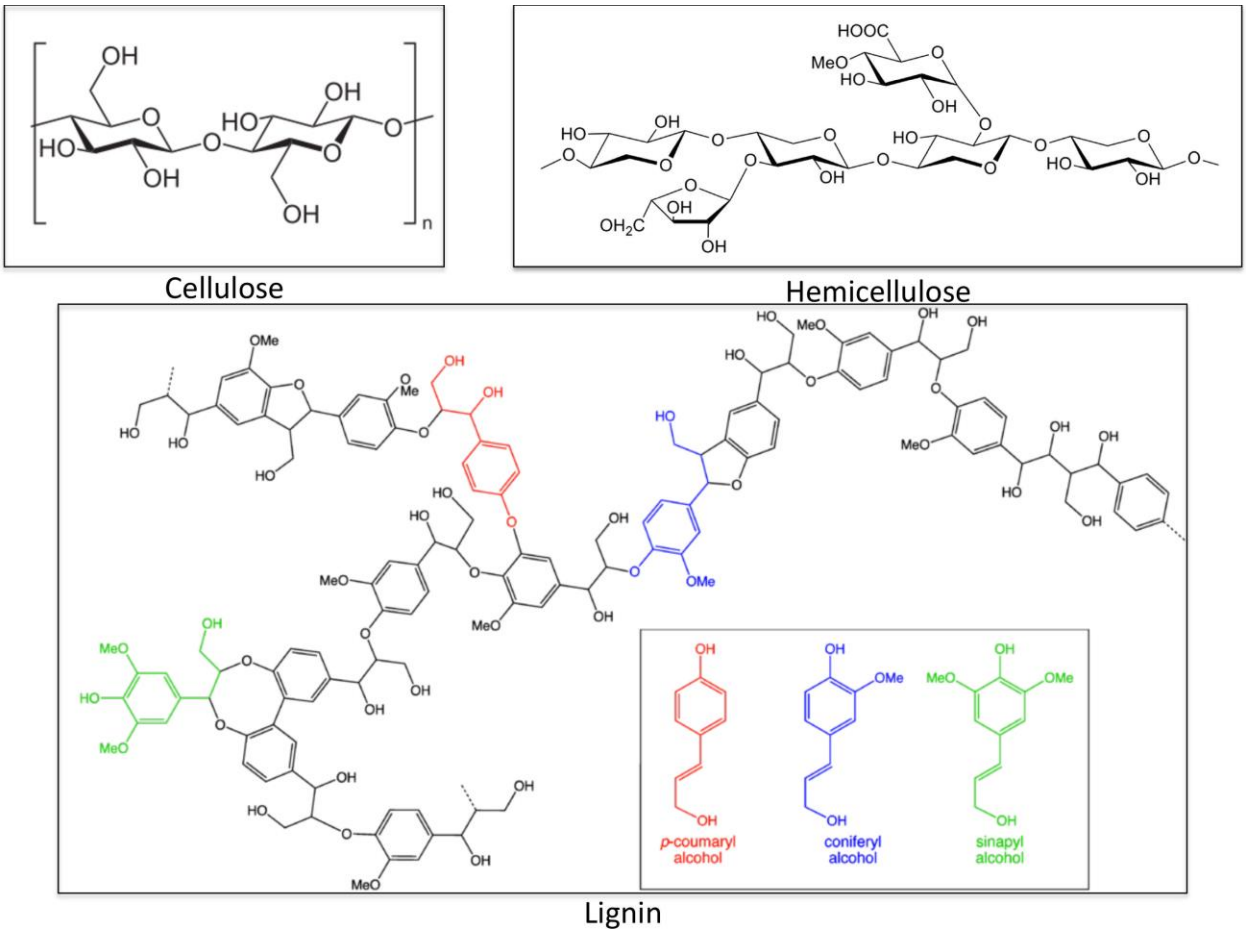

Figure 1.2. Representative structures of the components of lignocellulosic biomass.

Current strategies in petrochemical refineries are based on fractionation of the crude feedstock and upgrading into different grades of fuels and chemicals with a significant portion of the chemical transformations focused around (reword) platform chemicals. In order to fit into the current infrastructure, be economically and technically viable, a biorefinery would need to operate in a similar fashion.[18] That is lignocellulosic

biomass would need to be fractioned into defined segments so that these are later selectively upgraded into platform molecules. While a number of different strategies are available for the conversion of lignocellulosic biomass in a biorefinery setting, they can be grouped into two general categories: 1) thermochemical and 2) hydrolysis. Thermochemical approaches such as pyrolysis, gasification and liquefaction rely on heating up whole biomass to elevated temperatures to produce liquid and gas products. These have the advantage of being relatively simple and inexpensive but generally are not selective in terms of the native functionalities present in biomass and are prone to carbon losses from char formation.[19, 20] On the other hand, hydrolysis takes advantage of the different physical and chemical properties of the native fractions of lignocellulosic biomass (cellulose, hemicellulose and lignin) by separating them into relatively pure streams that can be individually processed at operating conditions that are optimal for a given chemical reaction. This process is certainly more involved and expensive, largely due to the deconstruction step, than those in the thermochemical category but has the advantage of higher flexibility and selectivity to high-value products.[21] For example, it is possible to use physical methods (e.g. milling,[22-26] steam[27, 28]) and chemical methods (e.g. aqueous-phase acid or base hydrolysis[13]). Moreover, it is possible to incorporate biological and chemical upgrading methods,[29] or to utilize a fraction of the biomass such as hemicellulose to produce fuels and chemicals while preserving the cellulose fraction for pulp and paper applications.[30] A recent scheme for a biorefinery process is shown in Figure 1.3 where biomass is deconstructed into the cellulose (C6) and hemicellulose (C5) fractions and processed in discrete steps into chemicals and, if desired, fuels.[21, 31]

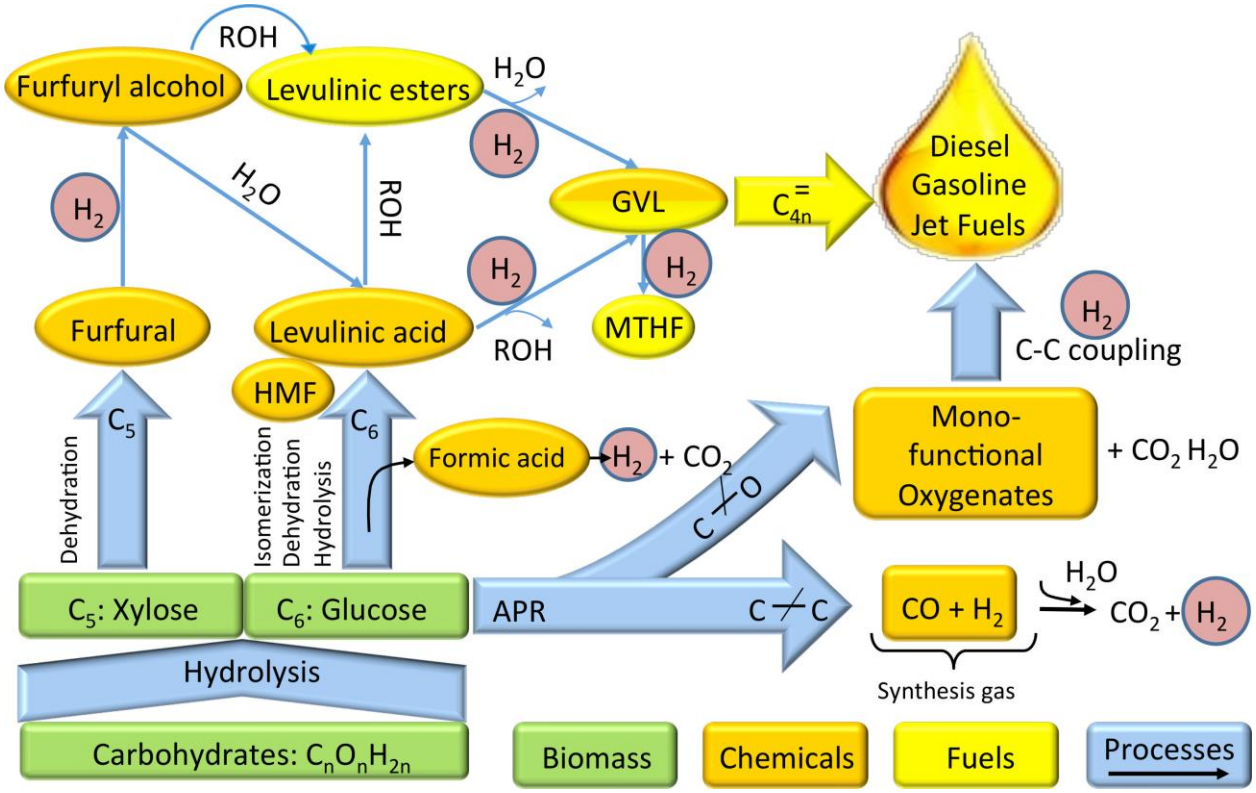

Figure 1.3. Biorefining scheme for the upgrading of lignocellulosic biomass into value-added platform chemicals and liquid fuels.

The successful establishment of a biorefinery based on either of these processing strategies depends on overcoming the economic and technical challenges associated with the supply and chemical transformation of the lignocellulosic biomass. As is often the case, these challenges exist intertwined and as such the largest economic drivers in biomass conversion: i) high product yields, ii) product concentration and iii) reaction rates are of a technical character.[13] In this regard, the use and development of catalysts and catalytic processes tailored to overcome these obstacles will be key in the realization of biorefining schemes.

Inspection of the roadmap presented in Figure 1.3 reveals that in the upgrading of the C5 and C6 fractions of biomass, hydrogen is a key reactant in a large number of the chemical transformations. In fact, the use of hydrogen to reduce the carbon to oxygen

ratio is prevalent through the majority of upgrading strategies and in order for any process to truly be sustainable it will be necessary to provide this hydrogen in a renewable fashion. Coincidentally, in this same strategy it is possible to produce hydrogen from the selective decomposition of formic acid (FA) and the water-gas shift reaction (WGS). The opportunity to harvest hydrogen from biomass itself is convenient yet it adds to the complexity of the problem as it will be necessary to develop the technology to both upgrade biomass into the desired fuels and chemicals and also extract the hydrogen in the biomass to enable the chemical transformations. Accordingly, the focus of this work will be on the development of catalysts and catalytic processes suitable for both of these tasks.

1.2 Research Direction

In the previous section an outline of previous advances in the field of biomass conversion were presented. In the following chapters, the work presented will aim to address the technical aspect of the challenges mentioned and each projects can be classified depending on its goal as: 1) strategies for the catalytic upgrading of biomass and 2) catalyst design and characterization for the production of renewable hydrogen in biomass processing schemes. In the first two chapters, advances in the catalytic depolymerization of lignocellulosic biomass to produce renewable solvents and the use of said solvents for selective biomass upgrading are described. In the following sections the nature of the active sites in monometallic and bimetallic catalysts for FA decomposition and the WGS reaction, respectively and the metal-support interaction for the reverse water-gas shift (RWGS) reactions are all described.

Chapter 2 will present an overview of the experimental/analytical methods employed throughout. Chapter 3 will explore the catalytic depolymerization of lignin to produce a renewable phenolic solvent mixture that can be employed to address the high yield upgrading of the C5 and C6 fractions using homogeneous and heterogeneous catalysts. The origin of the high selectivity will be investigated placing emphasis on the capacity of the solvent to partition the reactants and products shielding them from degradation. The stability and effectiveness of the solvent will be evaluated and compared to similar solvents derived from fossil-based feedstocks.

In Chapter 4 an alternative processing strategy for biomass upgrading will be covered. The experimental methodology aims to address the issue of selectivity during the upgrading of cellulose and hemicellulose by milling solid biomass (i.e. solid-state depolymerization) instead of performing aqueous phase hydrolysis. The solid-state reaction produces water-soluble oligosaccharides that are more reactive than cellulose and hemicellulose and readily undergo hydrolysis into monosaccharides. A phenolic solvent that can be derived from lignin, and was presented in Chapter 3, will be used to partition and protect the products from degradation after they are produced. In this regard, the selectivity observed will be related to the on-demand production of the monosaccharides and, as before, the capacity of the solvent to partition the reactants and products.

In Chapter 5, the origin of the catalytic activity in bimetallic catalysts will be investigated through the use of a PtRe alloy in the low-temperature WGS reaction. Experimental kinetic studies, density functional theory (DFT) calculations and microkinetic modeling will be combined to probe the contribution of multiple elementary

reactions and deduce the overall reaction pathway where the Pt to Re interaction is of critical importance to the catalytic activity. The information obtained sheds light into the nature of the active site for PtRe catalysts, the rate-limiting steps of the reaction on the studied catalysts and serves as the basis for the rational design of improved catalysts for this reaction.

In Chapter 6, the origin of the catalytic activity of Au catalysts will be studied in the context of the FA decomposition reaction. Similar to the approach in Chapter 5, a combined experimental and theoretical approach will be used to obtain information on the individual surface reaction contributions to the overall reaction. The results show that FA decomposition occurs selectively through the dehydrogenation pathway and that this reaction on Au is highly structure sensitive where only highly under-coordinated atoms of Au are able to perform the catalysis.

In Chapter 7 the disparity in activity between high coordination and low coordination Au atoms discussed in Chapter 6 is exploited to selectively deposit MoO_x moieties on the under-coordinated atoms. Raman spectroscopy, x-ray absorption spectroscopy, transmission infrared spectroscopy and reaction kinetics are used to probe the location of the Mo deposition and its effect on the catalytic activity. The resulting $AuMoO_x$ catalyst shows greatly increased catalytic activity for the RWGS reaction and serves as a platform to probe the metal-metal oxide interaction and quantify the catalytically active sites, metallic and interfacial, and their contribution to the catalytic activity.

In Chapter 8 a summary of the main conclusions from each research project will be presented. In addition, a possible direction for future work based on the most recent results obtained will be presented, laying out a potential roadmap for future researchers.

While each of the chapters presented will deal with a very specific set of challenges, it is important to keep in mind that the conclusions reached can be extended to other reaction systems where similar issues exist. While this statement can be applied to varying degrees on each project, it is especially true for the fundamental insight gained into the nature of the active sites of metal catalysts and the metal-metal oxide interactions where they should serve as a guide the rational design of improved catalysts.

1.3 References

1. J. G. de Vries and S. D. Jackson, *Catalysis Science & Technology*, 2012, **2**, 2009-2009.
2. B. J. Nikolau, M. Perera, L. Brachova and B. Shanks, *Plant Journal*, 2008, **54**, 536-545.
3. G. Huber, S. Iborra and A. Corma, *Chem. Rev.*, 2006, **106**, 4044-4098.
4. L. R. Lynd, J. H. Cushman, R. J. Nichols and C. E. Wyman, *Science*, 1991, **251**, 1318-1323.
5. Y. H. P. Zhang, *Journal of Industrial Microbiology & Biotechnology*, 2008, **35**, 367-375.
6. BP, *BP Statistical Review of World Energy*, 2014.
7. S. Chu and A. Majumdar, *Nature*, 2012, **488**, 294-303.
8. D. Alonso, J. Bond and J. Dumesic, *Green Chem.*, 2010, **12**, 1493-1513.
9. A. Corma, S. Iborra and A. Velty, *Chem. Rev.*, 2007, **107**, 2411-2502.
10. N. S. Lewis and D. G. Nocera, *Proceedings of the National Academy of Sciences of the United States of America*, 2006, **103**, 15729-15735.
11. P. Fornasiero and M. Graziani, *Journal*, 2011, 1 online resource (497 p.).
12. G. W. Huber and A. Corma, *Angewandte Chemie-International Edition*, 2007, **46**, 7184-7201.
13. C. E. Wyman, B. E. Dale, R. T. Elander, M. Holtzapple, M. R. Ladisch and Y. Y. Lee, *Bioresource Technology*, 2005, **96**, 1959-1966.
14. R. Vanholme, B. Demedts, K. Morreel, J. Ralph and W. Boerjan, *Plant Physiology*, 2010, **153**, 895-905.
15. F. Chakar and A. Ragauskas, *Ind. Crop. Prod.*, 2004, **20**, 131-141.
16. A. Aden and T. Foust, *Cellulose*, 2009, **16**, 535-545.

17. R. J. A. Gosselink, E. de Jong, B. Guran and A. Abacherli, *Industrial Crops and Products*, 2004, **20**, 121-129.
18. J. J. Bozell and G. R. Petersen, *Green Chemistry*, 2010, **12**, 539-554.
19. *Thermochemical Processing of Biomass:Conversion into Fuels, Chemicals and Power*, John Wiley & Sons, Ltd, 2011.
20. M. S. Mettler, D. G. Vlachos and P. J. Dauenhauer, *Energy & Environmental Science*, 2012, **5**, 7797-7809.
21. S. G. Wettstein, D. M. Alonso, E. I. Gürbüz and J. A. Dumesic, *Energy and environmental engineering / Reaction engineering and catalysis*, 2012, **1**, 218-224.
22. N. Meine, R. Rinaldi and F. Schuth, *Chemsuschem*, 2012, **5**, 1449-1454.
23. M. Kaldstrom, N. Meine, C. Farses, F. Schuth and R. Rinaldi, *Green Chemistry*, 2014, **16**, 4994-4994.
24. M. Kaldstrom, N. Meine, C. Fares, R. Rinaldi and F. Schuth, *Green Chemistry*, 2014, **16**, 2454-2462.
25. R. Carrasquillo-Flores, M. Kaldstrom, F. Schuth, J. A. Dumesic and R. Rinaldi, *Acs Catalysis*, 2013, **3**, 993-997.
26. J. Hilgert, N. Meine, R. Rinaldi and F. Schuth, *Energy & Environmental Science*, 2013, **6**, 92-96.
27. N. Mosier, C. Wyman, B. Dale, R. Elander, Y. Y. Lee, M. Holtzapple and M. Ladisch, *Bioresource Technology*, 2005, **96**, 673-686.
28. D. Montane, X. Farriol, J. Salvado, P. Jollez and E. Chornet, *Biomass & Bioenergy*, 1998, **14**, 261-276.
29. T. J. Schwartz, B. J. O'Neill, B. H. Shanks and J. A. Dumesic, *Acs Catalysis*, 2014, **4**, 2060-2069.
30. H. M. Li, A. Saeed, M. S. Jahan, Y. H. Ni and A. van Heiningen, *Journal of Wood Chemistry and Technology*, 2010, **30**, 48-60.
31. D. M. Alonso, S. G. Wettstein, M. A. Mellmer, E. I. Gurbuz and J. A. Dumesic, *Energy & Environmental Science*, 2013, **6**, 76-80.

Chapter 2: Experimental Techniques

2.1 Catalyst Preparation/Synthesis

2.1.1 Supported Metal Catalysts

10 wt% Pd/C, 5 wt% Ru/C and Pt black were obtained from Sigma-Aldrich for use in lignin depolymerization. For lignin depolymerization all catalysts were used as obtained from the manufacturer without further pretreatment.

A $RuSn_4$/C catalyst was synthesized by incipient wetness impregnation of the 5 wt% Ru/C catalyst from Sigma-Aldrich with an aqueous solution of $SnCl_2 \cdot H_2O$ followed by heating in air at 353 K for 2 h. Both the Ru/C and RuSn4/C catalysts were used for the hydrogenation of levulinic acid to γ-valerolactone (GVL). Prior to reaction studies, the catalysts samples were reduced in situ for 3 h at 723 K (1 K min^{-1}).

Catalysts for water-gas shift (WGS) studies included 5 wt% Pt, 5 wt% Re, 10 wt% PtRe (2:1), and 10 wt% PtRe (1:2), which were supported on the inert carbon black Vulcan XC-72 (CABOT). These catalysts were prepared as reported by Kunkes *et al.*[1] by incipient wetness impregnation with a chloroplatinic(IV) acid hexahydrate (Sigma-Aldrich) and perrhenic acid (aqueous solution, 50–54% Re, Strem) dissolved in deionized water. Prior to reaction the catalysts were reduced at 573 K (with a heating rate of 0.5 K min^{-1}) under a pure hydrogen flow at standard temperature and pressure (STP) (100 cm^3 min^{-1}).

1 wt% Au/SiC catalyst for formic acid decomposition was prepared by a modified deposition by precipitation method. Dry acid-treated silicon carbide was dispersed in 100 mL of a 1 mM chloroauric acid (Sigma-Aldrich) solution at room temperature. The pH of the mix was adjusted to 9 by drop-wise addition of 2.5 M ammonium hydroxide (Sigma-

Aldrich). The mixture was aged for 6 h under vigorous stirring at room temperature and was then filtered and washed with deionized water to remove chlorine ions. The sample was dried overnight at 373 K. The dried catalyst was reduced in situ, prior to the reaction at a temperature between 623 and 773 K (with a heating rate of 0.5 K min^{-1}) under pure hydrogen flow (30 cm^3 STP min^{-1}) for 4 h. Catalyst reductions at temperatures above 773 K (and up to 1073 K) were performed in a quartz flow-through cell under the same operating conditions.

4 wt% Au/SiO_2 was prepared following the procedure above for the 1 wt% Au/SiC. $AuMo/SiO_2$ was prepared by addition of cycloheptatriene molybdenum tricarbonyl (STREM) to 4 wt% Au/SiO_2. A reduced 4 wt% Au/SiO_2 sample was transferred to an inert atmosphere glove box using a flow through cell with stopcocks to avoid air exposure. A solution of cycloheptatriene molybdenum tricarbonyl in n-pentane (1 mg precursor/g solvent) was added to the 4 wt% Au/SiO2 inside the glove box. The mixture was stirred for 2 h inside the glove box and transferred to a vacuum oven where the sample was dried overnight at 318 K. The dried sample was stored inside the glove box until use. Mo/SiO_2 samples were prepared by deposition the organometallic Mo precursor follow the same method as for $AuMo/SiO_2$.

2.2. Catalyst Characterization

2.2.1 CO Chemisorption

For Pt/C and PtRe/C the active site were measure by CO chemisorption at 308 K using an ASAP 2020C (Micromeritics) after the catalyst was reduced at 573 K (0.5 K

min^{-1}). The number of catalytically active sites was taken to be equal to the irreversible CO uptake at the experimental conditions.

2.2.2 Inductively Coupled Plasma Elemental Analysis

A Perkin-Elmer Plasma 400 ICP Emission Spectrometer was used to quantify the metal content of supported metal catalysts. Reduced supported metal samples were suspended in aqua regia to dissolve the metal from the support. Standard solutions for the metal of interest were used to measure the response and sensitivity of the instrument to each metal.

2.2.3 Electron Microscopy and Spectroscopy

The particle-size distributions were determined from scanning transmission electron microscopy (STEM images). STEM characterization was performed using a FEI Titan STEM with CEOS probe aberration corrector operated at 200 kV with spatial resolution of <0.1 nm. For imaging, a high-angle annular dark-field (HAADF) Z-contrast STEM was used, with HAADF detector angle ranging from 54 to 270 mrad, probe convergence angle of 24.5 mrad, and probe current of ≈25 pA. To prepare samples for STEM, the catalyst samples were first suspended in ethanol, ultrasonicated for 5 min, and then deposited onto ≈5 nm thick Si window TEM grids. STEM samples were plasma cleaned for 10 min with 20% O_2 + 80% Ar gas immediately before loading into the microscope. To prepare AuMo samples for STEM, the catalysts were previously activated in a Schlenk tube under RWGS flow at 573 K, cooled to room temperature, sealed, and then opened in a glove box under N_2 atmosphere to avoid contact with air.

The samples were then suspended in ethanol and deposited on carbon-coated copper grids in a N_2 atmosphere. This procedure was previously reported to be and effective method to avoid leaching of oxidized oxophilic components into solution during the ethanol suspension process.[2] STEM samples were plasma cleaned for 15 min before loading into the microscope.

The particle-size distributions of the Au/SiC and AuMo/SiO_2 catalysts were calculated from the acquired STEM images. From the particle-size distributions, the number average Au particle sizes were determined using the relation $d = \Sigma_i \frac{d_i}{n}$, where d_i is the particle diameter of each Au particle, *n* is the total number of Au particles counted from the STEM images of a given sample, and the summation was performed over all the particles that were identified in the STEM images.

2.2.4 Fourier Transform Infrared Spectroscopy

Catalyst samples were pressed into self-supporting pellets using a 1.2 cm die. Au/SiO_2 and AuMo/SiO_2 pellets were fixed in the sample holder of a transmission cell described elsewhere.[3] The cell was sealed and the sample was activated in a flowing RWGS gas mixture (H_2:CO_2 2:1) for 4 h at 573 K (2 K min^{-1}). After activation the sample was cooled under RWGS flow to room temperature then evacuated to 10^{-5} Torr and a background scan was recorded. Fourier transform infrared (FTIR) (Nicolet 6700) spectra of adsorbed CO were obtained in transmission mode in the presence of 1% CO in He (Airgas). The spectra were collected at temperatures ranging from 148 to 383 K, and the cell was allowed to equilibrate for 5 min at each individual temperature. After the FTIR measurements were performed, the cell was evacuated and the same pellet was

exposed to flowing air. The sample was calcined in air for 4 h at 573 K (2 K min^{-1}) and cooled to room temperature. The sample was reactivated in RWGS flow and analyzed as described above. The temperature was measured by a type-K thermocouple and heating was controlled by a PID controller (Love Controls Series 16A) connected to a variable autotransformer. The sample holder is designed for collecting spectra at sub-ambient temperatures using flowing liquid nitrogen, as described previously.[3] All data were collected by averaging 256 scans with a resolution of 4 cm^{-1}. Spectral deconvolutions were performed using Origin 9.1 to determine the areal contribution from each peak. The final spectrum of CO adsorbed on each catalyst could be represented by two superimposed Gaussian curves.

2.2.5 Raman Spectroscopy

Raman spectroscopy experiments were carried out using a high-performance Renishaw InVia Raman Spectrometer with a 325 nm (excitation) laser. The laser is a Kimmon IK3201R-F laser with an output of 20 mW and an approximate power of 4 mW at the sample. All measurements used a 2400, l mm^{-1} grating with an efficiency of approximately 30 % at 325 nm. *In situ* Raman studies used an OFR near-UV objective with 15x magnification and a working distance of 8.5 mm. Scattered light was filtered into a UV enhanced (lumogen coated) deep depleted array detector (Renishaw). The laser line was calibrated with a Ne calibration lamp. In addition to calibrating the laser, the Raman spectrograph was calibrated to a diamond standard at 1332 cm^{-1}. Raman measurements were taken over a range of 100-1200 cm^{-1} and a dispersion of 1.36565 cm^{-1} $pixel^{-1}$. *In situ* measurements were taken using a fully open aperture and an exposure

time of 360 s, with four accumulations. Approximately 10 mg of sample was used for each *in situ* experiment. Experiments were performed in a high-temperature cell (Linkam CCR1000) designed for temperatures up to 1273 K using a quartz window with water-cooled O-rings. The temperature was controlled by a Linkam T95-HT system. Gas flows during *in situ* experiments were controlled by mass flow controllers (Bronkhorst EL-Flow) with maximum flow rates of 50, 100, and 40 cm^3 STP min^{-1} for hydrogen, helium, and oxygen/carbon dioxide, respectively. The mass flow controllers were connected to a digital readout system (Bronkhorst series E-7000) capable of mixing gases with variable flow rates. Catalysts were first activated for 2 h at 573 K (10 K min^{-1}), under RWGS flow (H_2:CO_2 2:1 15 cm^3 STP min^{-1}). The cell was then flushed with He for 10 minutes, and the sample was oxidized at 573 K under a flow of 16 cm^3 min^{-1} He (Airgas, UHP) and 4 cm^3 min^{-1} O_2 (Airgas, Research Grade). The sample was oxidized for two hours prior to obtaining a Raman spectrum. Samples were kept at 573 K for spectra acquisition.

2.2.6 X-ray Absorption Spectroscopy

Au L-edge (11.919 keV) and Mo K-edge (20.000 keV) x-ray absorption spectroscopy (XAS) measurements were performed on the beam lines of the Materials Research Collaborative Access Team (MRCAT, 10-BM and 12-BM) at the Advanced Photon Source (APS) at Argonne National Laboratory. Ionization chambers were optimized to provide maximum current with a linear response (~10^{10} photons detected s^{-1}). The x-ray beam was 0.25 mm^2 and data were collected in both transmission and fluorescence modes. A third detector in series was used to simultaneously collect a foil reference spectrum with each measurement for energy calibration. All catalysts were

pretreated in a continuous-flow reactor, consisting of a quartz tube (1 inch OD, 10 inch length) sealed with Kapton windows by two Ultra-Torr fittings. A ball valve was welded to each Ultra-Torr fitting to enable gas flow through the reactor. An internal type-K thermocouple was fixed against the catalyst sample holder to monitor temperature. Catalyst samples were pressed into a cylindrical sample holder consisting of six wells, each forming a self-supporting pellet. The mass of catalyst was selected to give an absorbance of approximately 1.0. The catalysts were reduced in flowing 3.5% H_2 in He (50 cm^3 STP min^{-1}) at 573 K, purged with flowing He for 10 min and then cooled to room temperature. Calcination treatments were performed by flowing air at 573 K, cooling to room temperature and performing the reduction procedure detailed above. XAS spectra were collected for the reduced samples before and after calcination. Traces of oxygen and moisture in the H_2 and He were removed by means of a purifier (Matheson PUR-Gas Triple Purifier Cartridge).

2.2.7 Density Functional Theory Calculations

All DFT calculations performed for the Pt(111) surface are reported in the work of Grabow *et al.*[4] The DFT calculations for the Pt_3Re(111) surface were performed using the DACAPO total energy code.[5, 6] A 2 x 2 x 4 unit cell with 6 equivalent layers of vacuum was used to represent the surface as a periodic supercell. The slab consisted of four layers of metal atoms. Adsorption was allowed on only one of the exposed surfaces in which the top two surface layers were allowed to relax, whereas the bottom two layers were fixed at their bulk coordinates. Ultrasoft Vanderbilt pseudopotentials[7] were utilized to describe core-electron interactions, and the Kohn–Sham one-electron valence states

were expanded in a basis of plane waves with kinetic energy below 25 Ry. The surface Brillouin zone was sampled at 18 special Chadi-Cohen k-points. Convergence was confirmed with respect to the k-point set and the number of metal layers used in the slab. The PW91 generalized gradient approximation (GGA-PW91)[8, 9] was used self-consistently for describing the exchange-correlation energy and potential. The electron density was determined by iterative diagonalization of the Kohn–Sham Hamiltonian, the Fermi-population of the Kohn–Sham states (kBT = 0.1 eV), and Pulay mixing of the resulting electron density.[10] The calculated equilibrium lattice constant for the bulk Pt_3Re alloy was 3.97 Å, which is in agreement with the experimental value of 3.90 Å.[11]

The Au(111) surface was modeled by a three-layer slab with a p(3 x 3) unit cell, corresponding to 1/9 monolayer (ML) coverage for a single adsorbate in the unit cell, periodically repeated in a super cell geometry with five equivalent layers of vacuum between any two successive metal slabs. All the Au atoms in this model surface were kept fixed in their bulk truncated positions, as our systematic investigations showed that surface relaxation does not have a significant effect on the energetics for this system. The super cell used to model the Au(100) facet consists of a p(3 x 3) unit cell with four layers of metal atoms, top two of which were allowed to relax, and five equivalent layers of vacuum spacing separating the periodic slab images. The Au(211) slab was constructed by a 1 x 3 unit cell and consisted of nine Au layers (having terrace three atoms deep and three atoms wide). Successive slabs were separated by a vacuum equivalent to 12 such Au(211) layers. Adsorption was allowed on only one of the two exposed surfaces for all three slabs, and the electrostatic potential was adjusted accordingly.[12, 13] The surface Brillouin zone of (111) slabs was sampled at 18 special Chadi–Cohen[14] k-points, whereas

that for the (100) and (211) slabs were sampled using a 4 x 4 x 1 Monkhorst–Pack[15] k-point mesh. Ionic cores were described by ultrasoft Vanderbilt pseudopotentials[7] and the Kohn–Sham one-electron valence states were expanded in a basis of plane waves below a kinetic energy of 25 Ry. The exchange-correlation energy and potential were described self-consistently using the generalized gradient approximation (GGA-PW91).[8, 9] The electron density was determined by iterative diagonalization of the Kohn–Sham Hamiltonian, Fermi population of the Kohn–Sham states (kBT = 0.1 eV), and Pulay mixing of the resulting electronic density.[10] The total energies were then extrapolated to kBT = 0 eV. The calculated equilibrium lattice constant for bulk Au was found to be 4.18 Å, in reasonable agreement with the experimental value (4.08 Å).[16]

2.2.8 Microkinetic Modeling

The mean-field microkinetic models used in the study of the WGS reaction in Chapter 5 accounted for a total of 15 elementary steps. Relevant kinetic and thermodynamic parameters (e.g., pre-exponential factors, activation energies, (EAs) reaction energies, and so on) were obtained from DFT calculations by following the methodology utilized by Grabow *et al.*[4] and Gokhale *et al.*[17] Spontaneous reactions, in which no transition state was found, were assigned pre-exponential factors of 10^{13} s^{-1}. All gas-phase enthalpies and entropies were obtained from the National Institute of Standards and Technology (NIST) archives.[18] The entropy of adsorbed species was calculated as the gas-phase entropy minus the three-dimensional translational contribution $S_{trans,3D}$. To account for the vibrational and rotational contributions to the entropy of adsorbed species, a fitting factor, F_{loc}, was utilized.[19]

Our reactor was modeled as a continuously-stirred tank reactor (CSTR) with the integration and parameter optimization performed by using MATLAB (2010A, The MathWorks, Natick, MA).

The mean-field microkinetic model for FA decomposition was developed on the basis of 17 elementary steps, including some steps that are in common with the WGS reaction. The initial estimates for the ZPE-corrected binding energies (BEs) and EAs were derived from DFT calculations and were later adjusted to reproduce the experimental kinetic dataset collected on the Au/SiC catalysts. Entropies of adsorbed intermediates and pre-exponential factors were determined from the DFT-calculated vibrational frequencies following a procedure described elsewhere.[20] Lateral adsorbate–adsorbate interactions were neglected and all the BEs and EAs were assumed to be coverage independent. This assumption is reasonable as we expect surface coverages to be low under our experimental conditions. The maximum surface coverage was restricted to 1 ML and multilayer adsorption was not considered. We assumed that all species occupy exactly one site on the surface, except for the bidentate formate (HCOO), which blocks two surface sites. Given the geometry of the reactor used in our experiments, the reactor was modeled as a plug-flow reactor. Hence, our reactor model comprised of five differential equations for the gaseous flow rate along the reactor length, eight steady-state algebraic equations for the fractional surface coverages of reaction intermediates, and one site-balance equation. Further details of our model formulation can be found in previous work.[4, 20, 21]

2.3 Reaction Studies

2.3.1 Batch Reactions

A 300 ml autoclave (Parr Instruments) with magnetic stirring was used for lignin extraction and depolymerization reactions in Chapter 3. After loading the biomass, catalyst and solvent, the reactor was purged with hydrogen and pressurized to 500 psi. The reactor temperature was increased using an external electrical heater and controlled with a type J thermocouple connected to a PID controller. The liquid phase was analyzed by GC (Shimadzu GC-2010 equipped with FID) and GC-MS (Shimadzu GCMS-QP2010S).

The biphasic reactions performed in Chapter 3 were carried out in 10 mL glass reactors kept at constant temperature in a pre-heated oil bath using magnetic stirring (1200 rpm). To end the reactions, the glass reactors were taken out from the oil bath and cooled in an ethylene glycol bath kept at cryogenic temperature with dry ice. The reactors were then placed in a centrifuge for 2 min at 3000 rpm to accelerate phase separation.

The biphasic reactions performed in Chapter 4 were carried out in 100 mL Teflon vessels heated in a Mars X microwave accelerated reaction system (CEM). The reaction temperature and stirring were internally measured and controlled by the apparatus and the maximum power output was set at 600 W. At the end of the program the vessels were removed from the microwave and cooled in an ice bath to end the reactions.

2.3.2 Continuous Flow Reactions

The selective hydrogenation of levulinic acid to GVL in Chapter 3 was carried out in a down-flow fixed bed reactor. The catalyst was loaded in a stainless steel tube with

¼” OD and 10 cm length. The catalyst was mixed with crushed silica granules to fill the reactor volume. Two plugs of quartz wool were utilized to keep the catalyst bed in place. The reactor was heated with an aluminum block that was heated externally by a heating tape and wrapped with fiberglass insulation. Type-K thermocouples (Omega) were used to measure the reaction temperature, which was controlled by a PID controller (Love controls 16A) connected to a variable transformer (Tesco). Mass flow controllers (Brooks 5850E) were used to regulate the flow of H_2 during the experiments. A back-pressure regulator (GO model BP-60) was used to control the total pressure, which was measured by two gauges at the entrance and the exit of the bed. A gas-liquid separator at room temperature was used to collect the liquid effluent phase for analysis. The reactants were introduced into the reactor using a Syringe pump (Harvard Apparatus PHD 2000).

WGS reaction studies in Chapter 5 were carried out in a fixed-bed down-flow reactor using a ¼” outer-diameter stainless steel tube. The temperature was measured by using a K-type thermocouple attached to the outside of the reactor. The temperature of the reactor was adjusted by using a furnace connected to a variable autotransformer power source, which was controlled with a temperature controller. The total pressure in the reactor was maintained at 1 atm, and the partial pressures of the gases were controlled by adjusting the flow-rates at the reactor inlet. The flow-rates of all gases were fixed by using calibrated mass-flow meters.

An inlet composition with between 10–25% of CO, 0–35% of H_2, 0–35% of CO_2, and 15–35% of H_2O was used, in which the remaining balance consisted of He. The gases were used as provided, with a purity of 99.99%. Steam was fed to the reactor by vaporizing Millipore-filtered, deionized liquid H_2O at T = 433 K; this was delivered by

using a syringe pump (Harvard Apparatus). The feed and effluent gases were analyzed by using gas chromatography with a thermal conductivity detector (TCD). Steam was removed from the reactor effluent stream by using a water trap (trap immersed in an ice/H_2O bath).

Gas phase FA decomposition studies in Chapter 6 were conducted in the same reactor setup used for WGS reactivity studies where the major change to the system was the use of a ½" outer diameter stainless steel tube. Liquid FA (Sigma-Aldrich) was delivered to the reactor system at room temperature using a syringe pump (Harvard Apparatus) and vaporized at the reactor inlet. The feed and effluent gases were analyzed using gas chromatography with a TCD.

RWGS reaction studies in Chapter 7 were conducted in a fixed-bed down-flow reactor containing the catalyst packed between quartz wool and silica chips in a 1/4-inch outer diameter stainless steel tube. The total pressure in the reactor was maintained at 8.1 bar using a back-pressure regulator and the reaction temperature was set at 573 K. The temperature was measured using a K-type thermocouple attached to the outside of the reactor. The temperature of the reactor was adjusted by using a furnace connected to a variable autotransformer, which was controlled with a temperature controller. The flow rates for the reactant gases CO_2 and H_2 were fixed using calibrated mass-flow meters (Cole-Parmer FF-32907-59). Research grade CO_2 and ultra-high purity H_2 (Airgas) were used. The composition of the product gases was analyzed by an online gas chromatograph with a barrier discharge ionization detector (GC-BID) system equipped with an auto-sampling 6-port valve (Shimadzu). The BID uses helium plasma to detect

permanent gases such as CO_2, CO, H_2 with high sensitivity. The GC-BID system was calibrated using Scott specialty gases (P/N 34507 and 34512).

2.4 References

1. E. L. Kunkes, D. A. Simonetti, J. A. Dumesic, W. D. Pyrz, L. E. Murillo, J. G. G. Chen and D. J. Buttrey, *Journal of Catalysis*, 2008, **260**, 164-177.
2. S. H. Hakim, C. Sener, A. C. Alba-Rubio, T. M. Gostanian, B. J. O'Neill, F. H. Ribeiro, J. T. Miller and J. A. Dumesic, *J. Cat.*, Accepted.
3. J. Y. Shen, J. M. Hill, R. M. Watwe, B. E. Spiewak and J. A. Dumesic, *J. Phys. Chem. B*, 1999, **103**, 3923-3934.
4. L. C. Grabow, A. A. Gokhale, S. T. Evans, J. A. Dumesic and M. Mavrikakis, *J. Phys. Chem. C*, 2008, **112**, 4608-4617.
5. B. Hammer, L. B. Hansen and J. K. Norskov, *Physical Review B*, 1999, **59**, 7413-7421.
6. J. Greeley, J. K. Norskov and M. Mavrikakis, *Annu Rev Phys Chem*, 2002, **53**, 319-348.
7. D. Vanderbilt, *Phys Rev B Condens Matter*, 1990, **41**, 7892-7895.
8. J. P. Perdew, J. A. Chevary, S. H. Vosko, K. A. Jackson, M. R. Pederson, D. J. Singh and C. Fiolhais, *Phys Rev B Condens Matter*, 1992, **46**, 6671-6687.
9. J. A. White and D. M. Bird, *Phys Rev B Condens Matter*, 1994, **50**, 4954-4957.
10. G. Kresse and J. Furthmuller, *Computational Materials Science*, 1996, **6**, 15-50.
11. B. N. Grgur, N. M. Markovic and P. N. Ross, *Electrochimica Acta*, 1998, **43**, 3631-3635.
12. J. Neugebauer and M. Scheffler, *Physical Review B*, 1992, **46**, 16067-16080.
13. L. Bengtsson, *Physical Review B*, 1999, **59**, 12301-12304.
14. D. J. Chadi and M. L. Cohen, *Physical Review B*, 1973, **8**, 5747-5753.
15. H. J. Monkhorst and J. D. Pack, *Physical Review B*, 1976, **13**, 5188-5192.
16. J. Donohue, Wiley, New York, 1974, p. 222.
17. A. A. Gokhale, J. A. Dumesic and M. Mavrikakis, *Journal of the American Chemical Society*, 2008, **130**, 1402-1414.
18. National Institute of Standards and Technology (U.S.), *Journal*.
19. R. D. Cortright and J. A. Dumesic, *Advances in Catalysis, Vol 46*, 2001, **46**, 161-264.
20. L. C. Grabow and M. Mavrikakis, *ACS Catal.*, 2011, **1**, 365-384.
21. J. A. Dumesic, A. A. Gokhale, S. Kandoi, J. P. Greeley and M. Mavrikakis, *Chemical Engineering Science*, 2004, **59**, 4679-4691.

Chapter 3: Catalytic Conversion of Biomass Using Lignin Derived Solvents

3.1 Introduction

The upgrading of biomass for the production renewable fuels and chemicals is currently a highly studied area. However, in order for biomass to be truly viable it will be necessary to efficiently utilize all of the components present in lignocellulosic feedstocks, i.e. cellulose, hemicellulose and lignin. Of these three components, lignin is the most recalcitrant and its valorization remains a major issue.[1] Due to the difficulty in its processing and upgrading, lignin is generally burned and used for process heat. In this chapter, however, alternative uses for lignin that could prove more valuable are explored.

Specific to the upgrading of the C5 and C6 sections of biomass, phenolic molecules have been identified as efficient solvents for the high yield production of furfural (FuAl), 5-hydroxymethyl-furfural (HMF), levulinic acid (LA) and γ-valerolactone (GVL).[2, 3] Inspection of the native structure of lignin, Figure 3.1, reveals it can potentially be converted into aromatics and phenolics by selectively cleaving the ether bonds. In fact, a variety of metal catalysts have been studied in the literature for the hydrogenolysis of lignin.[4-6] However, the integration of the lignin derived phenolic monomers into biomass upgrading strategies has not been explored. To bridge this knowledge gap a study on the viability of a lignin-derived solvent (LDS) for the upgrading of biomass using biphasic reactors was performed and the results are compared to similar solvents studied in the literature. Importantly, we have quantified the capacity of the LDS to partition the reactants and products from the acidic aqueous phase, the partition coefficient, and used it to explain the obtained selectivities for reactions in Figure 3.2.

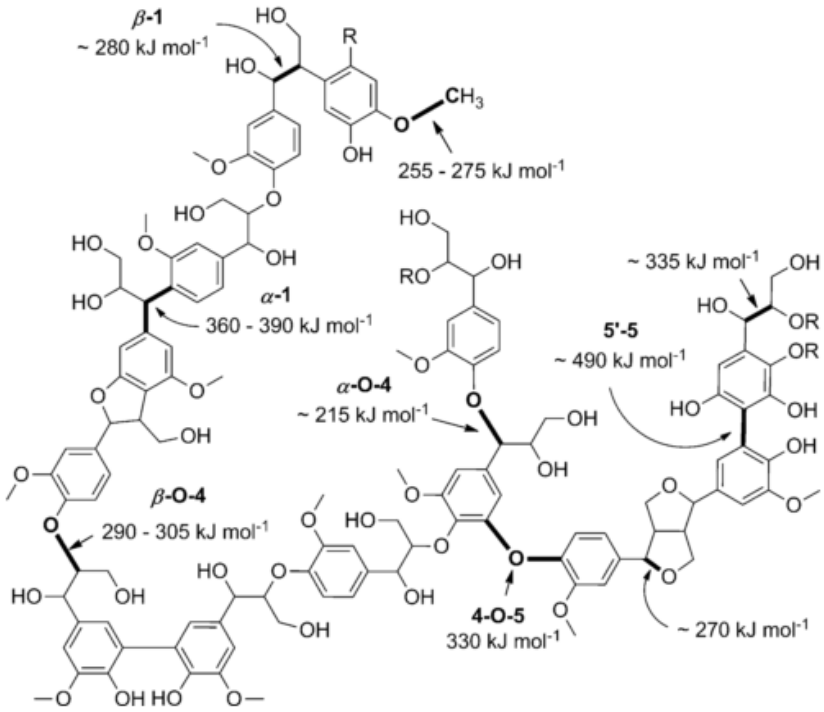

Figure 3.1. Example of lignin structure showing some of the primary linkages and bond dissociation enthalpies.[7]

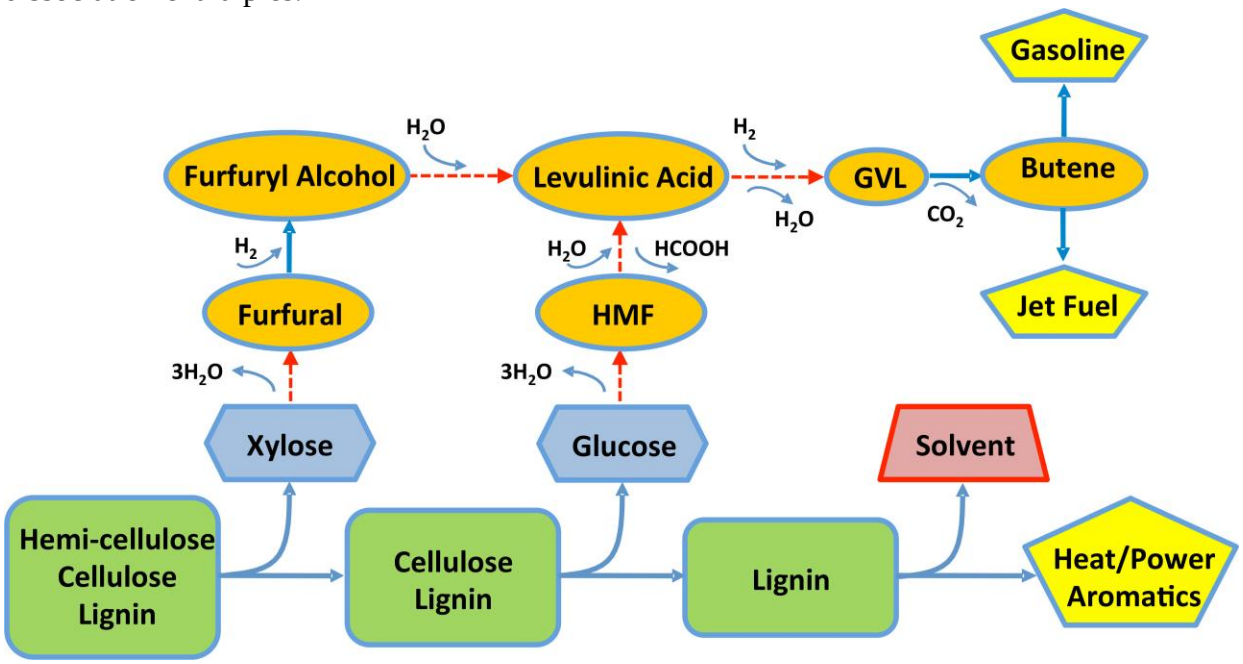

Figure 3.2. Roadmap for conversion of lignocellulosic biomass (rectangles) to chemicals (ovals) and fuels (pentagons), passing through the intermediate formation of C5 and C6 sugars (hexagons). Dashed arrows indicate processes that can be carried out using a lignin-derived organic solvent for the production of FuAL, HMF, LA and/or GVL.

3.2 Materials and Methods

3.2.1 Catalyst Preparation

A $RuSn_4$/C catalyst was synthesized by incipient wetness impregnation of the 5 wt% Ru/C catalyst from Sigma-Aldrich with an aqueous solution of $SnCl_2 \cdot H_2O$ followed by heating in air at 353 K for 2 h. Both the Ru/C and $RuSn_4$/C catalysts were used for the hydrogenation of levulinic acid to γ-valerolactone (GVL). Prior to reaction studies, the catalysts samples were reduced in situ for 3 h at 723 K (1 K min^{-1}).

3.2.2 Lignin Depolymerization Reaction

10 wt% Pd/C used in the depolymerization reactions was obtained from Sigma Aldrich. Poplar wood chips used in lignin depolymerization studies were obtained from the Forest Products National Laboratory (Madison, WI). The wood chips were crushed to mesh 20-40 prior to the experiments and used without drying. The moisture content of the wood was measured by drying the wood chips at 363 K for 24 hours and found to be 7 wt%.

A 300 mL autoclave (Parr Instruments) with magnetic stirring was used for lignin extraction and depolymerization reactions. In a typical lignin conversion reaction, 10 g of wood powder and 0.5 g of catalyst were mixed in 100 ml water. The reactor was purged with hydrogen and pressurized to 500 psi. The reactor temperature was increased to 473 K using an external electrical heater and controlled with a type J thermocouple connected to a PID controller. After holding the temperature for 1 h, the reactor was cooled to room temperature and depressurized. The reaction mixture was filtered to separate the liquid products from the wood residue and catalyst. The liquid phase was analyzed by GC

(Shimadzu GC-2010 equipped with FID) and GC-MS (Shimadzu GCMS-QP2010S). The phenolic monomers in the aqueous phase were extracted by contacting with 50 mL of diethyl ether (DEE) (Sigma Aldrich) and purified in a rotary evaporator.

3.2.3 Liquid-Liquid Extractions

Liquid-liquid extractions of FuAl, FuOH, HMF and LA were carried out in batch systems starting with different concentrations (in the aqueous phase) using propyl guaiacol (PG) and LDS in a 1:1 mass ratio with the aqueous phase at room temperature. In addition, equimolar amounts of LA and formic acid (FA) in 0.5 M sulfuric acid were prepared to represent the products of cellulose deconstruction. The LA and FA were then extracted from this aqueous mixture using PG or LDS with a 1:1 mass ratio.

3.2.4 Biphasic Reactions

The biphasic reactions for the dehydration of glucose and xylose and the hydrolysis of HMF and FuOH were carried out in batch systems utilizing mineral acids as catalysts in the aqueous phase. The experiments were carried out in 10 mL glass reactors kept at constant temperature in a pre-heated oil bath using magnetic stirring (1200 rpm). To end the reactions, the glass reactors were taken out from the oil bath and cooled in an ethylene glycol bath kept at freezing temperature with dry ice. The reactor was then placed in a centrifuge for 2 min at 3000 rpm to accelerate phase separation. The two phases were then separated and analyzed to quantify reactants/products using GC (Shimadzu GC 2060, equipped with a DB-5 column (Restek) and an FID) and HPLC (Waters 2695 instrument equipped with a 996 PDA UV detector and Zorbax SB-C18

reverse phase column (Agilent), operating at a temperature of 308 K using an acetonitrile:water gradient at a flow rate of 1 ml min^{-1}) for organic phase samples and HPLC (Waters 2695 system with a Bio-Rad Aminex HPX-87H column with a differential refractometer (Waters 410) and a photodiode array detector (Waters 996)) for aqueous phase samples.

3.2.5 Selective Hydrogenation of LA to GVL

The selective hydrogenation of LA to GVL was carried out in a down-flow fixed bed reactor over 5 wt% Ru/C and $RuSn_4$/C. The feed was prepared by extracting LA and FA from an aqueous solution (2 M LA, 2 M FA, 0.5 M H_2SO_4) with PG. The catalyst was loaded in a stainless steel tube with ¼" OD and 10 cm length. In a typical experiment, 0.1 g of catalyst was mixed with crushed silica granules to fill the reactor volume. Two plugs of quartz wool were utilized to keep the catalyst bed in place. The reactor was heated with an aluminum block that was heated externally by a heating tape and wrapped with fiberglass insulation. Type-K thermocouples (Omega) were used to measure the reaction temperature, which was controlled by a PID controller (Love controls) connected to a variable transformer (Tesco). Mass flow controllers (Brooks 5850E) were used to regulate the flow of H2 during the experiments. A back-pressure regulator (GO model BP-60) was used to control the total pressure, which was measured by two gauges at the entrance and the exit of the bed. A gas-liquid separator at room temperature was used to collect the liquid effluent phase for analysis. Prior to reactions in fixed bed reactors, catalyst samples were reduced in-situ for 3 h at 723 K (1 K min^{-1}). After the reduction was completed, the temperature and pressure (13.8 bars of H_2) were adjusted, and the

reactants were introduced into the reactor using a Syringe pump (Harvard Apparatus PHD 2000). The weight hourly space velocity (WHSV) was calculated for experiments using the mass flow rate of LA into the reactor and the mass of the catalyst used. The liquid effluent was separated from the hydrogen in a separator at room temperature and analyzed with Shimadzu GC 2060, equipped with a DB-5 column (Restek) and an FID and a Shimadzu 2060 GC/MS with a NIST library of spectra.

3.3 Results and Discussion

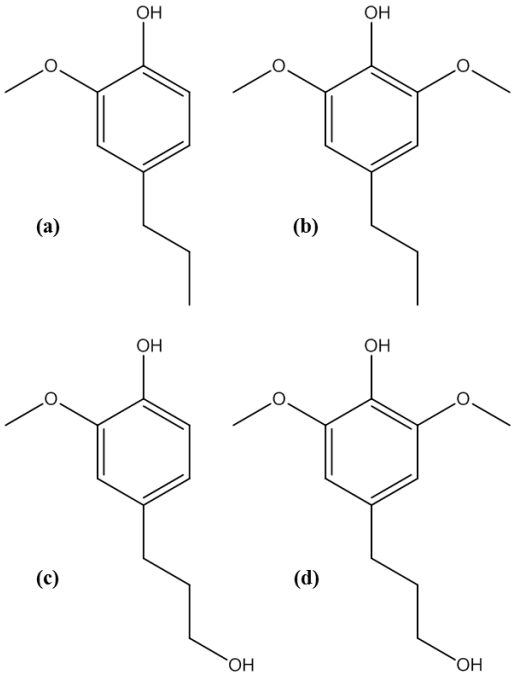

Figure 3.3. Primary phenolic monomers obtained from catalytic hydrothermal depolymerization of lignin. a) propyl guaiacol, b) propyl syringol, c) guaiacyl propanol, d) syringyl propanol.

The depolymerization of lignin using Pd/C produced a mixture of phenolic monomers, Figure 3.3. Propyl guaiacol and propyl syringol (PS) were separated from the guaiacyl propanol and syringyl propanol and the resulting mixture is henceforth termed

LDS. Liquid-liquid extractions of FuAl, FuOH, HMF and LA using PG and LDS in contact with an aqueous phase were carried out, Table 3.1. The extracted amounts are essentially identical at the two concentrations evaluated. In addition, the LDS extracts all species as efficiently as pure PG. This is due to the high structural similarity between the PG and PS in the LDS. NaCl was used in some of the extractions to improve the partitioning into the organic phase, as previously shown.[8] While the partitioning of LA into the organic phase is low, the separation can be improved by increasing the organic to aqueous mass ratio.

Table 3.1. Liquid-liquid extractions of high value platform chemicals using alkylphenol solvents in a 1:1 mass ratio with aqueous solutions at 298 K.

Entry	Solvent	Compound	Concentration (M)	% Mole in Organic Phase	Partition Coefficient (M_{org}/M_{aq})[a]
1	PG	FuAl	0.2	70±1	2.8±0.2
2	PG	FuAl	1.0	77±1	
3	PG	FuOH	0.2	77±2	4.0±0.4
4	PG	FuOH	1.0	82±1	
5	PG	HMF[b]	0.2	75±2	2.9±0.4
6	PG	HMF[b]	1.0	74±3	
7	PG	LA[c]	0.7	40±1	0.68±0.04
8	PG	LA[c]	2.0	41±2	
9	LDS	FuAl	0.2	68±3	2.6±0.4
10	LDS	FuAl	1.0	75±2	
11	LDS	FuOH	0.2	78±3	3.8±0.6
12	LDS	FuOH	1.0	80±2	
13	LDS	HMF[b]	0.2	73±1	2.9±0.3
14	LDS	HMF[b]	1.0	75±2	
15	LDS	LA[c]	0.7	39±2	0.63±0.04
16	LDS	LA[c]	2.0	38±1	

[a] Value reported is the average of entries.
[b] The initial aqueous solution was saturated with NaCl to increase the partitioning to the organic phase.
[c] Aqueous solution also contained 0.5 M sulfuric acid.

Motivated by the results from the liquid-liquid extractions biphasic batch reactions for the dehydration of glucose and xylose to HMF and FuAL, respectively, the hydrolysis of FuOH to LA and the hydrolysis of HMF to LA were carried out in glass reactors. The results for the reactions, Table 3.2, show that high selectivities can be achieved using both PG and the LDS. The selectivities obtained with these biphasic systems is comparable to previous reports using 2-*sec*-butylphenol (SBP),[2, 3] and demonstrate that these organic solvents in contact with an acidic aqueous phase are efficient biphasic systems for the upgrading of furanic compounds.

Table 3.2. Conversion of glucose, xylose, furfuryl alcohol and HMF in biphasic reactors to produce HMF, furfural and levulinic acid, respectively, using PG, LDS and SBP as organic solvents.

Entry	Reactant	wt%	Solvent	O:A[a]	T (K)	Conversion (%)	Product		
							Compound	Selectivity (%)	% in Organic Solvent
1	Glucose	5	PG	2	443	85±1	HMF	58±2	82±3
			LDS			82±2		59±2	88±1
			SBP			91±2		67±2	97±1
2	HMF	1	PG	3	423	96±2	Levulinic Acid	71±2	75±3
			LDS			97±2		73±1	74±2
3	Xylose	1.5	PG	0.15	443	75±2	Furfural	85±2	75±2
			LDS			75±1		82±2	84±2
			SBP[b]			98±2		80±2	90±2
4	Furfuryl Alcohol	1	PG	3	398	99±1	Levulinic Acid	63±2	73±2
			LDS			99±1		65±2	76±2
			SBP[b]	2		100		66±4	81±5

[a] Organic to aqueous solvent ratio by mass.
[b] Data taken from reference 2.

The biphasic dehydration of glucose to HMF (Table 3.2, entry 1) was performed starting from 5 wt% glucose in an aqueous 0.1 M HCl solution saturated with NaCl. A

Lewis acid ($AlCl_3$ in this case), is utilized to catalyze the isomerization of glucose to fructose,[9-11] from which HMF is produced in the presence of the mineral acid catalyst. Using PG in a 2 : 1 mass ratio to the aqueous phase, 58% selectivity towards HMF was obtained at 85% conversion, and 82% of the total HMF is retained in the organic phase. Importantly, the LDS extracts up to 88% of HMF, while exhibiting a similar selectivity. These results compare well to glucose conversion (91%) and HMF selectivity (67%) obtained using SBP as the extractive organic phase. The partitioning of the majority of the HMF into the organic phase would allow its efficient separation and in addition the recycling of the mineral acid present in the aqueous phase. Several studies have also demonstrated the effectiveness of biphasic systems in the dehydration of glucose to HMF[9, 12-14] utilizing high boiling organics (for example, dimethyl sulfoxide) with the intention of suppressing side/degradation reactions; however, the use of organic extractive solvents containing only C, H, and O atoms, such as the LDS, is advantageous.[13]

The hydrolysis of HMF to LA was previously studied in a single-phase system where HCl and H_2SO_4 have been identified as the best catalysts for the system producing high yields (i.e., 94%).[15] However, purification of LA and the recovery of the mineral acid is energy intensive and requires solvent extraction and distillation steps. The presented biphasic processing strategy using PG and LDS, for an organic : aqueous mass ratio of 3 : 1 (Table 3.2, entry 2), results in high selectivities (72%) for production of LA at almost full conversion, allowing the upgrading of HMF in the extracting solvent without a purification step. Additionally, the majority of the produced LA (75%) is

recovered in the organic phase, enabling the separation of LA from the mineral acid in the aqueous phase.

Analogous to the dehydration of glucose, conversion of xylose to FuAl has been previously studied in biphasic systems.[16, 17] These systems utilized organic solvents (e.g., methyl isobutyl ketone, 2-butanol and tetrahydrofuran), which do not partition FuAl efficiently into the organic phase. Using alkylphenol solvents (e.g., SBP) that have high partition coefficients for FuAl, it is possible to concentrate the FuAl to several times the initial concentration of xylose in the aqueous phase by using small amounts of the extractive solvent relative to the aqueous layer.[2] PG and the LDS perform in a manner that is similar to the SBP solvent (Table 3.2, entry 3), resulting in 85% and 82% selectivities to FuAl, respectively, at 75% xylose conversion, using an organic to aqueous mass ratio equal to 0.15. The partitioning of FuAl into the organic layer leads to 75% and 84% of the FuAl being retained in PG and LDS, respectively.

The FuAl in the organic phase could be distilled out at this point as an end product or it can undergo subsequent hydrogenation in the gas phase over a metal catalyst to form FuOH,[18, 19] which can be converted in another biphasic reactor to LA. The yield of LA by hydrolysis of FuOH is limited by polymerization reactions, even at low concentrations. Thus, we implemented a biphasic reactor system where the FuOH is slowly partitioned into the aqueous phase from the organic phase. Due to the high partitioning of FuOH into PG and the LDS, it is possible to minimize the concentration of FuOH in the aqueous phase. The LA yields at full conversion using PG (63% yield, with 73% of LA being in PG) and the LDS (65% yield, with 76% of LA being in LDS) compare well with experiments using SBP as a solvent, where 81% of the LA was

partitioned into the organic medium with comparable yields (~65%).[2] As shown previously by Lange *et al.*[20] and Gürbüz *et al.*,[2] a semi-batch operation mode can be adopted to process higher concentrations (~10–20 wt%) of furfuryl alcohol.

Figure 3.2 shows the hydrogenation of LA to GVL as a step where both the C5 and C6 pathways can be combined and processed into transportation fuels. Several publications have addressed this reaction with a variety of methods.[21-23] In the present study, we studied the conversion of LA to GVL, using an organic stream containing LA and FA in PG that was prepared by contacting PG with an aqueous stream of LA and FA prepared to match the effluent composition from the acid-catalyzed hydrolysis of cellulose. Table 3.3 shows the effects of temperature and weight hourly space velocity (WHSV) on the hydrogenation of LA to GVL in PG solvent using a Ru/C catalyst in a packed bed flow reactor. Increasing the temperature from 453 to 473 K increased the conversion of LA as well as the conversion of PG, from 62% to 82% and from 0.5% to 3.6%, respectively. In a similar manner, lowering the WHSV of the feed from 2.2 to 1.2 h^{-1} affected the extent of hydrogenation for both LA and PG, with an increase from 62% to 100% and from 0.5% to 6.0%, respectively. Hydrogenation of PG solvent could be completely suppressed with the addition of Sn to 5 wt% Ru/C in a 1 : 4 Ru : Sn molar ratio as demonstrated previously for SBP.[21, 24] Even though the addition of Sn decreased the GVL production rate (3.4 mmol g^{-1} h^{-1}), $RuSn_4$/C exhibited good stability for 80 h of operation at around 96% LA conversion, as shown in Figure 3.4.

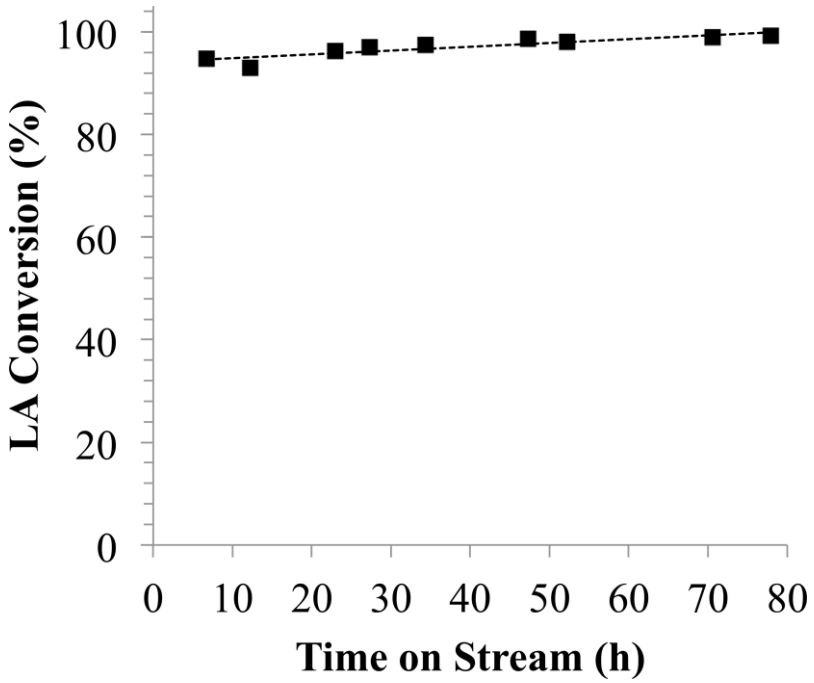

Figure 3.4. Levulinic acid conversion versus time on stream over $RuSn_4$/C at 453 K, 34.5 bar H_2 pressure and WHSV= 0.4 h^{-1}. Feed is obtained using PG to extract LA and FA from an aqueous solution.

Table 3.3. Hydrogenation of LA to GVL over 5 wt% Ru/C in the presence of FA using PG as the solvent at different reaction conditions. [a]

Entry	T (K)	WHSV[b] (h^{-1})	Conversion (%)		GVL Selectivity (%)	GVL rate ($mmol/g_{cat}\ h^{-1}$)
			LA	PG		
1	453	2.2	62	0.5	96	13.6
2	473	2.1	82	3.6	94	17.2
3	453	1.2	100	6.0	93	13.2

[a] Feed composition is given by LA/FA = 42%/9%. H_2 pressure in the reactor was fixed at 13.8 bars.
[b] WHSV is defined as mass of LA fed per mass of catalyst per hour.

3.4 Conclusions

The use of lignin-derived alkylphenols as solvents in biphasic reactors enables *in situ* separation of products and/or reactants, thereby minimizing undesirable side reactions in the aqueous phase and enabling the recycling of the mineral acid catalysts in biomass processing. The overall processing strategy presented here could benefit from

further optimization of lignin depolymerization processes to increase the yields obtained in the production of alkylphenol compounds. In addition, while the Ru/C catalyst is effective for the conversion of LA to GVL in the lignin-derived solvent, it is possible to use bimetallic catalysts, such as RuSn, to further minimize the rates at which the solvent is hydrogenated during the conversion of LA to GVL and to ensure stable activity. However, during this final step a large amount of hydrogen is necessary. As stated previously in order for this process to be sustainable this hydrogen will have to be provided sustainably and if possible from biomass.

3.5 Acknowledgments

The research work presented in this chapter was previously published in 2012, and is adapted here with permission from Green Chemistry. [25]

3.6 References

1. G. Huber, S. Iborra and A. Corma, *Chem. Rev.*, 2006, **106**, 4044-4098.
2. E. I. Gurbuz, S. G. Wettstein and J. A. Dumesic, *ChemSusChem*, 2012, **5**, 383-387.
3. Y. J. Pagán-Torres, T. Wang, J. M. R. Gallo, B. H. Shanks and J. A. Dumesic, *ACS Catal.*, 2012, **2**, 930-934.
4. J. M. Pepper, W. F. Steck, R. Swoboda and Karapall.Jc, *Advances in Chemistry Series*, 1966, 238-&.
5. M. Nagy, K. David, G. J. P. Britovsek and A. J. Ragauskas, *Holzforschung*, 2009, **63**, 513-520.
6. N. Yan, C. Zhao, P. J. Dyson, C. Wang, L. T. Liu and Y. Kou, *ChemSusChem*, 2008, **1**, 626-629.
7. X. Wang and R. Rinaldi, *ChemSusChem*, 2012.
8. Y. Roman-Leshkov and J. Dumesic, *Top. Catal.*, 2009, **52**, 297-303.
9. E. Nikolla, Y. Roman-Leshkov, M. Moliner and M. Davis, *ACS Catal.*, 2011, **1**, 408-410.
10. H. Zhao, J. E. Holladay, H. Brown and Z. C. Zhang, *Science*, 2007, **316**, 1597-1600.
11. M. Chidambaram and A. Bell, *Green Chem.*, 2010, **12**, 1253-1262.

12. Y. Roman-Leshkov, J. N. Chheda and J. A. Dumesic, *Science*, 2006, **312**, 1933-1937.
13. Y. Roman-Leshkov, C. Barrett, Z. Liu and J. Dumesic, *Nature*, 2007, **447**, 982-U985.
14. J. B. Binder and R. T. Raines, *J. Am. Chem. Soc.*, 2009, **131**, 1979-1985.
15. B. Girisuta, L. Janssen and H. Heeres, *Green Chem.*, 2006, **8**, 701-709.
16. J. N. Chheda, Y. Roman-Leshkov and J. A. Dumesic, *Green Chemistry*, 2007, **9**, 342-350.
17. R. Xing, A. Subrahmanyam, H. Olcay, W. Qi, G. van Walsum, H. Pendse and G. Huber, *Green Chem.*, 2010, **12**, 1933-1946.
18. B. Nagaraja, A. Padmasri, B. Raju and K. Rao, *J. Mol. Catal. A: Chem.*, 2007, **265**, 90-97.
19. R. Rao, R. Baker and M. Vannice, *Catal. Lett.*, 1999, **60**, 51-57.
20. J. Lange, W. van de Graaf and R. Haan, *ChemSusChem*, 2009, **2**, 437-441.
21. D. Alonso, S. Wettstein, J. Bond, T. Root and J. Dumesic, *ChemSusChem*, 2011, **4**, 1078-1081.
22. J. Serrano-Ruiz, D. Wang and J. Dumesic, *Green Chem.*, 2010, **12**, 574-577.
23. J. Serrano-Ruiz, D. Braden, R. West and J. Dumesic, *App. Catal., B*, 2010, **100**, 184-189.
24. S. G. Wettstein, J. Q. Bond, D. M. Alonso, H. N. Pham, A. K. Datye and J. A. Dumesic, *Applied Catalysis B-Environmental*, 2012, **117**, 321-329.
25. P. Azadi, R. Carrasquillo-Flores, Y. J. Pagan-Torres, E. I. Gurbuz, R. Farnood and J. A. Dumesic, *Green Chem.*, 2012, **14**, 1573-1576.

Chapter 4: Mechanocatalytic Depolymerization of Biomass Using Lignin Derived Solvents

4.1 Introduction

In Chapter 3 an effective strategy for upgrading the C5 and C6 fractions of lignocellulosic biomass utilizing a lignin-derived solvent was presented. High selectivities at high conversion were possible due to the partitioning of reactants and products between the aqueous and organic phase. However, these yields are mainly possible due to the use of monosaccharides as the reactants. From lignocellulosic biomass monosaccharides are produced in a depolymerization or deconstruction step that produces glucose and xylose. It would be desirable to perform this step using heterogeneous acid catalysts but this is currently cumbersome and therefore homogenous acid catalysts are employed under high severity reactions conditions.[1, 2] Accordingly, the degradation of the furfurals into humins is inevitable. Alternative approaches using ionic liquids are able to promote the depolymerization step at mild conditions but even then the formations of large quantities of humins, from HMF, is a problem.[1-5] Therefore, the development of novel depolymerization processes for the high-yield production of HMF and furfural from lignocellulosic materials is required.

Recently solvent-free approaches for depolymerization of cellulose have emerged in the literature.[6-10] Among these developments, the acid-catalyzed depolymerization of lignocellulosic biomass driven by mechanical forces, provided by a ball-milling, emerges as an important methodology for several reasons.[9] First, milling is often used as a first step in the conversion of lignocellulose biomass. Conventionally, the milling step serves for comminution of the biomass and for amorphization of crystalline domains, making plant biomass more amenable for the chemical or biochemical depolymerization.[11] Thus,

conventional ball-milling is a predominately physical process. Second and more important, by mechanocatalysis, the mechanic forces can be better used than in a conventional milling. This is because milling dry lignocellulose in the presence of an acid leads to dramatically different products: oligosaccharides and lignin fragments fully soluble in water. This finding evidences the chemical nature of this approach. The first analyses of the lab-scale results suggest that the mechanocatalytic approach should be both economically and energetically sustainable as an entry point for bioethanol production.[6, 9] Indeed, a conservative estimate shows that the electrical energy demand for keeping the milling process running would be only slightly more than 10% of the energy content of ethanol produced.[9]

Recently, it was demonstrated that the impregnation of cellulosic fibers with catalytic amounts of HCl or H_2SO_4 is key for the high efficiency of solvent-free, acid-catalyzed mechanical depolymerization of lignocelluloses.[9] This strategy circumvents the contact problems experienced in the process when using solid acids.[6] Indeed, milling the (dry) acid-impregnated substrate produces water-soluble oligosaccharides (WSOs) in quantitative yields within 2 h.[9] Lignocellulosic materials (e.g., beechwood, pinewood, and sugar cane bagasse) are also transformed by the mechanocatalytic method into soluble products within 2−3 h. Figure 4.1 shows a typical ESI mass spectrum of WSO obtained from α-cellulose.

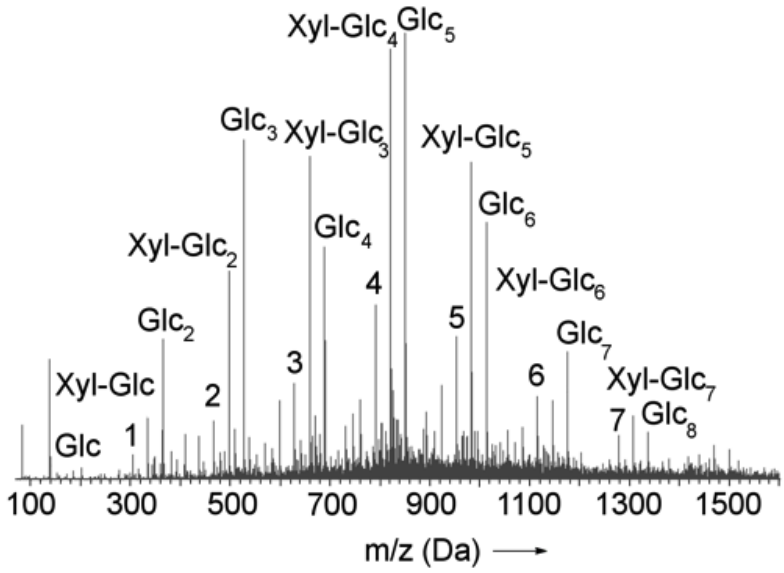

Figure 4.1. Typical ESI-mass spectrum of WSO. Glc and Xyl stand for glucose and xylose, respectively. For clarity, the products containing a levoglucosan unit (LG) are represented by numbers (*n*), where the composition is LG-Glc$_n$. The m/z values correspond to [M+Na$^+$].[9]

The complex chemical nature of WSOs poses a key question: Is such a complex mixture of oligosaccharides useful as a feedstock for the production of platform chemicals? This question is pertinent not only because the complexity of the WSOs but also because, in the best examples, the conversion of cellobiose achieved only low to moderate yields of HMF (12−57%), as recently reviewed by Heeres, de Vries and co-workers.[12] The work presented in this chapter aims to demonstrate the versatility of WSOs as a replacement for glucose and xylose in a complex chemical process.

4.2 Materials and Methods

4.2.1 Impregnation of substrates with acid

10.00 g of biomass substrate (α-cellulose, beechwood and sugarcane bagasse, see Table 4.1 for substrate composition) was dispersed in 150 mL of diethyl ether. To the

dispersion, hydrochloric acid (8 mmol, 37-38 % J. T. Baker) was added dropwise. The mixture was stirred for 1 h after which the organic solvent was removed under reduced pressure at 313 K. In all cases a fine powder was obtained as the final product. The final HCl loading in the material was 0.63 mmol/g, as determined by titration.

Table 4.1. Composition of lignocellulosic biomass substrates

Substrate	Glucans (wt %)	Xylans (wt %)	Lignin (wt %)	Humidity (wt %)	Ash (wt %)	Others (wt %)
α-Cellulose	76	16	0	6	0.1	1.9
Beechwood	41	24	24	5	0.4	5.4
Sugarcane Bagasse	41	15	20	7	2	15

4.2.2 Mechanocatalytic depolymerization of cellulose to water-soluble oligosaccharides

The substrates were milled in a stainless steel vial (12 mL; six stainless steel milling balls at 3.95 g each), using a ball mill (Fritsch, Pulverisette P7) at room temperature. Under working conditions, the temperature inside the mill was not higher than 315 K after 0.5 h. To avoid overheating in reactions carried out longer than 0.5 h, milling was turned off every 0.5 h for 10 min. The overall milling time was 2 h. Acid-impregnated substrate powder (1.2 g) was processed, directly after the impregnation step, at 800 rpm for the indicated times. Ball milled substrate was obtained as a powder and used directly in the experiments.

4.2.3 Conversion of WSO

The experiments were carried out in 100 mL Teflon vessels heated in a Mars X microwave accelerated reaction system (CEM). The reaction temperature and stirring were internally measured and controlled by the apparatus and the maximum power output was set at 600 W. Figure 4.2 shows the heating program used in all experiments unless otherwise noted. Preparation of the aqueous phase layer consisted of using solutions containing various amounts of $AlCl_3$ (anhydrous, Fluka) followed by saturation with NaCl. These solutions were then loaded with WSO to prepare the reaction solution. Table 4.2 lists the nominal concentrations of sugars present in the solution as oligosaccharides. In a typical experiment, 6.0 g of the aqueous feed and 12.0 g of propyl guaiacol (SAFC, Aldrich) were added to the reactor. The reactor was placed in the microwave system and the heating program was performed. Upon cooling, salt precipitated in the aqueous phase changing the organic to aqueous mass ratio from 2:1 to 2.4:1.

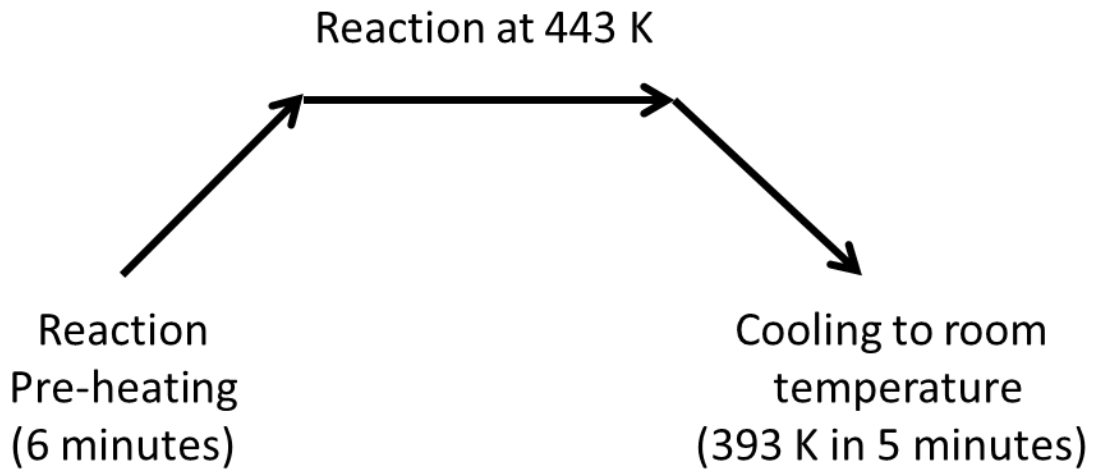

Figure 4.2. Heating program used in the microwave heating of reaction vessels.

For all biphasic experiments, the organic and aqueous phases were separated and immediately analyzed for quantification of glucose, xylose, HMF and furfural by HPLC analysis.

Table 4.2. Reaction conditions for biphasic reaction systems

Substrate	Aqueous Phase Composition[a]	Organic Phase Composition
α-Cellulose[b]	2.5 wt % glucose, 0.5 wt % xylose,	4-propylguaiacol
Beechwood	1.5 wt % glucose, 0.9 wt % xylose, 0.9 wt % lignin, 15 mM $AlCl_3$	4-propylguaiacol
Sugarcane Bagasse	1.5 wt % glucose, 0.6 wt % xylose, 0.8 wt % lignin, 15 mM $AlCl_3$	4-propylguaiacol

[a] All aqueous phases contained 24±1 mM HCl and were saturated with NaCl

[b] Several $AlCl_3$ concentrations were prepared: 5 mM, 10 mM, 15 mM, 25 mM, 30 mM and 100 mM.

4.2.4 HPLC analysis

HPLC analysis was carried out using a Perkin-Elmer HPLC 200 system equipped with a Perkin-Elmer diode array detector (Series 200 EP) and a Perkin-Elmer refractive index detector (Series 200a) maintained at 313 K. The aqueous phases were analyzed using 4 TSKgel G-Oligo-PW columns in series (TOSOH Bioscience) at 353 K, using water as the mobile phase at a flow rate of 0.8 mL min^{-1}. The organic phase samples were

dissolved in acetonitrile and analyzed using a Supelcogel H column (Sigma Aldrich) at 353 K, using a 5 mM H_2SO_4 water: acetonitrile (85:15) v/v solution at a flow rate of 0.2 mL min^{-1}. Glucose and xylose were monitored using the refractive index detector and HMF and furfural were monitored using the diode array detector (285 nm). Conversions are defined as the moles of glucose or xylose reacted divided by the moles of glucose or xylose in the feed (as determined by quantitative saccharification). Selectivity to HMF and furfural are defined as the moles of HMF or furfural produced divided by the moles of glucose or xylose reacted, respectively.

4.3 Results and Discussion

The conversion of WSOs into HMF and furfural, performed in a biphasic system, is chosen as the model reaction for this work. The formation of HMF and furfural from WSOs involves the series of reactions depicted in Figure 4.3.

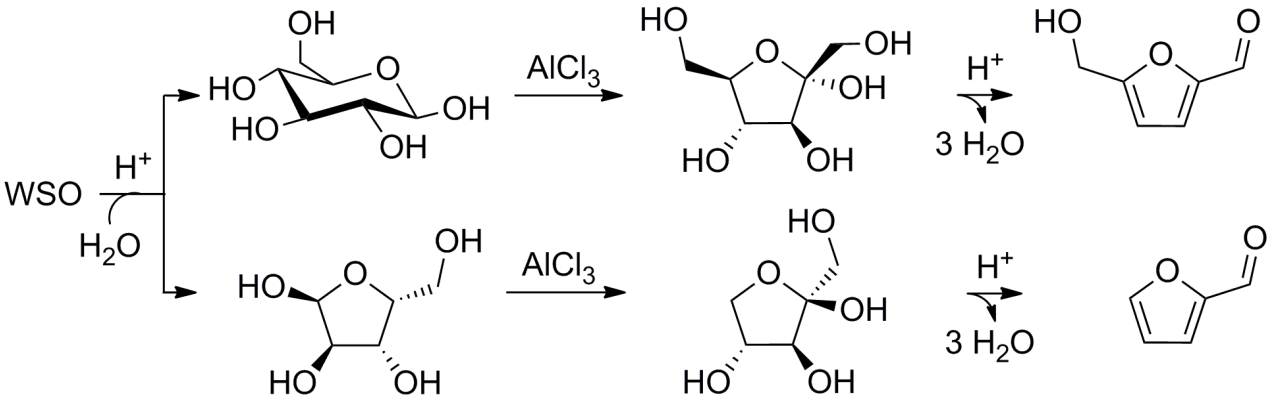

Figure 4.3. Reaction series for the conversion of WSO into HMF and furfural.

Acid−base titrations of the substrate before and after the mechanocatalytic approach showed that the mineral acid was not destroyed; therefore, no extra amount of

acid is necessary to obtain a WSO aqueous solution with pH 1 (10 wt % WSO). WSOs undergo acid hydrolysis in aqueous solutions at temperatures as high as 403 K, forming glucose and xylose as the main products (Table 4.3).[9] Strikingly, we have found now that the hydrolysis rate of WSOs is greatly accelerated by microwave radiation (Table 4.3) so that full conversion at 403 K after only 10 min is achieved. For comparison, the reaction takes 1 h to complete under conventional heating at 403 K (Table 4.3).[9] In light of these new results, the WSOs should be a more convenient source of glucose than cellulose because they readily undergo hydrolysis under microwave conditions, promptly providing the system with monosaccharides.

Table 4.3. Results of Hydrolysis of WSO (α-cellulose) at Full Conversion at 403 K by Conventional and Microwave Heating[a]

	yields (%)				
heating type	glucose dimers	glucose	xylose	HMF	furfural
conventional (1 h)[9]	8	91	96	1	4
microwave (10 min)	3.5	95	95	1.3	4.9

[a] Reaction conditions: substrate (0.10 g) dissolved in water (10 mL, pH 1). The relative standard deviation is ±5%.

For the production of HMF and furfural, glucose and xylose need to be first isomerized to fructose and xylulose, respectively. The isomerization step provides favorable reaction pathways for the formation of HMF and furfural, as recently elucidated by experimental and DFT studies.[13-18] It was demonstrated that $AlCl_3$ catalyzes both isomerization steps, facilitating the formation of HMF and furfural.[19, 20] The isomerization of glucose to fructose is about 4 times slower than the dehydration of fructose to HMF.[19, 20] In a single-phase system, the coexistence of HMF, furfural, and sugars may lead to the formation of humins in large quantities.[3] This problem is

alleviated by the extraction of HMF, upon its formation, in a biphasic reaction system using 4-propylguaiacol, a solvent derived from lignin, or other solvents as the extracting phase.[21-28]

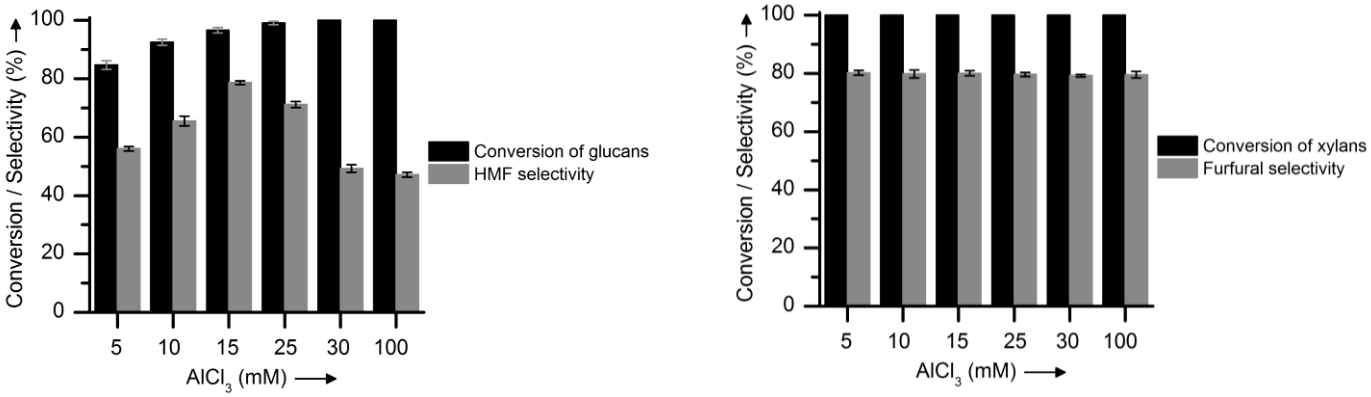

Figure 4.4. Effect of the concentration of $AlCl_3$ on the conversion of glucan and xylan fractions of WSO into HMF (left) and furfural (right), respectively. Reaction conditions: substrate (0.18 g), 24 mM HCl, and the indicated concentration of $AlCl_3$ dissolved in saturated NaCl solution (6 g). 4-Propylguaiacol was used as the extracting organic phase (12 g). Figure 4.2 shows the microwave program used to heat the reaction vessels at 443 K for 9 min.

To examine the effect of $AlCl_3$ on the selectivity for HMF and furfural, the initial experiments were performed at different concentrations of $AlCl_3$ (5−100 mmol) while keeping the concentration of HCl at 24 ± 1 mM. The biphasic reactor was heated by microwave radiation (443 K for 9 min). HMF and furfural were continuously extracted by 4-propylguaicol. Figure 4.4 (left) shows the effect of $AlCl_3$ on the conversion of the glucan fraction of WSO into HMF at 443 K for 9 min. Increasing the concentration of $AlCl_3$ from 5 to 15 mM steadily improved the conversion of the glucan fraction in WSO (from 85 to 97%) and the selectivity for HMF (from 56 to 79%). A further increase in the concentration of $AlCl_3$ from 15 to 100 mM, however, decreased the selectivity for HMF (from 79 to 47%). In this range of concentration, the isomerization rate does not limit the

formation of HMF. In fact, in the presence of 15 mM $AlCl_3$, the experiment led to 97% conversion of glucose in only 9 min. The selectivity to HMF reached 79% at 9 min, but decreased to 49% at 15 min (Table 4.4). Because no other byproduct was detected by HPLC and by GC/MS analyses, these results show overall that HMF decomposes to humins, which can, indeed, be visually detected as very fine black particles at the aqueous−organic interface.

Table 4.4. Conversion of WSO, Obtained from Several Substrates, into HMF and Furfural at 443 K for the Indicated Reaction Time[a]

		Conversion (%)		Selectivity (%)[c]	
Substrate[b]	Reaction time (min)	Glucan	Xylan	HMF	Furfural
α-Cellulose	3	78	99	66	87
	6	86	99	70	83
	9	97	100	79	80
	15	100	100	49	76
Beechwood	6	100	100	60	74
Sugarcane bagasse	6	94	100	65	84

[a] Reaction conditions: substrate (0.2 g), 15 mM $AlCl_3$, and 24 mM HCl dissolved in saturated NaCl solution (6 g); 4-propylguaiacol was used as the extracting organic phase (12 g). [b] The absolute standard deviation is ±2%. [c] Table 4.1 summarizes the substrate composition.

Parallel to the conversion of the glucan fraction into HMF, the xylan fraction in WSOs (from the hemicellulose present in α-cellulose) was converted into furfural. Figure 4.4 (right) shows the effect of $AlCl_3$ on the reaction at 443 K for 9 min. Unlike the conversion of glucose into HMF, full conversion of xylose into furfural was achieved in all cases. In addition, the selectivity for furfural (≈80%) was found to remain unchanged across the range of $AlCl_3$ concentration. Recently, it was showed that the presence of a Lewis acid, in their case $CrCl_3$, should promote the formation of xylulose, leading to a

faster, more selective transformation.[18] This is clearly not the case in our experiments. These different observations can be reconciled if we assume that the glucose and xylose fractions behave analogously. In doing so, we should expect the isomerization rate from xylose to xylulose to be rate-limiting up to a threshold value of Lewis acid. Given the low xylose concentration in the aqueous phase (0.5 wt%), it is likely that even at a concentration of 5 mM $AlCl_3$, this threshold concentration was already achieved.

In contrast with HMF production, the observed furfural decomposition is much less pronounced in these experiments (Table 4.4). Although the selectivity to HMF markedly decreases (from 79 to 49%) with the increase in the reaction time from 9 to 15 min, the selectivity to furfural only slightly decreases (from 80 to 76%). This finding is also in line with the fact that alkylphenolic solvents exhibit a very high partition coefficient for furfural (~90) when contacted with a saturated NaCl solution (aqueous phase).[29] For comparison, the partition coefficient of HMF in 4-propylguaiacol is 3.8. Accordingly, the majority of the furfural is retained in the organic phase, preventing its degradation, while a small, but still considerable, fraction of HMF (~4%) can be present in the aqueous phase.

The best result from Figure 4.4 shows that WSOs were almost fully converted, with selectivity for HMF of 79% at 443 K for 9 min. This result is even better than would be expected by the fast hydrolysis of WSOs under microwave conditions (Table 4.3). Indeed, the yield reported here is higher than that reported for dehydration of glucose (~60%), obtained by biphasic systems heated by microwave radiation.[20] Most importantly, the best yields of HMF presented here are twice as high as those reported

starting the process directly with cellulose. Indeed, under similar conditions, yields of HMF as high as 37% were achieved when starting from cellulose.[20]

The reasons for the improved performance of the biphasic system when starting the experiment with WSOs instead of monosaccharides is not yet fully clear. On one hand, it is clear that the fast formation of monosaccharides from WSOs by microwave heating (Table 4.3) contributes enormously to the results reported here. On the other hand, glucose establishes coordinative interactions with Al(III) species.[30] Tentatively, interactions of WSO with Al(III) species in solution might also be affecting the catalytic properties of the Al(III) species at the isomerization step so that the experiment would be more selective in the initial phase (5−10 min) when a WSO is still present in the aqueous solution.

Encouraged by the finding that WSOs from α-cellulose serve as a reactive feedstock for the high-yield production of HMF and furfural, WSOs from beechwood and sugarcane bagasse were also examined. Milling HCl-impregnated lignocellulosic substrates resulted in full conversion to water-soluble products after 2 h (beechwood) and 3 h (sugar cane bagasse). Because lignin is also fully converted into soluble products, the mixture of products obtained from lignocellulosic substrates is more complex than that of those obtained from α- cellulose, as previously reported.[4]

Table 4.4 compares the results of the production of HMF and furfural obtained from α-cellulose, beechwood, and sugarcane bagasse. The reactions were performed using 15 mM $AlCl_3$ dissolved in the saturated NaCl solution. Again, high conversions of the glucan and xylan content were achieved at short reaction times. High selectivity for HMF and furfural from the water-soluble lignocellulosic substrates was obtained. In the

biphasic system, the partition coefficient of HMF (3.8) was not changed by the presence of lignin-soluble fragments.

At a conversion of glucose of 94% or higher, the isolated yield of HMF reached 60 and 69% in the experiments beginning with water-soluble products from beechwood and sugarcane bagasse, respectively. These yields are still high, as similar studies have reported HMF yields of ~35% when starting from pinewood.[20]

Full conversion of xylose with high selectivity for furfural was achieved for the lignin-containing substrates. The results obtained from the processing of the water-soluble products from lignocellulosic substrates are similar to those previously reported for the dehydration of xylose to furfural.[27, 31] Again, the current yields of furfural (74−84%) are higher than those previously reported for the direct processing of solid lignocellulosic substrates (~65%).[19]

The "greenness" of using HCl and $AlCl_3$ as catalysts is certainly disputable. However, we believe the processing strategies we utilize are appropriate for waste minimization, making our approach attractive. To give better insight into this, we can make comparisons with other similar experiments. Solid acid catalysts, for example, could substitute HCl; however, the current strategies for biomass processing using solid acid catalysts provide low yields.[32, 33] Solid acid catalysts also present the additional challenge of low regenerability due to humin deposition on the surface.[34] In comparison, our system does not suffer from any deactivation. Similarly, we can consider additional Lewis acids. For example Zhao *et al.* have used $CrCl_2$, a toxic salt, as a catalyst to perform the isomerization of glucose to fructose.[35] Comparing $CrCl_2$ with $AlCl_3$ clearly shows the latter is a safer option while still offering comparable catalytic properties.

We showed that alkylphenolic solvents offer several advantages over other organics in the context of biphasic reactors in biomass processing.[21, 24, 29, 36] Specifically, HCl and $AlCl_3$ do not partition into the organic phase when using alkylphenols. This is attractive because fewer separation steps will be necessary during downstream processing, which diminishes the overall costs of process. The fact that the acids remain in the aqueous phase also implies that, in principle, they can be recovered and reused for further reactions.

Alkylphenols also provide the advantage of serving as proper solvents for the downstream processing of HMF and furfural into levulinic acid.[24] Levulinic acid can be further hydrogenated in this solvent into γ-valerolactone (GVL).[36] For the latter step, the use of a bimetallic RuSn catalyst gives high yields of GVL while preventing hydrogenation of the solvent. This allows for solvent recovery after product separation. Accordingly, by the use of an integrated processing scheme, it is possible to convert solid plant biomass into GVL while minimizing wastes by properly selecting the organic phase solvents used throughout the process chain to the desirable end product. The energy efficiency of microwave heating is very difficult to assess and must be done on a case-by-case basis.

The energy efficiency of microwave heating for lab-scale processes is usually not so good. However, in a perspective paper by Moseley and Kappe,[37] they conclude that the energy efficiency of microwave heating may, in fact, be favorable for larger-scale industrial processes. Specifically, Moseley and Kappe mention that adopting the use of microwave heating at a large-scale can produce a lower energy demand, shortening reaction times and reducing wall effects. For our reactions, the proper control of these

two variables can increase the selectivity and "contribute to another aspect of the 'greenness' of microwave heating in that less-demanding purification techniques/volumes may be possible."[37] In fact, the features of microwave heating are noticeable in our work, where by shortening reaction times and producing a more homogeneous temperature profile, the degradation of our target products was minimized.

4.4 Conclusions

The acid-catalyzed mechanical depolymerization of lignocellulosic substrates produces water-soluble oligosaccharides that are useful feedstock for the high-yield production of HMF and furfural in biphasic reactors. This is because they readily undergo hydrolysis upon microwave heating, selectively forming monosaccharides in the aqueous phase. Short reaction times are possible with the use of microwave heating and limit the extent of degradation reactions. Moreover, this work provides an ionic-liquid-free approach to processing lignocellulosic substrates into HMF and furfural with high yields. Thereby, the current results indicate that the process limitation lies no longer in the recalcitrance of lignocellulose, but in the extraction of highly reactive HMF and furfural from the aqueous phase. It is critical that new and more efficient procedures to perform the liquid−liquid extractions be developed. Further processing will be necessary for the purification or chemical transformation of these reagents, which can contribute to product losses. In addition, we understand that to establish HMF and furfural as platform chemicals, it is critical that current technologies used for the purification and downstream processing be developed to retain our reported yields. Importantly, these reaction scheme could be incorporated into the additional steps illustrated in Chapter 3, namely levulinic

acid and GVL production. However, as mentioned in the previous chapter the necessary hydrogen must be sourced through renewable paths.

4.5 Acknowledgments

The research work presented in this chapter was previously published in 2013, and is adapted here with permission from ACS Catalysis.[38]

4.6 References

1. R. Rinaldi and F. Schüth, *ChemSusChem*, 2009, **2**, 1096-1107.
2. R. Rinaldi and F. Schüth, *Energy Environ. Sci.*, 2009, **2**, 610-626.
3. C. Sievers, I. Musin, T. Marzialetti, M. B. V. Olarte, P. K. Agrawal and C. W. Jones, *Chemsuschem*, 2009, **2**, 665-671.
4. R. Rinaldi, R. Palkovits and F. Schüth, *Angewandte Chemie International Edition*, 2008, **47**, 8047-8050.
5. J. B. Binder and R. T. Raines, *Proc. Natl. Acad. Sci. USA*, 2010, **107**, 4516-4521.
6. S. M. Hick, C. Griebel, D. T. Restrepo, J. H. Truitt, E. J. Buker, C. Bylda and R. G. Blair, *Green Chemistry*, 2010, **12**, 468-474.
7. M. Benoit, A. Rodrigues, Q. Zhang, E. Fourre, K. D. O. Vigier, J.-M. Tatibouet and F. Jerome, *Angew. Chem. Int. Ed.*, 2011, **50**, 8964-8967.
8. M. Benoit, A. Rodrigues, K. De Oliveira Vigier, E. Fourré, J. Barrault, J. M. Tatibouët and F. Jérôme, *Green Chem.*, 2012, **14**, 2212-2215.
9. N. Meine, R. Rinaldi and F. Schüth, *ChemSusChem*, 2012.
10. J. Hilgert, N. Meine, R. Rinaldi and F. Schüth, *Energy and Environmental Science*, 2013, **6**, 92-96.
11. P. Kumar, D. M. Barrett, M. J. Delwiche and P. Stroeve, *Industrial & Engineering Chemistry Research*, 2009, **48**, 3713-3729.
12. R.-J. van Putten, J. C. van der Waal, E. de Jong, C. B. Rasrendra, H. J. Heeres and J. G. de Vries, *Chem. Rev.*, 2013, **113**, 1499-1597.
13. E. A. Pidko, V. Degirmenci, R. A. Van Santen and E. J. M. Hensen, *Angewandte Chemie - International Edition*, 2010, **49**, 2530-2534.
14. Y. Zhang, E. A. Pidko and E. J. M. Hensen, *Chemistry - A European Journal*, 2011, **17**, 5281-5288.
15. E. A. Pidko, V. Degirmenci and E. J. M. Hensen, *ChemCatChem*, 2012, **4**, 1263-1271.
16. S. Caratzoulas and D. G. Vlachos, *Carbohydrate Research*, 2011, **346**, 664-672.
17. V. Choudhary, R. I. Burnett, D. G. Vlachos and S. I. Sandler, *Journal of Physical Chemistry C*, 2012, **116**, 5116-5120.
18. V. Choudhary, S. I. Sandler and D. G. Vlachos, *ACS Catalysis*, 2012, **2**, 2022-2028.
19. Y. Yang, C.-W. Hu and M. M. Abu-Omar, *Chemsuschem*, 2012, **5**, 405-410.

20. Y. Yang, C. W. Hu and M. M. Abu-Omar, *Green Chem.*, 2012, **14**, 509-513.
21. Y. J. Pagán-Torres, T. Wang, J. M. R. Gallo, B. H. Shanks and J. A. Dumesic, *ACS Catal.*, 2012, **2**, 930-934.
22. S. De, S. Dutta and B. Saha, *Green Chemistry*, 2011, **13**, 2859-2868.
23. Y. Roman-Leshkov and J. A. Dumesic, *Topics in Catalysis*, 2009, **52**, 297-303.
24. P. Azadi, R. Carrasquillo-Flores, Y. J. Pagan-Torres, E. I. Gurbuz, R. Farnood and J. A. Dumesic, *Green Chem.*, 2012, **14**, 1573-1576.
25. T. F. Wang, Y. J. Pagan-Torres, E. J. Combs, J. A. Dumesic and B. H. Shanks, *Topics in Catalysis*, 2012, **55**, 657-662.
26. E. Nikolla, Y. Roman-Leshkov, M. Moliner and M. Davis, *ACS Catal.*, 2011, **1**, 408-410.
27. J. Chheda, Y. Roman-Leshkov and J. Dumesic, *Green Chem.*, 2007, **9**, 342-350.
28. Y. Roman-Leshkov, J. N. Chheda and J. A. Dumesic, *Science*, 2006, **312**, 1933-1937.
29. E. I. Gurbuz, S. G. Wettstein and J. A. Dumesic, *ChemSusChem*, 2012, **5**, 383-387.
30. M. Tonkovic and H. Bilinski, *Polyhedron*, 1995, **14**, 1025-1030.
31. R. Xing, A. Subrahmanyam, H. Olcay, W. Qi, G. van Walsum, H. Pendse and G. Huber, *Green Chem.*, 2010, **12**, 1933-1946.
32. H. Z. Chen, B. Yu and S. Y. Jin, *Bioresour. Technol.*, 2011, **102**, 3568-3570.
33. J. Hegner, K. C. Pereira, B. DeBoef and B. L. Lucht, *Tetrahedron Lett.*, 2010, **51**, 2356-2358.
34. R. Weingarten, W. C. Conner and G. W. Huber, *Energy Env. Sci.*, 2012, **5**, 7559-7574.
35. H. Zhao, J. E. Holladay, H. Brown and Z. C. Zhang, *Science*, 2007, **316**, 1597-1600.
36. D. M. Alonso, S. G. Wettstein, J. Q. Bond, T. W. Root and J. A. Dumesic, *Chemsuschem*, 2011, **4**, 1078-1081.
37. J. D. Moseley and C. O. Kappe, *Green Chemistry*, 2011, **13**, 794-806.
38. R. Carrasquillo-Flores, M. Kaldstrom, F. Schuth, J. A. Dumesic and R. Rinaldi, *Acs Catalysis*, 2013, **3**, 993-997.

Chapter 5: Water-Gas Shift Reaction on Pt-Re Catalysts: Characterization of the Active Site and Role of the Promoter

5.1 Introduction

In Chapters 3 and 4 strategies for the upgrading of biomass dealing with the upgrading and deconstruction of biomass, respectively, were presented. However, the development of renewable and efficient hydrogen harvesting schemes that tie into existing biomass processing strategies is critical to the advancement of biorefineries. In this regard, the water-gas shift (WGS) reaction can be tied into the effluent of aqueous-phase reforming steps where CO and H_2 are produced in order to remove CO and further produce H_2. The WGS reaction has received considerable attention from research and industry in the past and continues to do so but in general, the preparation of very active catalysts is far more advanced than fundamental understanding of the high catalytic activity. In this chapter the interest on and catalytic activity of bimetallic PtRe catalysts is discussed.

The WGS reaction ($H_2O + CO \rightarrow CO_2 + H_2$) is commonly used to produce H_2 from synthesis gas, [1, 2] but in fact it can take place in any system where CO and H_2O are present, such as methanol synthesis,[3, 4] methanol steam reforming,[5] aqueous-phase reforming, [6-8] catalytic combustion,[9] and Fischer-Tropsch synthesis.[10, 11] The WGS reaction has been the focus of extensive research work on Cu,[12-17] Fe,[18-20] and Ni based catalysts,[21-24] due to how inexpensive these metals are and the high catalytic activities they possess.

For the low-temperature WGS (LT-WGS) reaction, Cu-based catalysts have high performance, yet they are highly pyrophoric and can undergo deactivation by leaching

leading to loss of activity; this can be attributed to the presence of condensed H_2O or the formation of surface carbonates.[25-27] In light of this, noble metals and their alloys appear to be a promising alternative and have attracted considerable attention for the LT-WGS reactions.[12, 17, 28-37] Pt based catalysts have received particular attention for the LT-WGS reactions, because they have are both active and stable for fuel processing[32] (e.g., aqueous phase reforming of biomass derived oxygenates [6, 36, 38-41]). However, compared to Cu, Ni and Fe, Pt is expensive and therefore it would be advantageous to minimize the amount of Pt necessary while maintaining high activity.

Several studies have reported on Pt nanoparticles supported on metal oxides as catalysts for LT-WGS reactions.[11, 32, 42-47] In these studies, supports such as ceria,[48] zirconia,[49] and titania[50] were found to play an important role owing to their redox properties. The proposed mechanisms assume that the metal oxides are responsible for oxidizing CO, a fact that assumes a reduced form of the metal oxide. In a subsequent step CO is subsequently reoxidized by H_2O to produce H_2. Previously, our research group has reported on the reaction mechanism over Pt that is supported on alumina by using reaction kinetics studies, DFT calculations, and microkinetic modeling.[36] This previous study revealed the reaction mechanism to be much more complex, extending beyond the standard "surface-redox" mechanism, and it suggested that the carboxyl species, COOH, is a key intermediate, and is largely responsible for the turnover rates, whereas its isomer, formate (HCOO), is a spectator species.[36] Furthermore, a recent study, which combined experiments with theory, suggested that the active sites for LT-WGS reactions may be partially oxidized Pt centers with a single or a few metal atoms that are decorated with alkali ions.[35]

Several recent reports have indicated that the presence of Re has a beneficial role in the activity of Pt based catalysts in the LT-WGS reaction.[51-58] Although only a few experimental studies have been performed to understand the role of Re, they agree that Re provides an additional reaction pathway to activate H_2O.[51, 55, 58] In these studies, however, the Pt and Re atoms are supported on titania and zirconia, which are promoters for Pt catalyzed LT-WGS reactions themselves. The presence and collaboration of these different promotional effects make it difficult to isolate the effect of Re on the WGS reaction. Therefore, in this work a mechanistic study for the WGS reaction on Pt–Re catalysts supported on an inert support, carbon black Vulcan XC-72, is presented. In addition, DFT calculations, microkinetic modeling, and reaction kinetics experimental data are used to probe the reaction mechanism. Parameters from a DFT analysis of elementary steps on a $Pt_3Re(111)$ model surface are utilized to construct a comprehensive mean-field microkinetic model[59, 60] for probing the nature of the active sites on these catalysts.

5.2 Methods and Materials

5.2.1 Catalyst Preparation

Catalysts for the study included 5 wt% Pt, 5 wt% Re, 10 wt% Pt-Re (2:1), and 10 wt% Pt-Re (1:2), which were supported on the inert carbon black Vulcan XC-72 (CABOT). These catalysts were pre- pared as reported by Kunkes et al.[54] by incipient wetness impregnation with a chloroplatinic(IV) acid hexahydrate (Aldrich) and perrhenic acid (aqueous solution, 50–54% Re, Strem Chemicals) dissolved in deionized water. The catalysts were reduced at T = 573 K (with a heating rate of 0.5 K min-1) under a pure

hydrogen flow at standard temperature and pressure (100 cm^3 min^-1). CO chemisorption was performed in a Micromeritics ASAP 2020, and was used to determine the number of catalytically active sites.

5.2.2 Continuous Flow Reactions

WGS reaction studies in Chapter 5 were carried out in a fixed-bed down-flow reactor using a ¼" outer-diameter stainless steel tube. The temperature was measured by using a K-type thermocouple attached to the outside of the reactor. The temperature of the reactor was adjusted by using a furnace connected to a variable autotransformer power source, which was controlled with a temperature controller. The total pressure in the reactor was maintained at 1 atm, and the partial pressures of the gases were controlled by adjusting the flow-rates at the reactor inlet. The flow-rates of all gases were fixed by using calibrated mass-flow meters.

An inlet composition with between 10–25% of CO, 0–35% of H_2, 0–35% of CO_2, and 15–35% of H_2O was used, in which the remaining balance consisted of He. The gases were used as provided, with a purity of 99.99%. Steam was fed to the reactor by vaporizing Millipore-filtered, deionized liquid H_2O at T = 433 K; this was delivered by using a syringe pump (Harvard Apparatus). The feed and effluent gases were analyzed by using gas chromatography with a thermal conductivity detector (TCD). Steam was removed from the reactor effluent stream by using a water trap (trap immersed in an ice/H_2O bath).

5.2.3 Density Functional Theory Calculations

All DFT calculations performed for the Pt(111) surface are reported in the work of Grabow *et al.*[36] The DFT calculations for the Pt_3Re(111) surface were performed using the DACAPO total energy code.[61, 62] A 2 x 2 x 4 unit cell with 6 equivalent layers of vacuum was used to represent the surface as a periodic supercell (Figure 5.1). The slab consisted of four layers of metal atoms. Adsorption was allowed on only one of the exposed surfaces in which the top two surface layers were allowed to relax, whereas the bottom two layers were fixed at their bulk coordinates. Ultrasoft Vanderbilt pseudopotentials[63] were utilized to describe core-electron interactions, and the Kohn–Sham one-electron valence states were expanded in a basis of plane waves with kinetic energy below 25 Ry. The surface Brillouin zone was sampled at 18 special Chadi-Cohen k-points. Convergence was confirmed with respect to the k-point set and the number of metal layers used in the slab. The PW91 generalized gradient approximation (GGA-PW91)[64, 65] was used self-consistently for describing the exchange-correlation energy and potential. The electron density was determined by iterative diagonalization of the Kohn–Sham Hamiltonian, the Fermi-population of the Kohn–Sham states (kBT = 0.1 eV), and Pulay mixing of the resulting electron density.[66] The calculated equilibrium lattice constant for the bulk Pt_3Re alloy was 3.97 Å, which is in agreement with the experimental value of 3.90 Å.[67]

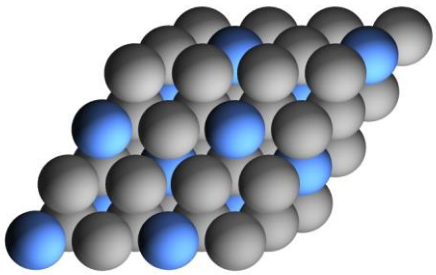

Figure 5.1. Schematic of the $Pt_3Re(111)$ surface used for the DFT calculations. Grey spheres represent Pt atoms; blue Re atoms.

Activation energy barriers for the elementary steps were calculated by using the CI-NEB method.[68-70] For determining the minimum energy pathways, a total of seven images were utilized, which included the initial and final state for each elementary step that was considered. To verify the validity of the identified transition states, vibrational frequency analysis was performed, which yielded a single negative curvature mode.

5.2.4 Microkinetic Modeling

The mean-field microkinetic models used in this work accounted for a total of 15 elementary steps. Relevant kinetic and thermodynamic parameters (e.g., pre-exponential factors, activation energies, (EAs) reaction energies, and so on) were obtained from DFT calculations by following the methodology utilized by Grabow *et al.*[36] and Gokhale *et al.*[71] Spontaneous reactions, in which no transition state was found, were assigned pre-exponential factors of 10^{13} s^{-1}. All gas-phase enthalpies and entropies were obtained from the National Institute of Standards and Technology (NIST) archives.[72] The entropy of adsorbed species was calculated as the gas-phase entropy minus the three-dimensional translational contribution $S_{trans,3D}$. To account for the vibrational and rotational contributions to the entropy of adsorbed species, a fitting factor, F_{loc}, was utilized.[73]

Our reactor was modeled as a continuously-stirred tank reactor (CSTR) with the integration and parameter optimization performed by using MATLAB (2010A, The MathWorks, Natick, MA).

5.3 Results

The proposed reaction mechanism for WGS consists of 15 elementary steps (Steps 2-16) all of which were studied thoroughly with DFT calculations on Pt(111) and $Pt_3Re(111)$ model surfaces. The overall reaction is given by Step (1). These 15 reactions encompass the redox and the COOH mechanisms:

$$CO + H_2O \leftrightarrow CO_2 + H_2 (1)$$

$$H_2O + * \leftrightarrow H_2O * (2)$$

$$CO + * \leftrightarrow CO * (3)$$

$$H_2O * + \ * \leftrightarrow OH * + H * (4)$$

$$OH * + \ * \leftrightarrow O * + H * (5)$$

$$2OH * \leftrightarrow H_2O * + O * (6)$$

$$CO * + O * \leftrightarrow CO_2 * + * (7)$$

$$CO_2 * \leftrightarrow CO_2 + * (8)$$

$$2H * \leftrightarrow H_2 + 2 * (9)$$

$$CO * + OH * \leftrightarrow COOH * + * (10)$$

$$COOH * + * \leftrightarrow CO_2 * + H * (11)$$

$$COOH * + O * \leftrightarrow CO_2 * + OH * (12)$$

$$COOH * + OH * \leftrightarrow CO_2 * + H_2O * (13)$$

$$CO_2 * + H * \leftrightarrow HCOO ** \quad (14)$$

$$HCOO ** + O * \leftrightarrow CO_2 * + OH * + * \quad (15)$$

$$HCOO ** + OH * \leftrightarrow CO_2 * + H_2O * + * \quad (16)$$

Previous research has verified the possibility of additional species such as formyl;[74] however, it is not expected that these species play a major role in the reaction mechanism and they will not be considered further in the present study. In the following sections, a more detailed description of the DFT results for the elementary steps (Steps (2)-(16) above) on the $Pt_3Re(111)$ surface is performed, and we will compare these results with the respective data on Pt(111). A summary of the results for the binding characteristics of the studied species can be found in Table 5.1. It should be noted that the preferred binding site of CO determined by DFT (hexagonal closed pack/face-centered cubic)[36, 75] differs from what is observed (atop) experimentally[76, 77].This has been discussed extensively in literature[78, 79], in which various possible explanations for the discrepancy are offered, such as temperature effects and the self-interaction error in DFT. However, the variation in stability of CO on different adsorption sites on Pt(111) is rather small (<0.2 eV), and thereby for the reaction temperatures considered here, the effect should be minimal.

In general, all reaction intermediates are stabilized further on the Pt_3Re surface, compared to that of the Pt surface.

Table 5.1. DFT-calculated binding energies (BE) and site preferences for WGS reaction intermediates. Individual adsorbates at θ = 1/4 ML coverage. Reference energy is that of the slab and the gas phase adsorbate at infinite separation from each other.

	Pt(111)		$Pt_3Re(111)$	
Adsorbate	**Site**	**BE (eV)**	**Site**	**BE (eV)**
H	Top	-2.71	top-Re	-2.81
O	Fcc	-3.73	top-Re	-6.44
OH	top tilted	-2.09	top-Re tilt	-3.74
H_2O	Top	-0.27	top-Re	-0.81
CO	fcc/hcp	-1.82	top-Re	-2.56
CO_2	No preference	-0.11	top-Re/top-Pt	-0.47
COOH	Top, H down	-2.44	top-Re/top-Pt	-2.87
HCOO	top-top	-2.31	top-Re/top-Pt	-3.29

5.3.1 Water Activation

$H_2O \rightarrow OH+H$: Adsorption of H_2O on the $Pt_3Re(111)$ surface is an exothermic process by -0.81 eV and prefers to take place at the Re top-site. The OH and H species prefer to bind atop the Re atom if they are individually adsorbed. The most stable state of coadsorbed OH and H species, formed through H_2O dissociation, involves an OH species that is adsorbed on top of the Re atom with the molecular axis tilted towards the surface normal, and an H atom that is adsorbed on top of a Pt atom. The total binding energy (BE) for the configuration is -6.24 eV.

The calculated activation energy barrier for the abstraction of the first H atom from H_2O was 0.46 eV. The surface reaction step is exothermic by -0.20 eV, and is initiated by a slight tilt of the H_2O molecule, with one H atom pointing closer to the surface. At the transition state, the abstracted H atom is attached to the side of a top-Pt site and the HO-H bond length was determined to be 1.36 Å.

OH→O+H: For co-adsorbed O and H, the most stable configuration occurs when an O atom is attached to top-Re and the H atom to top-Pt sites with a total BE of -8.94 eV. The dissociation of OH is an even more exothermic step (E = -0.60 eV) than the abstraction of the first H atom from H_2O (-0.20 eV). The activation energy barrier for OH dissociation is 0.44 eV, similar to the value for $H_2O \rightarrow OH + H$ (0.46 eV).

On Pt(111), the system has to overcome significantly higher activation energy barriers for both of the H-abstraction steps (0.88 eV and 1.09 eV, respectively[36]). Furthermore, the final decomposition from OH to atomic O and H is endothermic on Pt(111) by 0.26 eV. This comparison indicates that water activation is easier on $Pt_3Re(111)$ compared to Pt(111).

OH+OH→H_2O+O (Disproportionation Reaction): Two OH species co-adsorbed on the $Pt_3Re(111)$ surface (total coverage θ = 0.5 ML) had a total BE of -5.69 eV. At this higher coverage, OH is stabilized by 0.13 eV compared to the 1/4ML coverage case. In the most stable configuration, one OH species is attached to a top-Re site and the other OH is bound to a bridge-Pt site.

The most stable state for H_2O and O co-adsorption occurs when the O atom is bound to a top-Re site and H_2O is adsorbed on a top-Pt with an overall BE of -6.71 eV. The disproportionation of OH occurs spontaneously and the reaction is exothermic by -1.63 eV. This behavior is similar on Pt(111), where the step is also spontaneous, but the exothermicity of the step is much lower (-0.44 eV).[36]

5.3.2 Oxidation of CO by atomic oxygen

$CO + O \rightarrow CO_2$: CO_2 is found to be stable at the $Pt_3Re(111)$ surface in a bent configuration with a BE of -0.47 eV (Table 5.1) and it is bound to a Re and a Pt surface atom. Like the O atom, CO by itself is preferentially adsorbed perpendicular to a top-Re site with a BE of -2.56 eV (Table 5.1). Co-adsorbed CO and O are most stable with the CO bound to a top-Pt site and O bound to a top-Re site. For this configuration the total BE was -7.67 eV.

The activation energy barrier for CO oxidation is 1.18 eV with respect to the coadsorbed initial state; this elementary step is endothermic by 1.02 eV. CO oxidation on Pt(111) shows entirely different characteristics. The activation energy on Pt(111) is 0.75 eV with respect to co-adsorbed species, and the reaction itself is exothermic by -0.80 eV,[36] which suggests that, in contrast to water activation, CO oxidation on $Pt_3Re(111)$ is more difficult than on Pt(111) surfaces. This difference is reasonable, as H_2O activation leads to molecular fragments that bind more strongly to Pt_3Re than to Pt, whereas CO oxidation is a bond making step, in which one has to activate strongly-bound species (CO and O) to the transition state for CO_2 formation.

5.3.3 CO oxidation via COOH

$CO + OH \rightarrow COOH$: Adsorbing CO and OH simultaneously on $Pt_3Re(111)$ results in a total BE of -5.23 eV for a configuration where OH is bound perpendicular to a top-Re site and CO to a face-centered cubic-mixed site. The CO molecule is slightly tilted with the C atom closer to the Re atom. Adsorbed individually, both molecules prefer the

top-Re site with BE values of -2.56 and -3.74 eV (Table 5.1) for the CO and OH species, respectively.

In its most stable configuration, the COOH intermediate forms bonds with a top-Re site and a top-Pt site with the H atom pointing towards the surface. However, the direct formation of this structure from CO and OH is not possible. To form this configuration, first CO and OH react to $COOH_u$, where only the C atom is bound to the surface and its H atom pointing upwards away from the surface. Subsequently, $COOH_u$ realigns to the most stable $COOH_d$ configuration, with the C and O atoms bound to top-Re and H pointing downwards to the surface. The first reaction step requires an activation energy of 1.21 eV and is endothermic by 0.80 eV. At the transition state, the OC-OH bond length is 1.44 Å and the H atom points out of the OCO plane. The subsequent reorientation of $COOH_u$ to $COOH_d$ is exothermic by -0.25 eV and has an activation energy barrier of 0.37 eV. Overall, the reaction is endothermic by 0.55 eV, in contrast to the formation of COOH on Pt(111) which is exothermic by -0.45 eV.[36] In addition, energy barriers for the described reaction steps on Pt(111) are significantly lower than on $Pt_3Re(111)$ (0.46 eV and 0.32 eV, respectively).[36] Again, as discussed for $CO + O \rightarrow CO_2$ above, the formation of COOH is a bond-making step, which is less driven on the Pt-Re alloy surface as compared to Pt, for the same reasons outlined earlier.

5.3.4 COOH decomposition

$COOH \rightarrow CO_2 + H$: In the most stable configuration of co-adsorbed CO_2 and H on $Pt_3Re(111)$, the H atom is bound to a hexagonal closed pack-mixed site and CO_2 is

bound to both a top-Pt site and top-Re site in a bent configuration. This state has a total BE of -2.94 eV.

The dissociation of COOH is investigated starting from the most stable configuration with the H atom pointing towards the surface ($COOH_d$) The activation energy barrier for dissociation of $COOH_d$ to CO_2 and H is 1.23 eV and the reaction step is endothermic by 0.28 eV. Dissociation of COOH is initiated by bending of the O and H atoms toward the surface, followed by abstraction of the H atom. At the transition state, the H atom is attached to a top-Pt site and the COO-H bond length increases to 1.45 Å (from 0.98 Å in the initial configuration). Enhanced activation has been observed on Pt(111) where the dissociation of $COOH_d$ has an activation barrier of 0.78 eV and the reaction step itself is thermo-neutral.[36] The COO-H bond length of the transition state on Pt(111) is moderately longer (1.49 Å).[36]

$COOH + O \rightarrow CO_2 + OH$: In the most stable co-adsorbed state of $COOH_d$ and O, $COOH_d$ is bound to a top-Pt site and O is bound to a top-Re site. The calculated total BE for the $COOH_d$ + O initial state was -8.43 eV. Simultaneous adsorption of CO_2 and OH leads to a similar arrangement as CO_2 and H co-adsorption, where OH is bound to a top-Re site and CO_2 was physisorbed ca. 4 Å above the surface. The total BE for this final state is -3.99 eV.

The reaction of COOH and O to CO_2 and OH has an activation energy barrier of 1.11 eV and is endothermic by 0.22 eV. At the transition state, the distance between the C atom of COOH and the surface is 2.39 Å. The O*-H bond length at the transition state (*O-H-OCO) is 1.63 Å. Again, this reaction step is facilitated on pure Pt(111) with an activation barrier of 0.35 eV and an exothermicity of -0.27 eV.[36]

$COOH + OH \rightarrow CO_2 + H_2O$: The majority of the investigated configurations of co-adsorbed COOH and OH reacted spontaneously to CO_2 and H_2O, demonstrating the absence of an activation energy barrier. However, a stable configuration is found with OH bound to a top-Re site and tilted, and $COOH_d$ adsorbed on a top-Pt site with the H-atom pointing towards the surface. The total BE for this initial state is -5.91 eV. Compared to infinite separation, co-adsorbed CO_2 and H_2O (in the most stable final state) are stabilized by 0.12 eV, with the H_2O molecule attached to a top-Re site and CO_2 ca. 4 Å above a bridge-Pt site. This configuration has a total BE of -1.02 eV.

To calculate the minimum energy path for the reaction of COOH and OH to CO_2 and H_2O, it was assumed that CO_2 is formed on the surface first and it is subsequently desorbed. To verify this, an energy minimization calculation is performed for co-adsorption of CO_2 and H_2O, where the C atom of carbon dioxide is fixed in the z-direction. The calculated state has a BE of -0.86 eV and is 0.16 eV less stable than the most stable configuration for co-adsorbed H_2O and CO_2. The CI-NEB calculation yields an energy barrier of 0.17 eV for the COOH molecule to rotate to an intermediate state, which is 0.06 eV less stable than the initial state. The following transition of H from COOH to OH is endothermic by 0.11 eV without an additional energy barrier to activate the reaction. This reaction on Pt(111) is shown to occur quasi-spontaneously with a small activation barrier and without the formation of a stable intermediate species. No explicit transition state is identified and the reaction is exothermic by -0.71 eV.

5.3.5 Formate Decomposition

$HCOO \rightarrow CO_2 + O$: Besides the most stable state for CO_2 and H co-adsorption described above (BE=-2.94 eV), another state with a BE of -2.72 eV is found. In this configuration, CO_2 is non-linearly adsorbed on a top-Re site and H was bound to a hexagonal closed pack-mix site. CI-NEB calculations are performed with the latter configuration as the final state, instead of the most stable state with CO_2 bound to both a top-Re site and a top-Pt site. The activation barrier for this step is 1.38 eV, and the reaction is endothermic by 0.66 eV. Taking into account diffusion of the CO_2 molecule to the most stable configuration of CO_2 and H resulted in an endothermicity of 0.44 eV for the entire step. The reverse reaction, i.e. formate formation from CO_2 and H, is exothermic (-0.44 eV) and has an energy barrier of 0.94 eV. In contrast to Pt(111), where formate formation is modestly endothermic (by 0.35 eV) and has an energy barrier of 1.39 eV,[36] on Pt_3Re, the exothermicity and lower energy barrier enable the formation of HCOO.

$HCOO + O \rightarrow CO_2 + OH$: Coadsorption of HCOO and O leads to a slight stabilization by 0.11 eV, compared to their adsorption at infinite separation. In the most stable configuration, the O atom is located on a top-Re site and the formate is bound through its O atoms to two top-Pt sites. The total BE is found to be -8.62 eV. Using CI-NEB calculations, this step is observed to be inhibited by a significant activation energy of 1.83 eV. Furthermore, it is an endothermic step by 0.11 eV. This behavior differs markedly from what occurs on Pt(111), where an easier activation has been reported with an activation energy of 1.17 eV, and the step is exothermic by -0.60 eV.[36]

$HCOO + OH \rightarrow CO_2 + H_2O$: The most stable state of co-adsorbed HCOO and OH is similar to the coadsorption of HCOO with O. The OH species is found tilted on a top-Re site, whereas HCOO is bound through its O atoms to two top-Pt sites. The overall BE iss calculated to be -6.12 eV and is more stable by 0.29 eV than adsorption at infinite separation, indicating a relatively strong attraction between co-adsorbed HCOO and OH. The barrier for this step is 1.34 eV, and it is quasi thermo-neutral (ΔE=-0.05eV). A comparable activation barrier is observed on Pt(111) (1.23 eV); however, on Pt(111) this step is thermodynamically favored with an exothermicity of -1.04 eV.[36]

5.3.6 Coverage Dependence of CO Binding Energy

The binding energy of a specific adsorbate on a surface can depend significantly on its own surface coverage or the surface coverage of other co-adsorbed species. In particular, the binding energy of CO on transition metals surfaces is known to shown a strong dependence on its own coverage.[74] Grabow *et al*.[36] have found that the BE of CO on Pt(111), in eV, depends on coverage as described by the equation below:

$$BE_{CO}(\theta_{CO}) = -1.78 + 0.0065 \cdot exp(4.79 \cdot \theta_{CO}) + 0.031135 \cdot \theta_{CO} \cdot exp(4.79 \cdot \theta_{CO}) \quad (17)$$

This equation is used for the microkinetic modeling of Pt catalysts in this study. The use of coverage-dependent BE for other species, such as hydrogen, oxygen and others, on Pt(111) is not utilized since these effects are not nearly as significant when compared to that of CO.

To a first approximation, the microkinetic model discussed in subsequent sections for PtRe catalysts does not utilize an explicit CO-coverage dependence correlation for the

BE's. Instead, the initial guess for BE_{CO} is defined as the value obtained from the fitted Pt(111) microkinetic model by substituting into Eqn. 17 the value of the CO coverage predicted by the model for the Pt catalyst under WGS reaction conditions. The sensitivity to this parameter for the Pt-Re catalyst is determined and further optimizations of this parameter (BE_{CO}) are performed in the framework of the developed PtRe microkinetic model.

5.3.7 Microkinetic Models

The microkinetic models for three catalysts, Pt, Pt-Re(2:1) and Pt-Re(1:2), are constructed based on the parameters obtained from DFT calculations on Pt(111) and $Pt_3Re(111)$. The calculated turnover frequencies (TOF) from these models are compared with the respective experimental TOF values. Binding energies (BE), pre-exponential factors and forward activation energy barriers obtained from DFT are input to the microkinetic code as the initial guesses for the model parameters. For the case of the Pt-Re microkinetic models, two initial guesses were utilized:

1. The most favorable adsorption sites, having the highest absolute BE, on the $Pt_3Re(111)$ alloy
2. BE of species on the Pt-sites in the $Pt_3Re(111)$ alloy (i.e. Re was modeled as a promoter)

The results for each set of initial guesses are discussed in the following sections. Based on the results of Grabow *et al.*,[36] only the coverage dependence for BE_{CO} (Eq. 17) is included in the Pt model. Accordingly, the final BE_{CO} in this model is a direct result of the behavior predicted by the equation. In contrast, in the Pt-Re surface models the

binding energies were adjusted only through the microkinetic modeling optimization procedure, where the final BE_{CO} is equal to the converged value from the fit. No assumptions are made on the identity of the rate-limiting step.

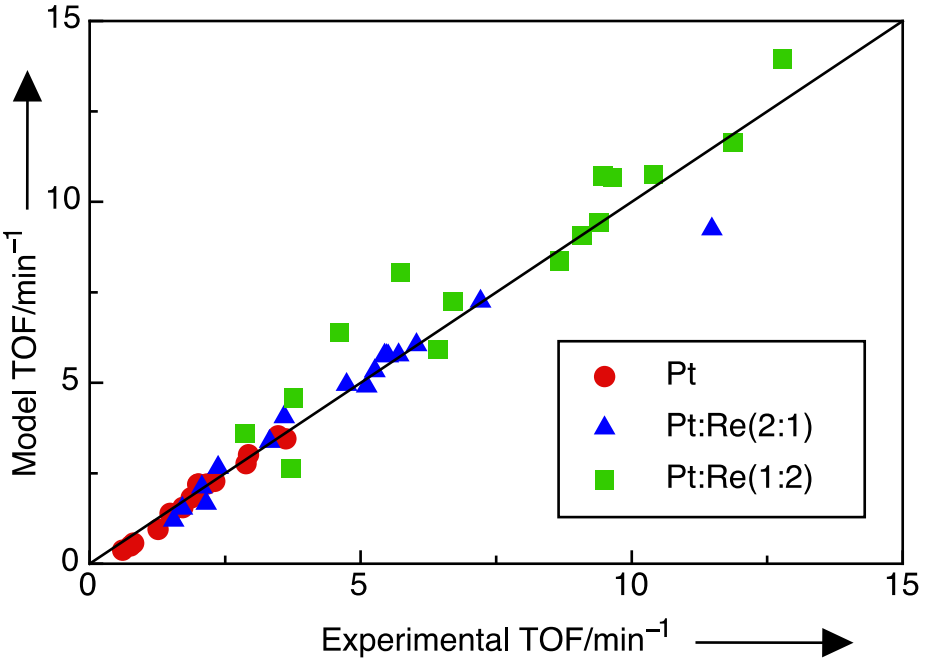

Figure 5.2. Calculated (model) versus experimental turnover frequency (TOF). The parameters used to calculate the model TOF are those obtained from fitting the experimental TOF's.

The first step was to perform a sensitivity analysis on the activation energy barriers and BE's. The results for this analysis show that for all three catalysts studied, the BE_{CO} and the activation energy barrier for step (10), carboxyl formation, are sensitive parameters. For both Pt-Re models another parameter demonstrates sensitivity, namely the activation energy barrier of step (11), carboxyl decomposition to CO_2 and H*. Decomposition of carboxyl including the reaction with surface O* and formation of CO_2 and *OH could have been expected to facilitate carboxyl decomposition. However,

resulting from the strong binding of O* to Re sites, the activation barrier is decreased only by 0.24 eV compared to the direct decomposition step(0.99 eV versus 1.23eV for the direct COOH decomposition). Having identified the sensitive parameters, we proceeded to optimize them in the respective models and the predicted TOF values were compared with experimental TOF values, as shown in Figure 5.2. The Pt(111) model shows excellent agreement with experiments, after adjusting only the DFT value for the activation energy for step (10). For the Pt-Re models, fitting of the experimental TOF values leads to larger deviations from the DFT results for the activation energy barriers of steps (10) and (11), the implications of which are discussed later.

Table 5.2 shows the predicted and experimental values of the reaction orders and apparent activation energies. The reaction orders obtained through the microkinetic models are in agreement with experiments; significant differences are observed only for H_2. In general, the models tend to overestimate the inhibiting effect of hydrogen. In all cases, CO is the most abundant surface species, $\theta_{CO} \approx 2/3$ ML, with negligible amounts of other surface species, except in the Pt-Re surfaces where approximately $\theta_H \approx 0.15$ ML is calculated. Still, the obtained apparent activation energies are in excellent agreement with experiments.

Table 5.2. Reaction Orders and Apparent Activation Energies. E_{app} in kJ/mol. Elementary step activation energies and binding energy values can be found in supporting information.

	Pt		**Pt:Re(2:1)**		**Pt:Re(1:2)**	
Species	**Experiment**	**Model**	**Experiment**	**Model**	**Experiment**	**Model**
CO	-0.20 ± 0.03	-0.20	-0.17 ± 0.02	-0.22	-0.34 ± 0.01	-0.36
CO_2	-0.03 ± 0.01	0.00	0.01 ± 0.02	0.00	-0.02 ± 0.01	-0.01
H_2	-0.37 ± 0.01	-0.48	-0.35 ± 0.01	-0.63	-0.36 ± 0.04	-0.45
H_2O	0.55 ± 0.06	0.68	0.73 ± 0.04	0.68	0.78 ± 0.07	0.77
E_{app}	74.7 ± 2.94	74.6	76.1 ± 2.33	76.2	77.6 ± 1.27	82.2

Campbell's degree of rate control was used to assess the existence of rate-determining steps:[80, 81]

$$X_{RC,i} = \frac{k_i}{r}\left(\frac{\partial r}{\partial k_i}\right)_{K_{i,eq},k_j} \quad (18)$$

Table 5.3. Kinetic parameters in the PtRe(2:1) microkinetic model obtained from $Pt_3Re(111)$ DFT at θ = 1/4 ML coverage for each of the reactants adsorbed. $E_{f,DFT}$ is the forward reaction barrier as obtained from DFT and E_f is the fitted reaction barrier from the microkinetic model shown for the experimental conditions in Table 5.4 DFT and fitted binding energies for this model are provided in supporting information.

Step	Reaction	$E_{f,DFT}$ (eV)	from microkinetic model	
			E_f (eV)	X_{RC}
(2)	$H_2O + * \leftrightarrow H_2O*$	0.0	0.0	0
(3)	$CO + * \leftrightarrow CO*$	0.0	0.0	0
(4)	$H_2O* + \ * \leftrightarrow OH* + H*$	0.46	0.46	$-3x10^{-4}$
(5)	$OH* + \ * \leftrightarrow O* + H*$	0.44	0.44	0
(6)	$2OH* \leftrightarrow H_2O* + O*$	0.0	0.0	0
(7)	$CO* + O* \leftrightarrow CO_2* + *$	1.18	1.18	0
(8)	$CO_2* \leftrightarrow CO_2 + *$	0.0	0.0	0
(9)	$2H* \leftrightarrow H_2 + 2*$	0.0	0.0	0
(10)	$CO* + OH* \leftrightarrow COOH* + *$	0.37	0.03	0.95
(11)	$COOH* + * \leftrightarrow CO_2* + H*$	1.23	0.69	$9x10^{-3}$
(12)	$COOH* + O* \leftrightarrow CO_2* + OH*$	0.99	0.99	0
(13)	$COOH* + OH* \leftrightarrow CO_2* + H_2O*$	0.33	0.33	0
(14)	$CO_2* + H* \leftrightarrow HCOO**$	0.94	0.94	0
(15)	$HCOO** + O* \leftrightarrow CO_2* + OH* + *$	1.83	1.83	0
(16)	$HCOO** + OH* \leftrightarrow CO_2* + H_2O* + *$	1.34	1.34	0

Table 5.3 shows the results of the performed analysis for PtRe. Elementary step (10) shows the highest degree of rate control for all catalysts studied. In the Pt-Re models, reaction (11) follows (10) in the degree of rate-control, but with a much lower value for step (11). The reaction rate (flux) for each elementary step is also studied in our microkinetic model, and the mechanism proceeds predominantly through water activation

(4), carboxyl formation (10) and direct carboxyl decomposition (11) in all three microkinetic models, under the conditions studied.

5.4 Discussion

5.4.1 Density Functional Theory

A potential energy surface (PES), Figure 5.3, shows the results of the DFT calculations on $Pt_3Re(111)$ as implemented in the microkinetic model (i.e. adsorbate binding energies of Pt(111) and activation energies from $Pt_3Re(111)$). The PES shows two pathways that occur via the redox mechanism, OH dissociation and OH-OH disproportionation, both generating O* on the surface, whereas the other two pathways occur via a COOH intermediate; one of these pathways is the direct decomposition (step 11) and the other is the OH-mediated decomposition (step 13). Inspection allows to identify the COOH direct decomposition path as the one with the least deviation from the average potential energy between reactants and products. The OH dissociation route and the OH+OH disproportionation route are the least plausible in this reaction system. Still, the OH dissociation reaction is favored over the disproportionation step to give surface O*. Previous DFT calculations on the WGS reaction mechanism on different morphologies of TiC have shown that the redox pathway is favored over the carboxyl pathway on nanostructures of TiC[82]. This has been attributed to the stronger binding of species, in particular oxygen[82]. A similar behavior could be expected on the Pt_3Re surface where a strong interaction of atomic oxygen with the Re atoms has been calculated. However, here, it is observed that the COOH mechanism is favorable. The strong interaction of O with Re can furthermore lead to the formation of Re-O species and prevent the Re sites from having a direct role in the WGS reaction. However, Re-O

species can possibly act as promoter for the reactions taking place on Pt sites. Formate, not shown in any of the pathways leading from reactants to products, is determined through the microkinetic models to be a spectator species, and it is formed through a reaction between surface hydrogen and CO_2. A compact representation of the WGS reaction pathways is shown in Figure 5.4. The minimum energy route is highlighted with solid arrows; the reaction proceeds through the COOH intermediate which, through subsequent elementary steps, leads to CO_2 and H_2.

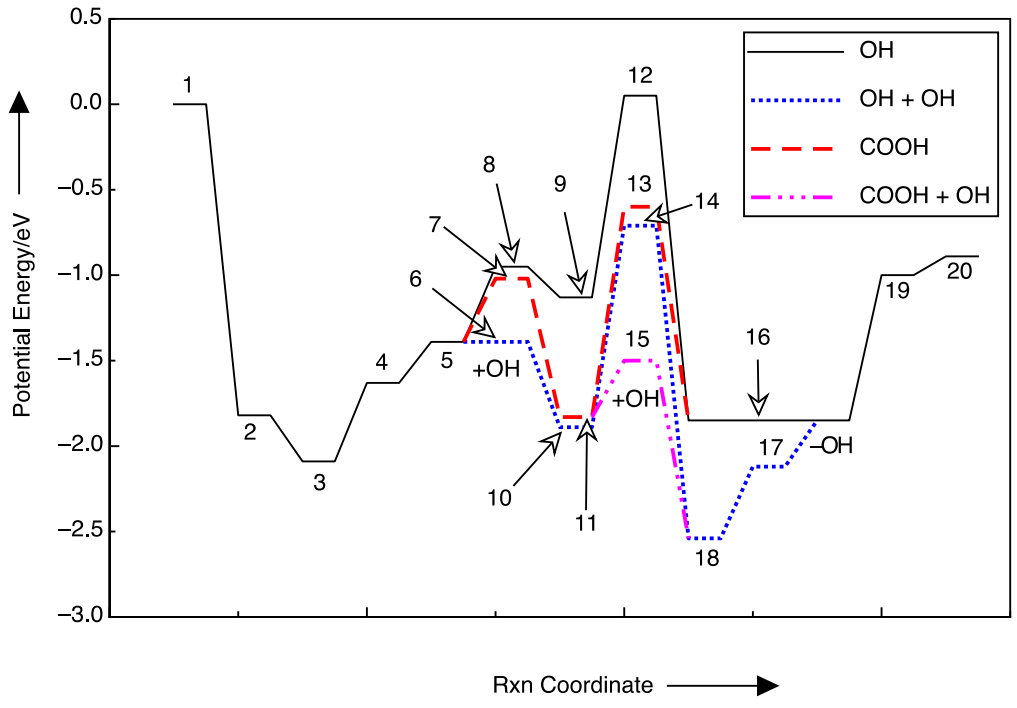

1. $CO + H_2O$
2. $CO_{ads} + H_2O$
3. $CO_{ads} + H_2O_{ads}$
4. $OH–H_{TS}$
5. $CO_{ads} + OH_{ads} + H_{ads}$
6. $O–H–OH_{TS}$
7. $CO–OH_{TS}$
8. $O–H_{TS}$
9. $CO_{ads} + 2H_{ads} + O_{ads}$
10. $CO_{ads} + H_2O_{ads} + H_{ads} + O_{ads}$
11. $COOH_{ads} + H_{ads}$
12. $CO–O_{TS}$
13. $COO–H_{TS}$
14. $CO–O_{TS}$
15. $COO–H–OH_{TS}$
16. $CO_{2,\ ads} + 2H_{ads}$
17. $OH–H_{TS}$
18. $CO_{2,\ ads} + H_2O_{ads} + H_{ads}$
19. $CO_{2,\ ads} + H_2$
20. $CO_2 + H_2$

Figure 5.3. Potential energy surface for four possible reaction paths for WGS on $Pt_3Re(111)$, based on DFT-derived parameters. Surface species are denoted with the subscript ads while transition state complexes are marked as TS. Additional OH is added/removed where needed as it is regenerated along the reaction.

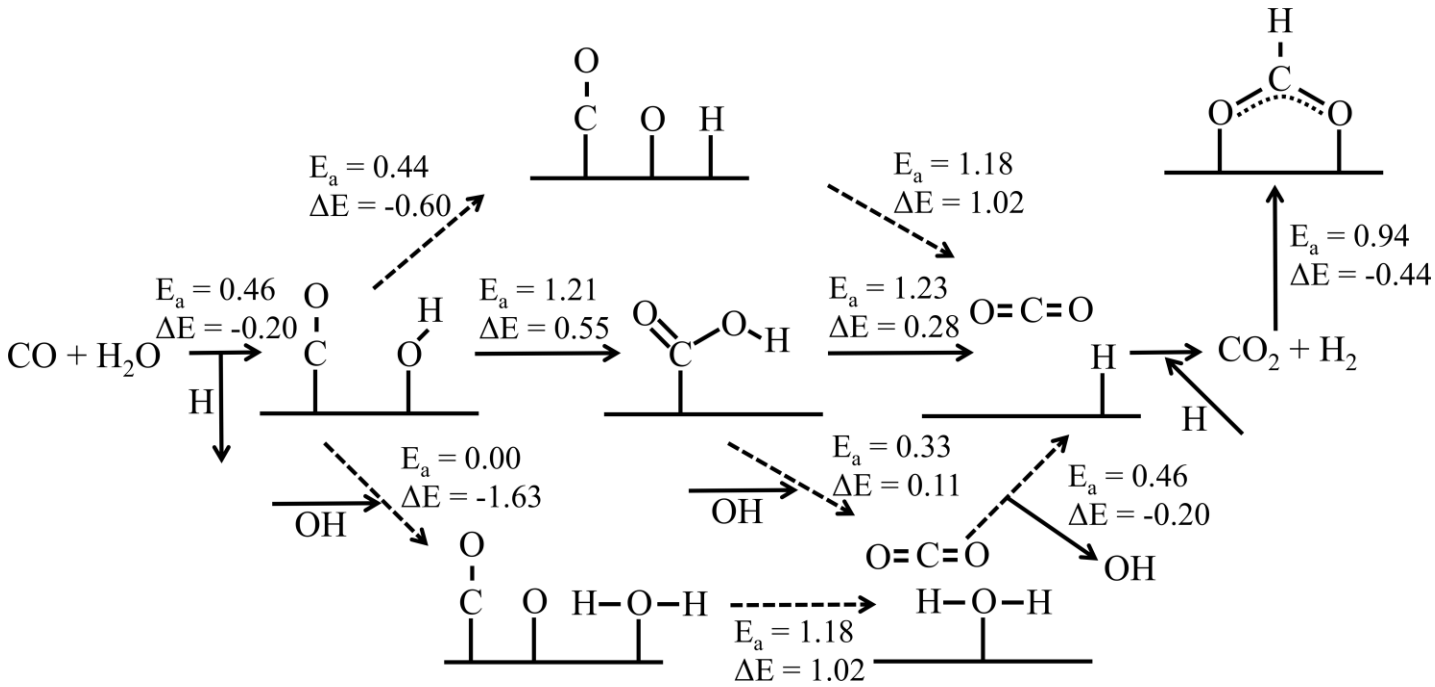

Figure 5.4. WGS reaction pathway on the $Pt_3Re(111)$ surface. For each elementary step, activation energy barrier, Ea, and reaction energy, ΔE, are shown both in eV based on the calculated DFT values. The COOH mediated pathway, highlighted by solid arrows, is found to be prevalent through a flux analysis from all microkinetic models. OH mediated pathways are hindered by low OH coverage. Formate is a spectator species only produced after the main reaction products (CO_2 and hydrogen) have been formed.

5.4.2 Microkinetic Models

Figure 5.2 and Table 5.4 demonstrate that the microkinetic models are able to capture the respective experimental results (Additional data for the remaining catalysts studied can be found in Table 5.5 and Table 5.6). The reaction orders with respect to reactants and products are predicted well, and only a few outliers are observed in the H_2 orders. Importantly, the apparent activation energies, Table 5.2, are predicted to within 6% across a wide range of working conditions.

Table 5.4. Experimental and Microkinetic model Turn over Frequencies (TOF) for the PtRe(2:1) catalyst; see also Fig. 5.4.1.1. Inlet mole fractions are provided. The total pressure was kept at P =1 atm; He served as an inert carrier gas.[a]

Exp #	Temperature (K)	y(CO)	$y(H_2O)$	$y(H_2)$	$y(CO_2)$	Experimental TOF (min^{-1})[b]	Model TOF (min^{-1})
1	548	0.15	0.25	0	0	5.70	5.77
2	548	0.2	0.25	0	0	5.26	5.33
3	548	0.1	0.25	0	0	6.03	6.05
4	548	0.25	0.25	0	0	5.11	4.91
5	548	0.15	0.15	0	0	3.59	4.06
6	548	0.15	0.2	0	0	4.74	4.95
7	548	0.15	0.35	0	0	7.21	7.25
8	548	0.15	0.25	0.15	0	2.07	2.12
9	548	0.15	0.25	0.1	0	2.37	2.66
10	548	0.15	0.25	0.25	0	1.71	1.53
11	548	0.15	0.25	0.35	0	1.55	1.20
12	548	0.15	0.25	0	0.15	5.44	5.76
13	548	0.15	0.25	0	0.25	5.48	5.75
14	548	0.15	0.25	0	0.35	5.51	5.74
15	573	0.15	0.25	0	0	11.48	9.25
16	533	0.15	0.25	0	0	3.32	3.38
17	518	0.15	0.25	0	0	2.15	1.67

[a] All experiments were carried out at a total flow rate of 100 cm^3/min.
[b] Reported values are the average of several experiments for each condition.

Table 5.5. Experimental and Calculated Turn over Frequencies (TOF) for the PtRe(1:2) catalyst. The total pressure was kept at P =1 atm; He served as inert gas.[a]

Exp #	Temperature (K)	y(CO)	$y(H_2O)$	$y(H_2)$	$y(CO_2)$	Experimental TOF (min^{-1})[b]	Model TOF (min^{-1})
1	548	0.1	0.25	0	0	11.88	11.64
2	548	0.2	0.25	0	0	9.40	9.44
3	548	0.15	0.25	0	0	10.39	10.77
4	548	0.25	0.25	0	0	8.67	8.36
5	548	0.15	0.15	0	0	6.71	7.26
6	548	0.15	0.35	0	0	12.78	13.95
7	548	0.15	0.2	0	0	9.07	9.06
8	548	0.15	0.25	0.2	0	3.76	4.57
9	548	0.15	0.25	0.05	0	5.73	8.04
10	548	0.15	0.25	0.1	0	4.61	6.39
11	548	0.15	0.25	0.3	0	2.87	3.60
12	548	0.15	0.25	0	0.15	9.46	10.72
13	548	0.15	0.25	0	0.25	9.46	10.69
14	548	0.15	0.25	0	0.35	9.65	10.66
15	573	0.15	0.25	0	0	21.52	16.77
16	533	0.15	0.25	0	0	6.42	5.92
17	518	0.15	0.25	0	0	3.72	2.64

[a] All experiments were carried out at a total flow rate of 100 cm^3/min.
[b] Reported values are the average of several experiments.

Table 5.6. Experimental and Calculated Turn over Frequencies (TOF) for the Pt catalyst. The total pressure was kept at P =1 atm; He served as inert gas.[a]

Exp #	Temperature (K)	y(CO)	$y(H_2O)$	$y(H_2)$	$y(CO_2)$	Experimental TOF (min^{-1})[b]	Model TOF (min^{-1})
1	623	0.15	0.25	0	0	2.16	2.20
2	623	0.2	0.25	0	0	2.01	2.07
3	623	0.1	0.25	0	0	2.30	2.28
4	623	0.3	0.25	0	0	1.87	1.82
5	623	0.15	0.35	0	0	2.89	2.77
6	623	0.15	0.15	0	0	1.72	1.55
7	623	0.15	0.5	0	0	3.48	3.54
8	623	0.15	0.25	0.2	0	0.75	0.49
9	623	0.15	0.25	0.05	0	1.26	0.96
10	623	0.15	0.25	0.35	0	0.61	0.37
11	623	0.15	0.25	0.15	0	0.81	0.57
12	623	0.15	0.25	0	0.15	2.00	2.20
13	623	0.15	0.25	0	0.25	2.02	2.20
14	623	0.15	0.25	0	0.35	2.00	2.20
15	608	0.15	0.25	0	0	1.48	1.39
16	638	0.15	0.25	0	0	2.93	3.01
17	648	0.15	0.25	0	0	3.62	3.45

[a] All experiments were carried out at a total flow rate of 100 cm^3/min.
[b] Reported values are the average of several experiments.

The microkinetic model based on Pt(111) shows only small changes in the parameter chosen for optimization, that is, the activation energy of reaction (10). The BE_{CO} was not adjusted from the results of DFT calculations, i.e., it was only a function of the CO coverage using equation (17). After optimization, the activation barrier for step (10) changes to 0.20 from 0.47 eV. According to equation (17), the BE_{CO} is equal to -1.26 eV at the typical value of CO coverage under WGS conditions predicted by the microkinetic model (i.e., 2/3 coverage by CO). These results are in agreement with experimental findings and the work of Grabow *et al.*[36]

The approach taken for the $Pt_3Re(111)$ models, however, is more intricate. When the surface is modeled using the most favorable adsorption sites, in most cases Re sites, the surface coverage of all species is negligible except for the atomic oxygen coverage,

which is approximately 0.98 ML in most cases. It has been previously suggested that the oxidation state of Re can alter its interaction with the support and with the other alloyed metal; in some cases Re can exist as Re^{+4} or Re^{+7}.[58, 83, 84] The high O coverage observed in our models is in agreement with these assertions. Accordingly, Re is expected to preferentially bind O atoms, and the binding of any other species will be negligible. The presence of O atoms on Re can generate repulsive interactions and destabilize nearby adsorbed species, mainly CO, thereby promoting the catalyst's overall reactivity.

The majority of the efforts in the $Pt_3Re(111)$ microkinetic models deal with the behavior of species adsorbed on pure Pt-sites, with Re serving the role of a promoter. The $Pt_3Re(111)$ models, even though similar in some aspects to the Pt(111) model, show distinct differences in the BE_{CO} and the activation barriers for elementary steps (10) and (11). The final BE_{CO} for the two Pt-Re catalysts, obtained from the microkinetic model optimization, is ca. -1.11 eV. (Note that Eqn. 17 is not used for the Pt-Re catalyst, and this binding energy corresponds to the value at the CO coverage on the catalyst under WGS reaction conditions.) For these catalysts, CO is found to be destabilized from the surface compared to the Pt(111) model, where the BE_{CO} is found to be -1.26 eV at the CO coverage on the catalyst under WGS reaction conditions. The barriers for steps (10) and (11) is significantly lowered from the calculated DFT values, with the former step occurring almost spontaneously (calculated DFT value of 0.37 eV) and the latter step having a barrier of 0.69 eV after optimization (calculated DFT value of 1.23 eV) in both Pt-Re models. The coverage of CO is approximately 2/3 ML with the coverage of H on the surface ranging from 0.15 ML to 0.2 ML.

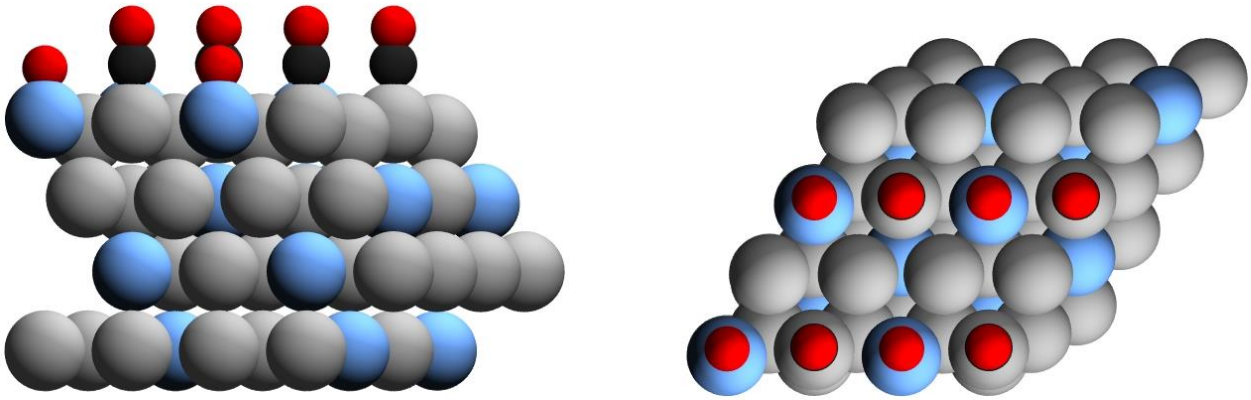

Figure 5.5. Schematic of the proposed active site on the $Pt_3Re(111)$ surface. Re (blue spheres) exist in an oxidized form while Pt (gray spheres) serves as the site for CO adsorption in this scheme.

The results obtained can be explained as follows. First, all of the studied metal surfaces operate under high coverage of CO molecules. Ojeda *et al.*[10, 85] demonstrated that the energetics of chemical reactions in highly-saturated environments are significantly different from their low coverage equivalents and that, in general, bond making reactions such as (10) and (11) are facilitated in these environments. It is also important to note that while reaction (11) had its barrier decreased considerably in the microkinetic model optimization procedure, the final fitted value is the same as for the Pt(111) surface, 0.69 eV. This similarity can be taken as an indication that this reaction proceeds mostly over Pt and is only slightly affected by the presence of the oxidized Re, if at all. Second, the fitted BE_{CO} for both PtRe models is approximately 0.15 eV lower than on Pt(111). Previously, it was stated that there is a high probability for the Re atoms to be bonded to surface O atoms and that the presence of these Re-O species can destabilize the CO binding on the nearby Pt sites. Accordingly, the weaker binding of CO molecules is likely to increase their reactivity and correspondingly enhance the measured

reaction rates. Zhang *et al.*[86] have documented a similar effect on the electrocatalytic oxygen reduction reaction. Given the above insights, Figure 5.5 gives a graphical representation of a possible structure for the active site on the $Pt_3Re(111)$ surface.

5.4.3 Rate Determining Step.

The results of the Campbell's degree of rate control analysis indicate that the formation of COOH from CO and OH is the step with the highest effect on the overall reaction rates for all studied catalysts. However, it is important to note that this reaction is dependent on the availability of both CO and OH on the catalyst surface. It was previously mentioned that the CO coverage in all models was approximately 2/3 ML, and therefore it is highly unlikely that the CO coverage would be a limiting factor. On the other hand, OH coverage is negligible in all of the models. In the proposed reaction scheme, OH is produced on the surface through water activation, step (4). In fact, the reaction rates (flux) for water activation (4), carboxyl formation (10) and the direct carboxyl decomposition (11) are dominant throughout the reaction network. When all of the observations are put together it is inferred that water activation, step (4), is the underlying rate-controlling step. After carboxyl is formed in step (10), it prefers to directly decompose via step (11). Increasing amounts of H_2O in the reactor inlet promote higher coverages of OH and increase overall reaction rates. This behavior is in agreement with the positive reaction order for H_2O observed in our experiments, in our microkinetic models and also with previous studies.[57, 87, 88]

5.5 Conclusions

DFT calculations, experimental reaction kinetics measurements and microkinetic models have been utilized to study and understand the mechanism of the WGS reaction over Pt and Pt-Re alloys. DFT-derived pre-exponential factors, binding energies and activation energies were used to construct a microkinetic model capable of simulating the observed experimental reactions rates and orders for the low temperature WGS reaction. The Pt(111) model showed remarkable agreement between model, experiments and DFT results, indicating that Pt(111) is a reasonable representation of the active site for this reation. On the other hand, the Pt-Re models diverged significantly from the DFT-derived parameter set for the $Pt_3Re(111)$ surface, suggesting that the active site is quite different than that provided by the $Pt_3Re(111)$ model surface. Steps, defects or more complicated structures such as mixed metal-metal oxides might be better representations of the active site. In all cases, the overall apparent activation energies were predicted to within 6% of the experimental values. CO was determined to be the most abundant surface intermediate with a coverage of approximately 2/3 ML. Formate was identified as a spectator byproduct species produced from a recombination of the main reaction products, CO_2 and H_2. Carboxyl, COOH, was found to be a key intermediate, responsible for turning the reactants into products. Based on the DFT results alone, the OH-assisted decomposition of COOH into CO_2 and H_2 was highly preferred; however, this pathway was kinetically hindered by a low OH coverage. Instead, the reaction proceeds through the direct decomposition of COOH, which, at the conditions studied, produces the majority of CO_2. The redox mechanism was found to have minimal contributions for all conditions studied.

The methodology outlined in this work is a step towards the rational design and the synthesis of improved catalysts. Through the combination of experimental reaction kinetic measurements, density functional theory calculations and microkinetic modeling it was possible to explain the effect of the second metal and its role in the catalytically active site. The knowledge acquired on the state of the catalyst is an important step in understanding the interaction between a highly reducible metal, Pt, and an oxophilic metal, Re, which ultimately enables the increased activity observed in these alloys. More importantly this work demonstrates the potential of this combined approach for elucidating fundamental information of a catalyst.

5.6 Acknowledgments

The research work presented in this chapter was previously published in 2013, and is adapted here with permission from ChemCatChem.[89]

5.7 References

1. J. A. Rodriguez, *Catal. Today*, 2011, **160**, 3-10.
2. C. R. F. Lund, J. E. Kubsh and J. A. Dumesic, *Acs Symposium Series*, 1985, **279**, 313-338.
3. L. C. Grabow and M. Mavrikakis, *ACS Catal.*, 2011, **1**, 365-384.
4. T. S. Askgaard, J. K. Norskov, C. V. Ovesen and P. Stoltze, *J. Catal.*, 1995, **156**, 229-242.
5. B. A. Peppley, J. C. Amphlett, L. M. Kearns and R. F. Mann, *Appl. Catal., A*, 1999, **179**, 21-29.
6. R. D. Cortright, R. R. Davda and J. A. Dumesic, *Nature*, 2002, **418**, 964-967.
7. G. W. Huber, J. W. Shabaker and J. A. Dumesic, *Science*, 2003, **300**, 2075-2077.
8. S. Kandoi, J. Greeley, D. Simonetti, J. Shabaker, J. A. Dumesic and M. Mavrikakis, *J. Phys. Chem. C*, 2011, **115**, 961-971.
9. J. H. Lee and D. L. Trimm, *Fuel Process. Technol.*, 1995, **42**, 339-359.
10. M. Ojeda, A. W. Li, R. Nabar, A. U. Nilekar, M. Mavrikakis and E. Iglesia, *J. Phys. Chem. C*, 2010, **114**, 19761-19770.
11. B. Jager and R. Espinoza, *Catalysis Today*, 1995, **23**, 17-28.

12. N. Schumacher, A. Boisen, S. Dahl, A. A. Gokhale, S. Kandoi, L. C. Grabow, J. A. Dumesic, M. Mavrikakis and I. Chorkendorff, *J Catal*, 2005, **229**, 265-275.
13. A. A. Gokhale, J. A. Dumesic and M. Mavrikakis, *J. Am. Chem. Soc.*, 2008, **130**, 1402-1414.
14. R. J. Madon, D. Braden, S. Kandoi, P. Nagel, M. Mavrikakis and J. A. Dumesic, *J Catal*, 2011, **281**, 1-11.
15. N. A. Koryabkina, A. A. Phatak, W. F. Ruettinger, R. J. Farrauto and F. H. Ribeiro, *J. Catal.*, 2003, **217**, 233-239.
16. X. Wang, J. A. Rodriguez, J. C. Hanson, D. Gamarra, A. Martinez-Arias and M. Fernandez-Garcia, *J Phys Chem B*, 2006, **110**, 428-434.
17. J. A. Rodriguez, P. Liu, J. Hrbek, J. Evans and M. Perez, *Angew. Chem. Int. Ed. Engl.*, 2007, **46**, 1329-1332.
18. R. B. King, C. C. Frazier, R. M. Hanes and A. D. King, *J. Am. Chem. Soc.*, 1978, **100**, 2925-2927.
19. G. P. van der Laan and A. A. C. M. Beenackers, *Applied Catalysis A: General*, 2000, **193**, 39-53.
20. S. Natesakhawat, X. Q. Wang, L. Z. Zhang and U. S. Ozkan, *J. Mol. Catal. A: Chem.*, 2006, **260**, 82-94.
21. L. Barrio, A. Kubacka, G. Zhou, M. Estrella, A. Martinez-Arias, J. C. Hanson, M. Fernandez-Garcia and J. A. Rodriguez, *J. Phys. Chem. C*, 2010, **114**, 12689-12697.
22. P. Liu, J. A. Rodriguez, Y. Takahashi and K. Nakamura, *J. Catal.*, 2009, **262**, 294-303.
23. W. Wen, J. E. Calderon, J. L. Brito, N. Marinkovic, J. C. Hanson and J. A. Rodriguez, *J. Phys. Chem. C*, 2008, **112**, 2121-2128.
24. R. C. Catapan, A. A. M. Oliveira, Y. Chen and D. G. Vlachos, *J. Phys. Chem. C*, 2012, **116**, 20281-20291.
25. H. Kusar, S. Hocevar and J. Levec, *Appl. Catal., B*, 2006, **63**, 194-200.
26. C. Wheeler, A. Jhalani, E. J. Klein, S. Tummala and L. D. Schmidt, *J. Catal.*, 2004, **223**, 191-199.
27. A. B. Mhadeshwar and D. G. Vlachos, *Catal. Today*, 2005, **105**, 162-172.
28. J. A. Rodriguez, S. Ma, P. Liu, J. Hrbek, J. Evans and M. Perez, *Science*, 2007, **318**, 1757-1760.
29. X. Wang, J. A. Rodriguez, J. C. Hanson, M. Perez and J. Evans, *J. Chem. Phys.*, 2005, **123**, 221101.
30. J. B. Park, J. Graciani, J. Evans, D. Stacchiola, S. D. Senanayake, L. Barrio, P. Liu, J. Fdez Sanz, J. Hrbek and J. A. Rodriguez, *J. Am. Chem. Soc.*, 2010, **132**, 356-363.
31. W. Q. Xu, R. Si, S. D. Senanayake, J. Llorca, H. Idriss, D. Stacchiola, J. C. Hanson and J. A. Rodriguez, *J. Catal.*, 2012, **291**, 117-126.
32. A. A. Phatak, N. Koryabkina, S. Rai, J. L. Ratts, W. Ruettinger, R. J. Farrauto, G. E. Blau, W. N. Delgass and F. H. Ribeiro, *Catal. Today*, 2007, **123**, 224-234.
33. N. Guo, B. R. Fingland, W. D. Williams, V. F. Kispersky, J. Jelic, W. N. Delgass, F. H. Ribeiro, R. J. Meyer and J. T. Miller, *Phys Chem Chem Phys*, 2010, **12**, 5678-5693.

34. J. H. Pazmino, M. Shekhar, W. D. Williams, M. C. Akatay, J. T. Miller, W. N. Delgass and F. H. Ribeiro, *J. Catal.*, 2012, **286**, 279-286.
35. Y. Zhai, D. Pierre, R. Si, W. Deng, P. Ferrin, A. U. Nilekar, G. Peng, J. A. Herron, D. C. Bell, H. Saltsburg, M. Mavrikakis and M. Flytzani-Stephanopoulos, *Science*, 2010, **329**, 1633-1636.
36. L. C. Grabow, A. A. Gokhale, S. T. Evans, J. A. Dumesic and M. Mavrikakis, *Journal of Physical Chemistry C*, 2008, **112**, 4608-4617.
37. J. Knudsen, A. U. Nilekar, R. T. Vang, J. Schnadt, E. L. Kunkes, J. A. Dumesic, M. Mavrikakis and F. Besenbacher, *J. Am. Chem. Soc.*, 2007, **129**, 6485-6490.
38. D. M. Alonso, J. Q. Bond and J. A. Dumesic, *Green Chem.*, 2010, **12**, 1493-1513.
39. G. W. Huber, J. W. Shabaker, S. T. Evans and J. A. Dumesic, *Appl. Catal., B*, 2006, **62**, 226-235.
40. G. W. Huber and J. A. Dumesic, *Catal. Today*, 2006, **111**, 119-132.
41. R. R. Davda, J. W. Shabaker, G. W. Huber, R. D. Cortright and J. A. Dumesic, *Appl. Catal., B*, 2005, **56**, 171-186.
42. D. S. Newsome, *Catalysis Reviews-Science and Engineering*, 1980, **21**, 275-318.
43. D. C. Grenoble, M. M. Estadt and D. F. Ollis, *J Catal*, 1981, **67**, 90-102.
44. C. N. Satterfield, *Heterogeneous catalysis in industrial practice*, McGraw-Hill, New York, 2nd edn., 1991.
45. C. Rhodes, G. J. Hutchings and A. M. Ward, *Catalysis Today*, 1995, **23**, 43-58.
46. M. S. Wainwright and D. L. Trimm, *Catalysis Today*, 1995, **23**, 29-42.
47. C. V. Ovesen, B. S. Clausen, B. S. Hammershoi, G. Steffensen, T. Askgaard, I. Chorkendorff, J. K. Norskov, P. B. Rasmussen, P. Stoltze and P. Taylor, *J Catal*, 1996, **158**, 170-180.
48. T. Bunluesin, R. J. Gorte and G. W. Graham, *Appl. Catal., B*, 1998, **15**, 107-114.
49. P. O. Graf, D. J. M. de Vlieger, B. L. Mojet and L. Lefferts, *J. Catal.*, 2009, **262**, 181-187.
50. P. Panagiotopoulou, A. Christodoulakis, D. I. Kondarides and S. Boghosian, *J. Catal.*, 2006, **240**, 114-125.
51. K. G. Azzam, I. V. Babich, K. Seshan, B. L. Mojet and L. Lefferts, *ChemCatChem*, 2013, **5**, 557-564.
52. L. Dorazio, W. Ruettinger, M. Castaldi and R. Farrauto, *Top. Catal.*, 2008, **51**, 68-75.
53. W. Ruettinger, X. S. Liu, X. M. Xu and R. J. Farrauto, *Top. Catal.*, 2008, **51**, 60-67.
54. E. Kunkes, D. Simonetti, J. Dumesic, W. Pyrz, L. Murillo, J. Chen and D. Buttrey, *J. Catal.*, 2008, **260**, 164-177.
55. K. G. Azzam, I. V. Babich, K. Seshan and L. Lefferts, *Appl. Catal., B*, 2008, **80**, 129-140.
56. K. G. Azzam, I. V. Babich, K. Seshan and L. Lefferts, *J. Catal.*, 2007, **251**, 163-171.
57. R. Radhakrishnan, R. R. Willigan, Z. Dardas and T. H. Vanderspurt, *Applied Catalysis B-Environmental*, 2006, **66**, 23-28.
58. H. Iida and A. Igarashi, *Appl. Catal., A*, 2006, **303**, 192-198.
59. J. A. Dumesic, *The Microkinetics of heterogeneous catalysis*, American Chemical Society, Washington, DC, 1993.

60. R. D. Cortright and J. A. Dumesic, *Advances in Catalysis, Vol 46*, 2002, **46**, 161-264.
61. B. Hammer, L. B. Hansen and J. K. Norskov, *Physical Review B*, 1999, **59**, 7413-7421.
62. J. Greeley, J. K. Norskov and M. Mavrikakis, *Annu Rev Phys Chem*, 2002, **53**, 319-348.
63. D. Vanderbilt, *Phys Rev B Condens Matter*, 1990, **41**, 7892-7895.
64. J. P. Perdew, J. A. Chevary, S. H. Vosko, K. A. Jackson, M. R. Pederson, D. J. Singh and C. Fiolhais, *Phys Rev B Condens Matter*, 1992, **46**, 6671-6687.
65. J. A. White and D. M. Bird, *Phys Rev B Condens Matter*, 1994, **50**, 4954-4957.
66. G. Kresse and J. Furthmuller, *Computational Materials Science*, 1996, **6**, 15-50.
67. B. N. Grgur, N. M. Markovic and P. N. Ross, *Electrochimica Acta*, 1998, **43**, 3631-3635.
68. A. Ulitsky and R. Elber, *Journal of Chemical Physics*, 1990, **92**, 1510-1511.
69. G. Mills, H. Jonsson and G. K. Schenter, *Surface Science*, 1995, **324**, 305-337.
70. G. Henkelman, B. P. Uberuaga and H. Jonsson, *Journal of Chemical Physics*, 2000, **113**, 9901-9904.
71. A. A. Gokhale, J. A. Dumesic and M. Mavrikakis, *Journal of the American Chemical Society*, 2008, **130**, 1402-1414.
72. National Institute of Standards and Technology (U.S.), *Journal*.
73. R. D. Cortright and J. A. Dumesic, *Advances in Catalysis, Vol 46*, 2001, **46**, 161-264.
74. J. Greeley and M. Mavrikakis, *J. Am. Chem. Soc.*, 2002, **124**, 7193-7201.
75. D. C. Ford, Y. Xu and M. Mavrikakis, *Surf. Sci.*, 2005, **587**, 159-174.
76. A. M. Baro and H. Ibach, *J Chem Phys*, 1979, **71**, 4812-4816.
77. G. S. Blackman, M. L. Xu, D. F. Ogletree, M. A. Vanhove and G. A. Somorjai, *Phys Rev Lett*, 1988, **61**, 2352-2355.
78. P. J. Feibelman, B. Hammer, J. K. Norskov, F. Wagner, M. Scheffler, R. Stumpf, R. Watwe and J. Dumesic, *J Phys Chem B*, 2001, **105**, 4018-4025.
79. R. A. Olsen, P. H. T. Philipsen and E. J. Baerends, *J Chem Phys*, 2003, **119**, 4522-4528.
80. C. T. Campbell, *Topics in Catalysis*, 1994, **1**, 353-366.
81. C. T. Campbell, *J. Catal.*, 2001, **204**, 520-524.
82. F. Vines, J. A. Rodriguez, P. Liu and F. Illas, *J Catal*, 2008, **260**, 103-112.
83. M. Garland, A. Baiker and A. Wokaun, *Ind. Eng. Chem. Res.*, 1991, **30**, 440-447.
84. M. Johnson, *J. Catal.*, 1974, **35**, 434-440.
85. M. Ojeda, R. Nabar, A. U. Nilekar, A. Ishikawa, M. Mavrikakis and E. Iglesia, *J. Catal.*, 2010, **272**, 287-297.
86. J. Zhang, M. B. Vukmirovic, K. Sasaki, A. U. Nilekar, M. Mavrikakis and R. R. Adzic, *J. Am. Chem. Soc.*, 2005, **127**, 12480-12481.
87. J. Bergeld, B. Kasemo and D. V. Chakarov, *Surf. Sci.*, 2001, **495**, L815-L820.
88. A. Luengnaruemitchai, S. Osuwan and E. Gulari, *Catal. Commun.*, 2003, **4**, 215-221.
89. R. Carrasquillo-Flores, J. M. R. Gallo, K. Hahn, J. A. Dumesic and M. Mavrikakis, *Chemcatchem*, 2013, **5**, 3690-3699.

Chapter 6: Formic Acid Decomposition on Au Catalysts: Characterization of the Active Site

6.1 Introduction

In Chapter 5 a combined approach using experimental reaction kinetics measurements, density functional theory (DFT) calculations and microkinetic modeling was demonstrated as a powerful method to elucidate fundamental information for a PtRe catalyst used in the water-gas shift reaction. As mentioned before the water-gas shift reaction can be utilized to produce H_2 from synthesis gas, fitting into the proposed biomass-processing scheme after an aqueous-phase reforming step. Another possibility to produce H_2 is to catalytically decompose formic acid (FA, HCOOH), a by-product during the production of levulinic acid from 5-hydroxymethyl-furfural, to produce H_2 and CO_2.

FA is a major byproduct in biomass processing,[1] and it has attracted significant attention as a potential hydrogen-carrier material.[2-7] As a hydrogen-carrier, it is possble to oxidize FA in direct formic acid fuel cells (DFAFCs).[8] When generated as an equimolar by-product of levulinic acid[9, 10] production from cellulosic biomass, FA can be used for *in situ* harvesting H_2 that can then be correspondingly utilized for the hydrogenation of levulinic acid to gamma-valerolactone,[11] thereby eliminating the need of an external hydrogen source in the production of this key biofuel precursor.[12, 13] Also, as the simplest carboxylic acid, FA has for long been used as a probe molecule in homogeneous and heterogeneous catalysis, and surface science studies, to study the reactivity on metals,[14-22] metal carbides,[23-25] and metal oxides[26-31] specifically for deoxygenation of more complex carboxylic acids, which is a critical step in the selective upgrading of biomass derived platform molecules to fuels. Hence, this study of the FA decomposition reaction has been motivated by (1) its potential application as a promising liquid hydrogen carrier for *in situ*

hydrogen production and (2) its suitability as a fundamental probe molecule for understanding the reactivity of carboxylic acids on metal catalysts, and using this information to design improved catalysts for the effective deoxygenation of these functional groups. FA decomposition can take place via two parallel pathways involving dehydrogenation or dehydration reactions, which are linked by the water gas shift (WGS)[32-34] reaction. In the broader context of FA decomposition on transition metals, steering selectivity toward production of CO_2 and H_2 (dehydrogenation), rather than CO and H_2O (dehydration) presents an important selectivity challenge in this catalytic chemistry. Even though the dehydration products can be transformed to CO_2 and H_2 via the WGS reaction, forming the dehydration products may lead to partial poisoning of catalytic sites by CO, thereby limiting the efficiency of the overall catalysis. Accordingly, supported Pt catalysts have frequently been suggested to be the most active catalysts for selective FA dehydrogenation, and for this reason, they have found widespread applications as the anode material for DFAFCs.[35-41] Yet, major obstacles are present in using Pt-based catalysts as electrode materials and as FA decomposition catalysts, because of the vulnerability of Pt to CO poisoning[42-44], which is only prevented at extremely low CO concentrations, and its dissolution under the operating conditions necessary in fuel cells.

Gold, on the other hand, is not hindered by CO poisoning under most reaction conditions. Ever since Haruta *et al.*[45] and Hutchings[46] first predicted Au to be an extraordinary catalyst for CO oxidation and ethylene hydrochlorination reactions, there has been vast interest in exploring the application of supported Au catalysts in both homogeneous and heterogeneous catalysis.[47-55] More recently, Au has been studied as a

catalyst for FA decomposition.[56] In particular, Ojeda and Iglesia[57] studied the FA decomposition on supported Au catalysts and showed that the turnover frequencies (TOFs) on Au catalysts can be higher than those on Pt catalysts if the Au is well-dispersed. This unprecedented activity on Au catalysts was proposed to arise from small Au clusters, most likely undetected in transmission electron microscopy (TEM) micrographs. More recently, Gazsi *et al.*[58] performed vapor-phase experiments to study the effect of supports on the selectivity of FA decomposition to the dehydration and dehydrogenation products, and confirmed the high activity of Au nanoparticles supported on a wide range of porous and nonporous supports. Although these experimental studies shed light on the possible nature of active sites on Au catalysts, a molecular level understanding of this reaction mechanism is still lacking and necessary for the design of highly active Au catalysts. In this work, the combined integrated approach employed in Chapter 5 is used to shed additional light into the reaction mechanism and the nature of active sites on Au catalysts. In particular, Au(111), Au(100), and Au(211) model surfaces are studied with DFT calculations to derive initial guesses for the surface reaction energetics needed for the microkinetic model. A comprehensive mean-field microkinetic model is then developed including all elementary steps investigated by the DFT calculations. Comparisons between microkinetic modeling reaction rates and reaction orders with the experimental results provide critical insights for the nature of the active site on Au/SiC catalysts for FA decomposition.

6.2 Method and Materials

6.2.1 Catalyst Preparation

SiC is chosen as the preferred support for our reaction kinetics experiments because (1) it is an inert support that does not contribute to the overall reaction rate and (2) it results in a clear contrast for Au atoms and clusters in the scanning transmission electron microscopy (STEM) micrographs, due to the large difference in the scattering potentials of the metal and the support. A 1 wt% Au/SiC catalyst was prepared by the deposition-precipitation method. 2.0 g of dry acid-treated silicon carbide was dispersed in 100 mL of a 1 mM chloroauric acid (Sigma-Aldrich) solution at room temperature. The pH of the mix was adjusted to 9 by drop-wise addition of 2.5 M ammonium hydroxide (Sigma-Aldrich). The mixture was aged for 6 h under stirring at room temperature and was then filtered and washed with deionized water to remove chloride ions. The sample was dried overnight at 373 K. The dried catalyst was reduced *in situ*, prior to the reaction at a temperature between 623 and 773 K (with a heating rate of 0.5 K min^{-1}) under pure hydrogen flow (30 cm^3 STP min^{-1}) for 4 h. Catalyst reductions at temperatures above 773 K (and up to 1073 K) were performed in a quartz flow-through cell under the same operating conditions.

6.2.2 Continuous Flow Reactions

Gas phase FA decomposition studies were conducted in a fixed-bed down-flow reactor containing 120 mg of catalyst mixed with silica chips in a 1/2-inch outer diameter stainless steel tube. The temperature was measured using a K-type thermocouple attached to the outside of the reactor. The temperature of the reactor was adjusted using a furnace

connected to a variable autotransformer power source controlled with a temperature controller. The total pressure in the reactor was maintained at 1 atm, and the partial pressures of the gases were controlled by adjusting the flow rates at the reactor inlet. The flow rates of all gases were fixed using calibrated mass-flow meters, and the total inlet flow rate was maintained at 100 mL min^{-1} for all experimental runs. An inlet composition between 0–6% of H_2, 0–6% of CO_2, and 1–4% of FA was used, with the balance consisting of helium. The gases were used as provided, with a purity of 99.99%. Liquid FA (Sigma-Aldrich) was delivered to the reactor system at room temperature using a syringe pump (Harvard Apparatus) and vaporized at the reactor inlet. The feed and effluent gases were analyzed using gas chromatography (with a Thermal Conductivity Detector (TCD)). All the experimental rates reported in this study are based on FA converted, which is equal to the amount of CO_2 produced, as no measurable amount of CO is formed under any experimental condition. To ensure this, the TCD used to analyze CO in the effluent gas mixture was first calibrated using commercial CO gas mixtures with known concentrations. Control experiments with only the SiC support in the reactor provided signals that corresponded to a concentration of 24 ± 1 ppm of CO. The CO concentrations that were obtained during our kinetic experiments under all reaction conditions were found to be very close to this value (max = 27.0 ppm, min = 23.2 ppm, average over all the runs = 25.1 ± 2 ppm). The carbon balance was verified for all experimental runs and was found to be in the range of 98.9–99.9%. Conversions were maintained below 20% to achieve differential reactor operation. To determine the apparent activation energy barrier, the temperature was varied over a range of 50 K, with

the concentrations kept at standard conditions. The apparent reaction orders with respect to reactants and products were determined by varying one gas concentration at a time.

6.2.3 Scanning Transmission Electron Microscopy

The particle-size distributions were determined from (STEM) images. STEM characterization was performed using a FEI Titan STEM with CEOS probe aberration corrector operated at 200 kV with spatial resolution of < 0.1 nm. For imaging, a high-angle annular dark-field (HAADF) Z-contrast STEM was used, with HAADF detector angle ranging from 54 to 270 mrad, probe convergence angle of 24.5 mrad, and probe current of ≈ 25 pA. To prepare samples for STEM, the catalyst samples were first suspended in ethanol, ultrasonicated for 5 min, and then deposited onto a ≈ 5 nm thick Si window TEM grids. STEM samples were plasma cleaned for 10 min with 20% O_2 + 80% Ar gas immediately before loading into the microscope.

The particle-size distributions of the Au/SiC catalysts were calculated from the acquired STEM images. From the particle-size distributions, the number average Au particle sizes were determined using the relation $\mathrm{d} = \Sigma_{\mathrm{i}} \frac{\mathrm{d_i}}{\mathrm{n}}$, where d_i is the particle diameter of each Au particle, n is the total number of Au particles counted from the STEM images of a given sample, and the summation was performed over all the particles that were identified in the STEM images.

6.2.4 Density Functional Theory Calculations

All calculations were performed using the DACAPO total energy code.[59, 60] The Au catalyst was modeled by the (111), (100), and (211) facets of the fcc bulk crystalline structure of Au metal (Figure 6.1).

The Au(111) surface was modeled by a three-layer slab with a p(3 x 3) unit cell, corresponding to 1/9 monolayer (ML) coverage for a single adsorbate in the unit cell, periodically repeated in a super cell geometry with five equivalent layers of vacuum between any two successive metal slabs. All the Au atoms in this model surface were kept fixed in their bulk truncated positions, as systematic investigations showed that surface relaxation does not have a significant effect on the energetics for this system. The super cell used to model the Au(100) facet consists of a p(3 x 3) unit cell with four layers of metal atoms, top two of which were allowed to relax, and five equivalent layers of vacuum spacing separating the periodic slab images. The Au(211) slab is constructed by a 1 x 3 unit cell and consisted of nine Au layers (having terrace three atoms deep and three atoms wide). Successive slabs were separated by a vacuum equivalent to 12 such Au(211) layers. Adsorption is allowed on only one of the two exposed surfaces for all three slabs, and the electrostatic potential was adjusted accordingly.[61, 62] The surface Brillouin zone of (111) slabs is sampled at 18 special Chadi–Cohen[63] k-points, whereas that for the (100) and (211) slabs is sampled using a 4 x 4 x 1 Monkhorst–Pack[64] k-point mesh. Ionic cores are described by ultrasoft Vanderbilt pseudopotentials[65] and the Kohn–Sham one-electron valence states are expanded in a basis of plane waves below a kinetic energy of 25 Ry. The exchange-correlation energy and potential are described self-consistently using the generalized gradient approximation (GGA-PW91).[66, 67] The

electron density is determined by iterative diagonalization of the Kohn–Sham Hamiltonian, Fermi population of the Kohn–Sham states (kBT = 0.1 eV), and Pulay mixing of the resulting electronic density.[68] The total energies are then extrapolated to kBT = 0 eV. The calculated equilibrium lattice constant for bulk Au is found to be 4.18 Å, in reasonable agreement with the experimental value (4.08 Å).[69]

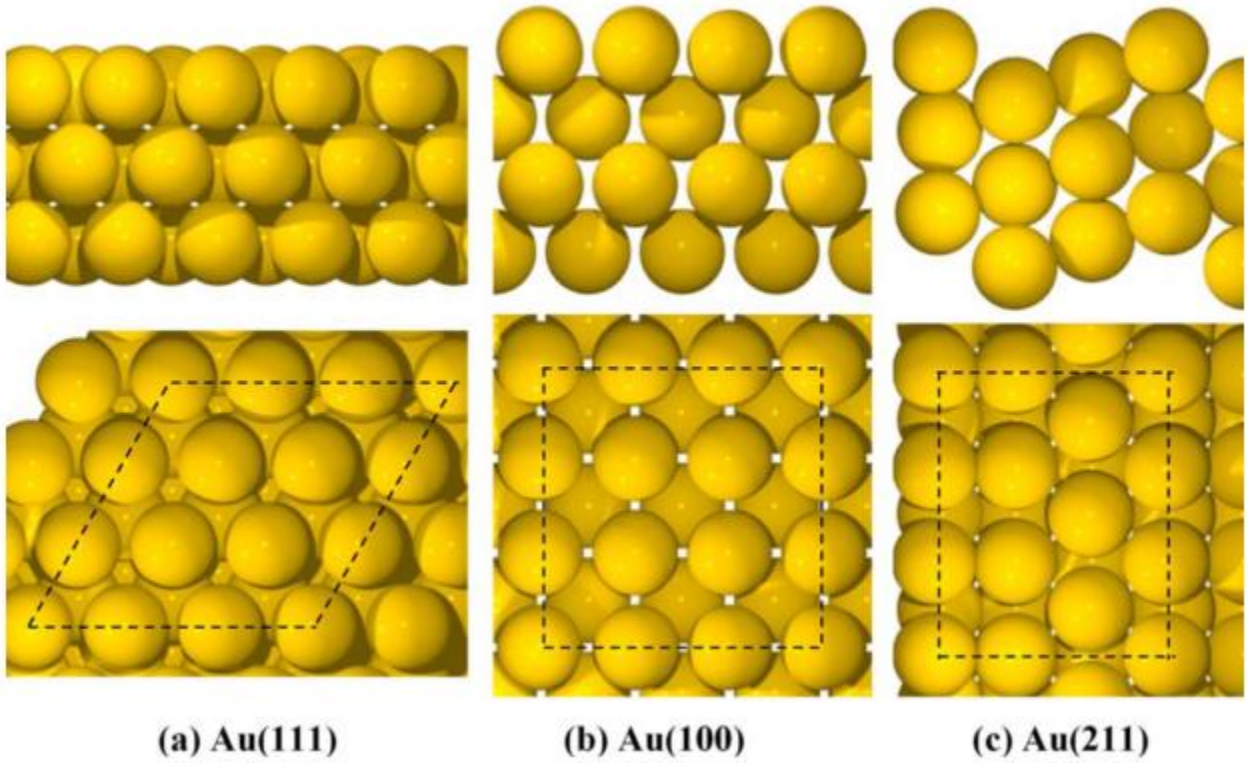

Figure 6.1. Side and top views of the three model Au surfaces used in this study: (a) Au(111), (b) Au(100), and (c) Au(211). Dotted black lines in the top view indicate the unit cell on each surface.

The binding energies (BEs) are calculated with respect to the total energy of the clean slabs (E_{slab}) and the corresponding adsorbates in the gas phase ($E_{adsorbate,\ gas\text{-}phase}$), that is, $BE_{adsorbate} = E_{total} - E_{slab} - E_{adsorbate,\ gas\text{-}phase}$. In the discussion of the DFT results, the electronic energy values mentioned include the zero-point energy (ZPE) corrections unless otherwise noted. The minimum energy pathways and activation energy barriers for

all elementary steps are determined using the climbing image nudged elastic band method.[70, 71] The minimum energy path for each elementary step is discretized with at least seven images, in addition to the initial and final states. A vibrational frequency analysis[72] is performed to confirm the true nature of the saddle point by identifying a single imaginary frequency along the reaction coordinate. The frequencies are calculated using the harmonic oscillator assumption by diagonalization of the mass-weighted Hessian matrix in internal coordinates.[72]

6.2.5 Microkinetic Modeling

The mean-field microkinetic model for FA decomposition consists of 17 elementary steps, including some steps that are in common with the WGS reaction. The initial estimates for the ZPE-corrected binding energies (BEs) and EAs are derived from DFT calculations and are later adjusted to reproduce the experimental kinetic dataset collected on the Au/SiC catalysts. The entropies of adsorbed intermediates and the pre-exponential factors are determined from the DFT-calculated vibrational frequencies following a procedure described elsewhere.[73] Lateral adsorbate–adsorbate interactions are neglected and all the BEs and EAs were assumed to be coverage independent. This assumption is reasonable as surface coverages are expected to be low under the experimental conditions. The maximum surface coverage is restricted to 1 ML and multilayer adsorption is not considered. All species are assumed to occupy exactly one site on the surface, except for the bidentate formate (HCOO), which blocks two surface sites. Given the geometry of the reactor used in our experiments, the reactor is modeled as a plug-flow reactor. Hence, our reactor model comprises five differential equations for

the gaseous flow rate along the reactor length, eight steady-state algebraic equations for the fractional surface coverages of reaction intermediates, and one site-balance equation. Further details of our model formulation can be found in previous work.[73-75]

6.3 Results and Discussion

In order to develop a comprehensive mean-field microkinetic model that would allow the study of structure sensitivity for this reaction on Au surfaces, a rigorous study was performed of the properties of five closed-shell species and eight reaction intermediates, as well as the reaction energetics of 17 elementary steps, on the Au(111), Au(100), and Au(211) facets using first principles DFT calculations. The results from DFT calculations will be presented first; followed by the results of the fits of the microkinetic model predicted rates and selectivities to the experimentally measured reaction kinetics data.

6.3.1 Structure and adsorption thermochemistry of reaction intermediates

The BEs and the preferred adsorption sites of surface species involved in this reaction network on the three Au facets studied are summarized in Table 6.1. The following description focuses primarily on the most favorable binding configurations for the adsorbates. Schematic representations for these configurations are shown in Figures 6.2–6.5. In this discussion, and throughout the text, (g) stands for "gas-phase species" and each "*" represents a single surface site occupied by the corresponding adsorbate. Wherever available, the previously reported literature values (as obtained using DFT) for

the BEs of surface species and activation energy barriers (EA) of elementary steps are reported in parenthesis next to our DFT derived numbers.

Table 6.1. Calculated PW91 Binding Energies (BEs) of Adsorbed Species and their Preferred Adsorption Sites on Au(111), Au(100), and Au(211)

	Au(111)		Au(100)		Au(211)	
Species	Adsorption Site	BE (eV)	Adsorption Site	BE (eV)	Adsorption Site	BE (eV)
H*	fcc	-1.90	bridge	-2.06	bridge	-2.11
O*	fcc	-2.41	hollow	-2.69	bridge	-2.80
OH*	bridge	-1.36	bridge	-1.96	bridge	-2.07
H_2O*	top	-0.10	top	-0.14	off-top	-0.20
CO*	top	-0.21	bridge	-0.62	bridge	-0.67
CO_2*	physisorbed	-0.02	physisorbed	-0.02	physisorbed	-0.05
HCO*	top	-1.05	top	-1.26	top	-1.38
HCOO*	top-top	-1.69	top-top	-2.02	top-top	-2.19
COOH*	top	-1.27	top	-1.48	top	-1.58
COOHcis*	top	-1.22	top	-1.48	top	-1.59
HCOOH*	top	-0.10	top	-0.16	top	-0.21

Zero of the energy scale is the slab and the gas-phase species at infinite separation from each other

Overall all the closed-shell species involved in this reaction network, with the exception of CO, are weakly bound to all three Au facets studied. They exhibit only a weak preference for their most stable binding configurations, as evidenced by the near degeneracy of their several adsorption states. Our calculations do not take include the long-range interactions, such as van der Waals forces,[76, 77] and it is important to note that these can contribute an additional stabilization of ≈ 0.1–0.2 eV per carbon atom. The absolute magnitude of the BEs of surface species on the three Au surfaces are observed to decrease in the general order: Au(211) > Au(100) > Au(111), in agreement with the general concept that adsorbates tend to exhibit stronger binding to more open facets.[78]

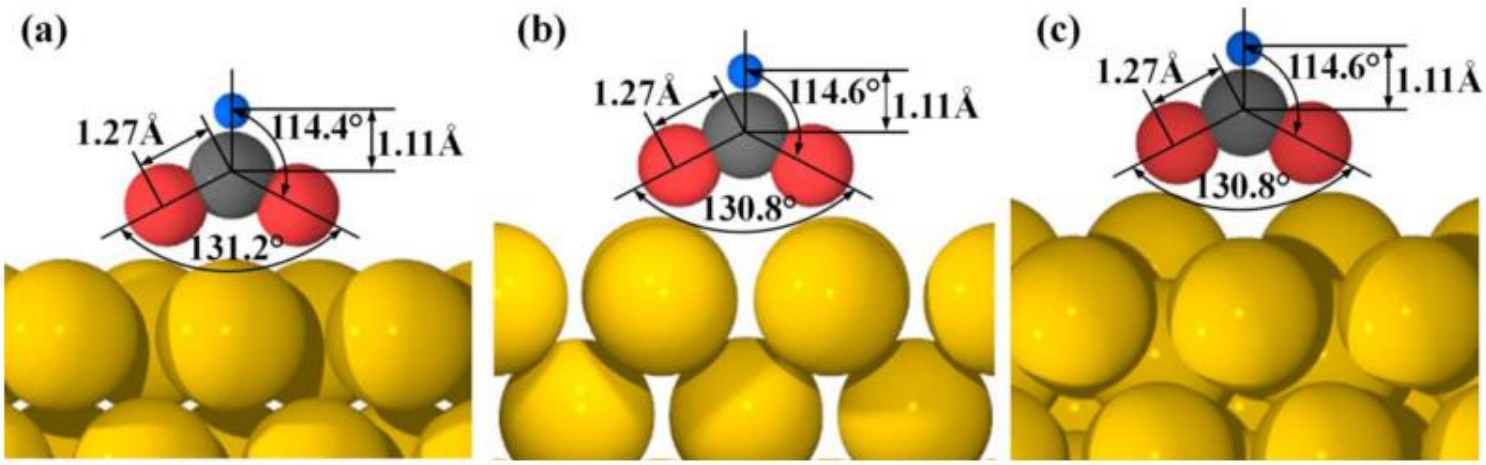

Figure 6.2. Most stable configurations of Formate (HCOO) intermediate on (a) Au(111), (b) Au(100), and (c) Au(211).

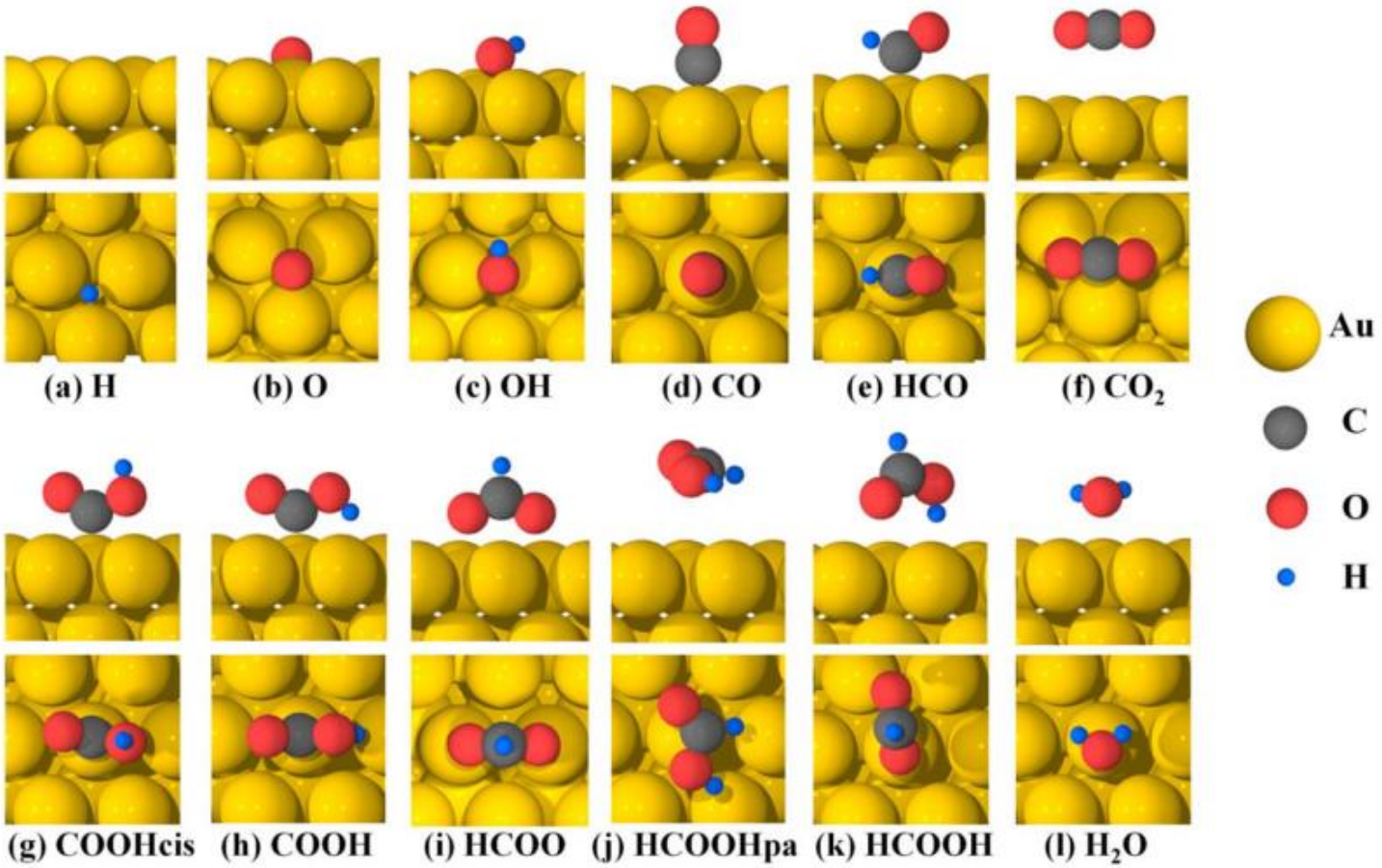

Figure 6.3. Most stable configurations of FA decomposition intermediates on Au(111) (top panel represents cross-sectional view; bottom panel represents top view).

FA exhibits two distinct stable configurations: one where all atoms of the HCOOH* molecule are in the same plane perpendicular to the surface (HCOOH*), and another one in which this plane is parallel to the surface (HCOOHpa*). The latter orientation is found to adsorb with practically zero BE on all three surfaces. HCOOH* binds to the three studied Au facets via its carbonyl O atom on a top site with the O-H and C-H bonds pointing toward and away from the surface, respectively, and has a BE of -0.10 eV (-0.15 eV[79]), -0.16 eV (-0.19 eV[80]), and -0.21 eV on Au(111), Au(100), and Au(211), respectively. Formate has for long been proposed as one of the key reaction intermediates in FA decomposition and has also been frequently cited as a possible intermediate in WGS[81-83] and methanol synthesis[84-86] reactions. As a result, it has received much scientific attention,[31, 57, 87-92] both in the experimental and theoretical literature. Our DFT calculations indicate that HCOO** binds on all three Au facets in a bidentate configuration (Figure 6.2) with its O ends on top of two nearest neighbor metal atoms. This structural data is in agreement with the available experimental (NEXAFS and IR)[87] and theoretical evidence. It has a BE of -1.69 eV (-1.82 eV[79]), -2.02 eV (-2.10 eV[80]), and -2.19 eV on Au(111), Au(100), and Au(211), respectively.

The BEs of atomic hydrogen on Au(111), Au(100), and Au(211) are -1.90 eV (-2.03 eV,[79] -2.20 eV[93, 94]), -2.06 eV (-2.29 eV[80]), and -2.11 eV (-2.32 eV[95]), respectively. H* binds preferentially on the bridge sites on Au(100) and Au(211), and on the threefold sites on Au(111). The most stable binding configuration on the Au(111) facet is at the fcc sites, although the hexagonal close packed (hcp) sites are found to be energetically quasidegenerate to the fcc sites.

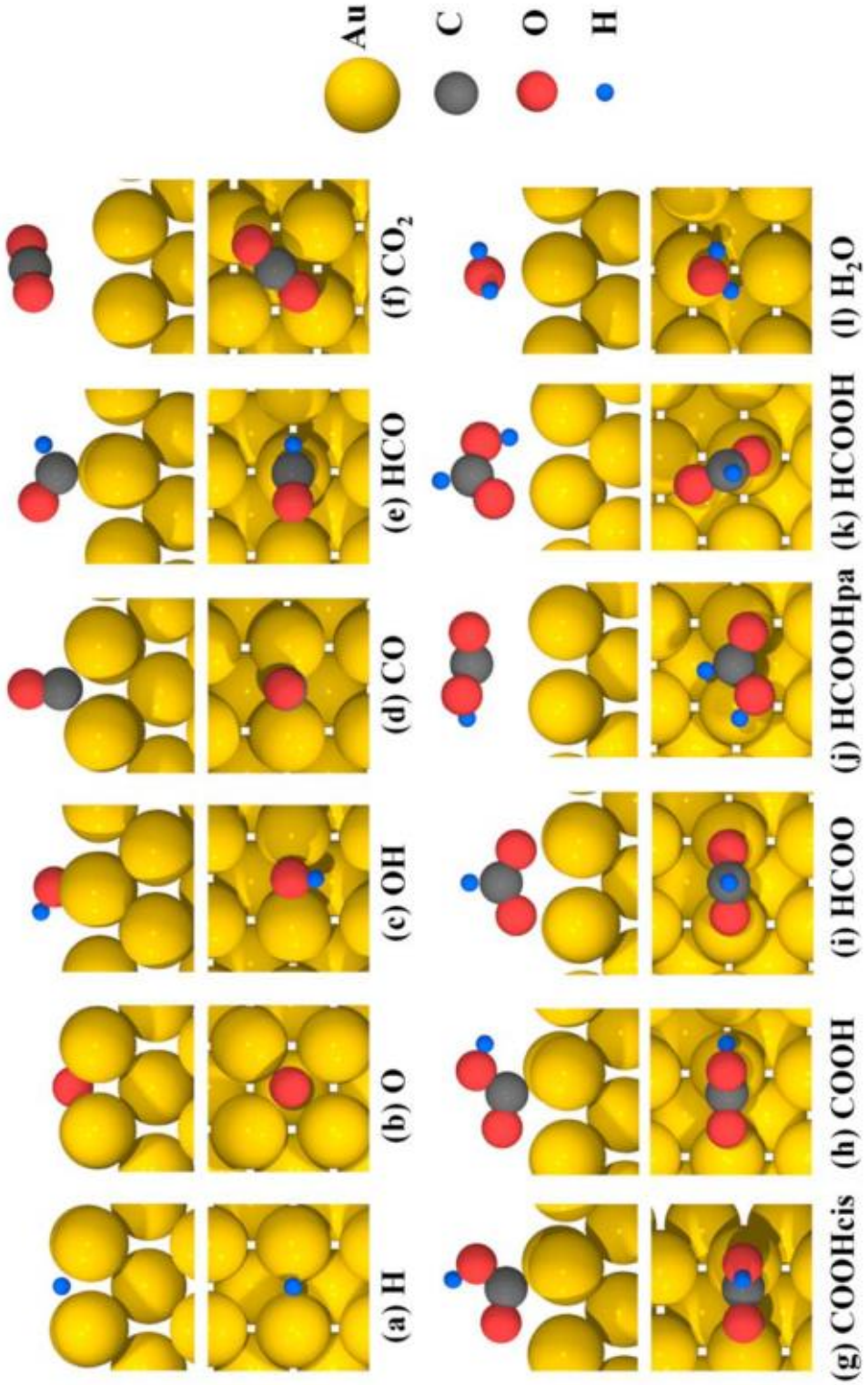

Figure 6.4. Most stable configurations of FA decomposition intermediates on Au(100) (top panel represents cross-sectional view; bottom panel represents top view).

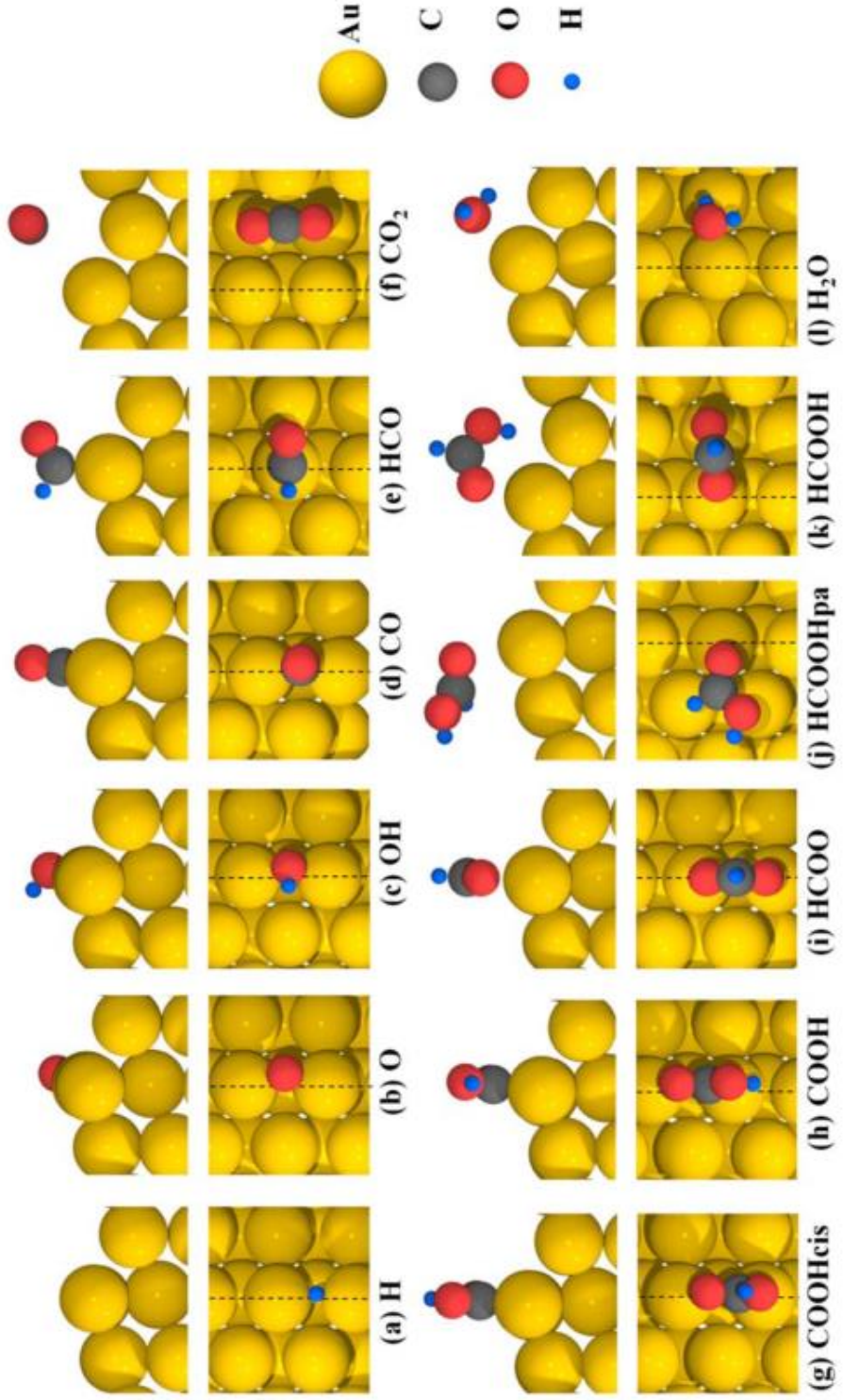

Figure 6.5. Most stable configurations of FA decomposition intermediates on Au(211) (top panel represents cross- sectional view; bottom panel represents top view; dotted black lines in the top view denote the step edge of Au(211) surface).

Atomic oxygen is most stable in the threefold fcc site on Au(111), the fourfold hollow site on Au(100), and the twofold bridge site on the step edge of Au(211), with BEs of -2.41 eV (-2.43 eV[96]), -2.69 eV(-2.85 eV[97]), and -2.80 eV(-2.83 eV[98]), respectively. Hydroxyl is most stable when adsorbed in a top-tilted configuration on the bridge sites of all three Au facets with BEs of -1.36 eV (-1.47 eV[96]), -1.96 eV, and -2.07 eV on Au(111), Au(100), and Au(211), respectively.

Carboxyl exhibits two stable adsorption configurations: (a) one with H pointing downward toward the surface, the trans isomer (COOH*) and (b) one with H pointing away from the surface, the cis isomer (COOHcis*). COOH* has a BE of -1.27 eV, -1.48 eV (-1.61 eV[80]), and -1.58 eV on Au(111), Au(100), and Au(211), respectively. The formyl radical binds preferentially through its C atom to the top sites of all three Au facets, with BEs of -1.05 eV, -1.26 eV, and -1.38 eV on Au(111), Au(100), and Au(211), respectively.

Carbon monoxide (CO) binds through the carbon atom, with the C-O bond perpendicular to the surface. It binds preferentially to the top site on Au(111), and the two fold bridge sites on Au(100) and the step-edge of Au(211), with BEs of -0.21 eV (-0.26 eV[79]), -0.62 eV (-0.62 eV[80]), and -0.67 eV (-0.65 eV[99]), respectively. Water binds weakly through its oxygen atom to the top site of the three Au facets with the plane containing all the atoms parallel to the surface. It has a BE of -0.10 eV (-0.11 eV,[79] -0.15 eV,[100] -0.12 eV[94]), -0.14 eV, and -0.20 eV (-0.19 eV[95]) on Au(111), Au(100), and Au(211), respectively.

Carbon dioxide (CO_2) binds weakly on all three Au facets, with BEs of -0.02 to -0.05 eV. CO_2 retains its gas-phase linear geometry and exhibits very weak site preference with several degenerate binding configurations

6.3.2 Reaction Barriers of Elementary Steps

The calculated EA and reaction energies (DE) for all elementary steps studied are reported in Table 6.2. All activation energy barriers and reaction energies reported in the following text are relative to the reactant and product states at infinite separation.

Table 6.2. PW91 Reaction Energies (DE) and Activation Energy Barriers (EA) for the Elementary Steps Considered in the HCOOH Decomposition Reaction Network on Au(111), Au(100), and Au(211) Surfaces

		Au(111)		Au(100)		Au(211)	
#	Reaction	ΔE(eV)	E_A(eV)	ΔE(eV)	E_A(eV)	ΔE(eV)	E_A(eV)
1	HCOOH + * ↔ HCOOH*	-0.10		-0.16		-0.21	
2	HCOOH* ↔ HCOOHpa*	0.24	0.55	0.29	0.59	0.26	0.63
3	HCOOH* + 2* ↔ HCOO** + H*	0.86	1.29	0.42	0.87	0.26	0.98
4	HCOOHpa* + * ↔ COOH* + H*	0.80	1.22	0.44	0.83	0.37	0.87
5	HCOOH* + * ↔ HCO* + OH*	2.32	2.16	1.57	1.91	1.38	1.74
6	HCOO** ↔ CO_2* + H*	-0.35	0.80	-0.17	0.84	-0.08	0.85
7	HCOO** + H* ↔ H_2 + CO_2* + 2*	-0.84	0.99	-0.34	1.11	-0.15	1.30
8	COOH* + * ↔ H* + CO_2*	-0.54	0.54	-0.48	0.68	-0.46	0.74
9	COOH* ↔ COOHcis*	0.05	0.45	0.00	0.52	-0.01	0.44
10	COOHcis* + * ↔ OH* + CO*	1.30	1.33	0.55	0.70	0.51	1.00
11	COOHcis* + H* ↔ H_2O* + CO*	-0.33	0.55	-0.36	0.68	-0.30	0.87
12	HCO* + * ↔ H* + CO*	0.07	0.59	-0.29	0.24	-0.26	0.28
13	OH* + H* ↔ H_2O*	-1.64	0.26	-0.92	0.38	-0.81	0.61
14	2H* ↔ H_2 + 2*	-0.49	0.57	-0.17	0.47	-0.07	0.49
15	CO_2* ↔ CO_2 + *	0.02		0.02		0.05	
16	H_2O* ↔ H_2O + *	0.10		0.14		0.20	
17	CO* ↔ CO + *	0.21		0.62		0.67	

All the values are relative to infinite separation in initial/final states. All adsorption and desorption steps are found to be nonactivated and are assumed to be quasiequilibrated.

6.3.2.1 HCOOH Activation.

In this section three different pathways for HCOOH activation, namely, the HCOO, the COOH, and the HCO mediated pathways (Figure 6.6) are discussed.

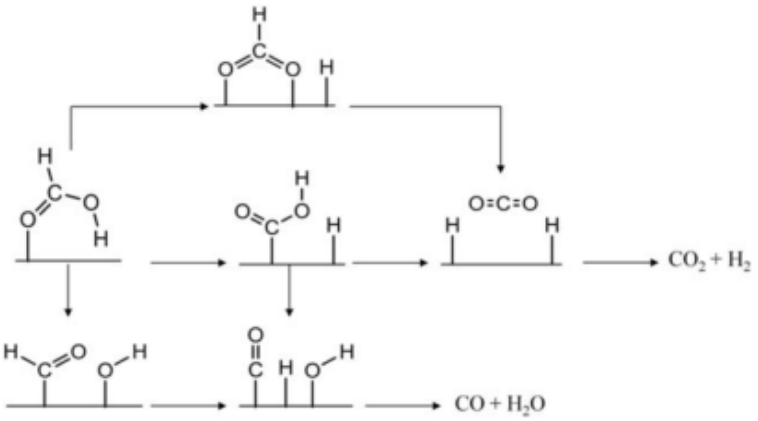

Figure 6.6. The three HCOOH decomposition pathways considered.

$$HCOOH^* + 2^* \rightarrow HCOO^{**} + H^*$$

HCOOH* decomposition to HCOO** is found to proceed directly from the most stable, albeit weakly bound perpendicular configuration. The most favorable pathway involves H abstraction from HCOOH* over the top site on Au(111), but bridge site on Au(100) and Au(211) surface. This step has a ΔE of 0.86 (0.89 eV[79]), 0.42, and 0.26 eV, with EA of 1.29 (1.36 eV[79]), 0.87, and 0.98 eV on Au(111), Au(100), and Au(211), respectively.

$$HCOOH^* \rightarrow HCOOHpa^*;\ HCOOHpa^* + * \rightarrow COOH^* + H^*$$

C-H bond scission in HCOOH*, yielding adsorbed COOH* and atomic hydrogen, is a two-step process. The first step is the rotation of HCOOH* to yield a metastable HCOOHpa* state. This rotation is quasi structure-insensitive, with a barrier of 0.55–0.63

eV on the three Au facets. HCOOHpa* is higher in energy than the most stable adsorbed state (HCOOH*), but it brings the carbonic hydrogen in FA closer to the three Au surfaces, thereby facilitating the C-H bond scission. The specific bond scission in HCOOHpa* to yield COOH* is an endothermic step, with EA of 1.22, 0.83, and 0.87 eV on Au(111), Au(100), and Au(211), respectively.

$$HCOOH^* + * \rightarrow HCO^* + OH^*$$

The dehydroxylation of HCOOH* to yield HCO* and OH* has a barrier of 2.16, 1.91, and 1.74 eV on Au(111), Au(100), and Au(211), respectively, significantly higher than the HCOO** and COOH* formation steps.

6.3.2.2 Product Formation

$$HCOO^{**} \rightarrow CO_2^* + H^*$$

H abstraction from HCOO** starts with the rotation of the HCOO** molecule such that the C-H bond becomes parallel to the Au surface, and one Au-O bond is broken just before the C-H bond scission over the top sites of all three Au facets (top site at the step edge for Au(211) facet). The H-C bond length in the transition state is 1.29, 1.37, and 1.18 Å on Au(111), Au(100), and Au(211), respectively (Figure 6.7), as compared to the bond length of 1.11 Å in adsorbed HCOO**. This step is slightly exothermic on Au(111) (ΔE = -0.35 eV) and Au(100) (ΔE = -0.17 eV) and near-thermo neutral on Au(211) (ΔE = -0.08 eV). EA for this step is relatively invariant of the model surface, with values of 0.80 (0.65 eV[101]), 0.84, and 0.85 eV on Au(111), Au(100), and Au(211), respectively.

$$COOH^* + * \rightarrow CO_2^* + H^*$$

Carboxyl decomposition to CO_2 is found to proceed directly from the more stable trans configuration (COOH*). The reaction on all three facets starts with rotation of carboxyl within its molecular plane, such that O-H bond scission takes place over the top site. Atomic hydrogen subsequently diffuses to the closest preferable site, and CO_2 settles in its physisorbed state. This step is exothermic, with ΔE of -0.54 (-0.49 eV[94]), -0.48, and -0.46 eV, and has EA of 0.54 (0.58 eV[94]), 0.68 eV, and 0.74 eV on Au(111), Au(100), and Au(211), respectively.

$$COOH^* \rightarrow COOHcis^*; COOHcis^* + * \rightarrow CO^* + OH^*$$

Different from the previous step, CO formation from carboxyl starts from the cis configuration of carboxyl. For this to take place, the most stable trans configuration of COOH* undergoes activated rotation (with E_A of 0.45, 0.52 and 0.44 eV on Au(111), Au(100), and Au(211), respectively), to yield the cis configuration (COOHcis*). The dissociation of COOHcis* takes place over the top site on all three Au facets, with EA of 1.33 (1.25 eV[94]), 0.70, and 1.00 eV on Au(111), Au(100), and Au(211), respectively.

$$H^* + H^* \rightarrow H_2 + 2^*$$

H_2 recombinative desorption starts with two H* adsorbed on adjacent bridge sites, and the H-H bond formation takes place over the top site, for all three Au facets. The H-H bond lengths at the transition state are 1.38, 1.38, and 1.34 Å on Au(111), Au(100), and Au(211), respectively, (Figure 6.7) as compared to an H_2 gas-phase bond length of 0.75 Å.

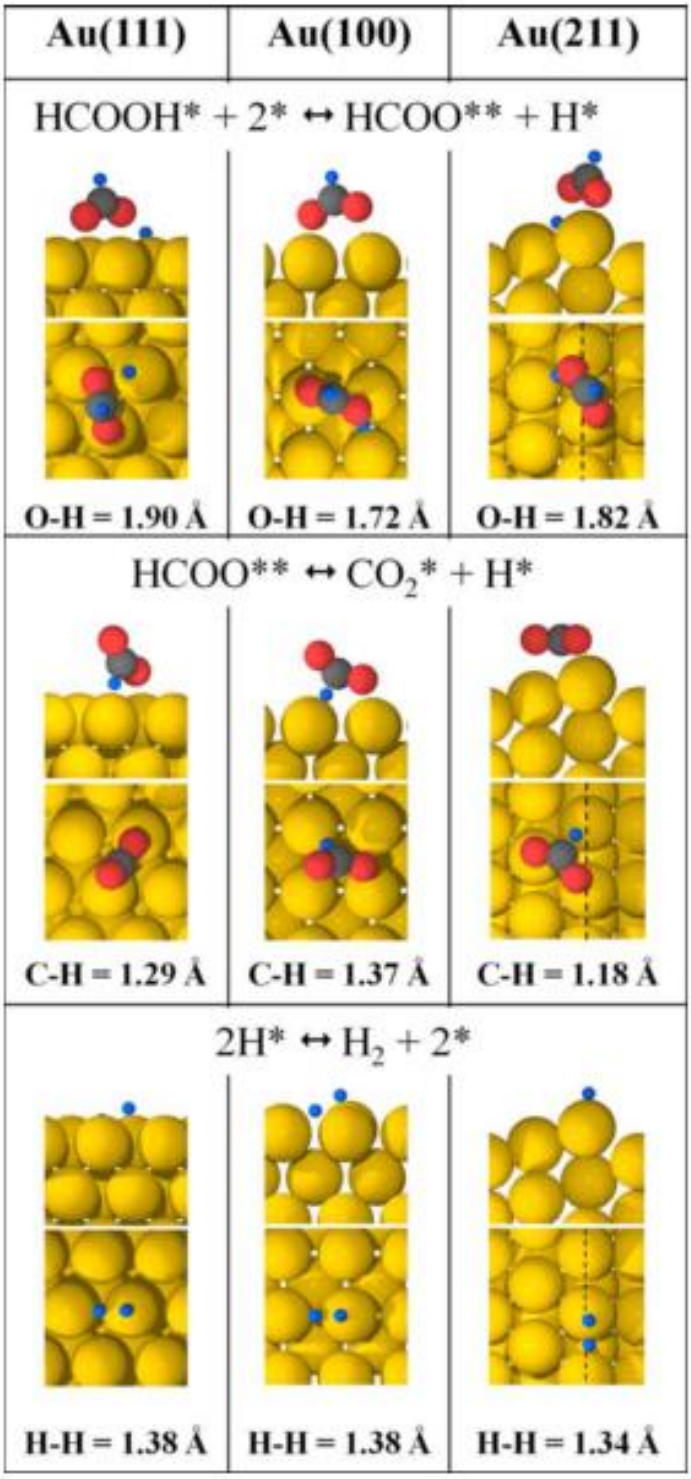

Figure 6.7. Side and top views of the transition states (TS) for the three kinetically relevant steps (as predicted by our microkinetic modeling results) on Au(111), Au(100), and Au(211) surfaces. The lengths of the bond being broken/formed are reported for each transition state. Dotted black lines in the top views of Au(211) surface indicate the step-edge.

6.3.3 Potential Energy Surfaces

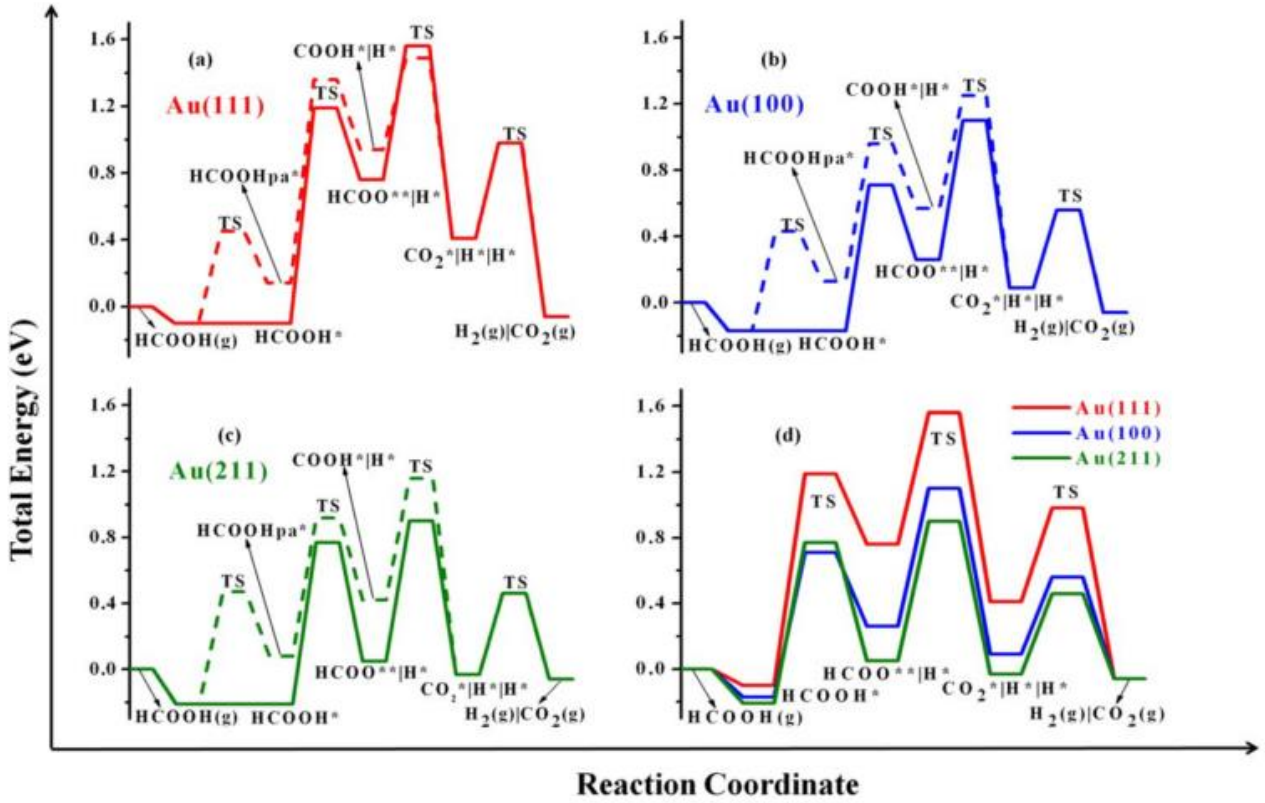

Figure 6.8. The two-dimensional PESs of FA decomposition reaction via the HCOO (solid lines) and COOH (dashed lines) mediated pathways on Au(111) (red) (a), Au(100) (blue) (b), and Au(211) (green) (c), and a comparison of the most favorable pathways (HCOO mediated) on all three facets (d). Energy zero corresponds to the energy of HCOOH in the gas phase, away from the slab. A "|" between two adsorbates denotes that they are at infinite separation from each other.

The thermochemistry and activation energy barriers of the various elementary described in the previous sections can be summarized in the form of two-dimensional potential energy surfaces (PESs) for the three Au facets, as shown in Figure 6.8. The PESs shown in Figure 6.8a–c compare the HCOO** and COOH* mediated pathways on the three Au facets respectively. On the basis of the DFT-derived energetics alone, the HCOO** mediated route appears to be the minimum energy path for FA decomposition on Au(100) and Au(211), whereas both HCOO** and COOH* mediated routes appear to

be competitive for the Au(111) facet. Figure 6.8d compares the HCOO** pathway on all three Au facets, and one can suggest from here that Au(100) and Au(211) are expected to be significantly more active than the Au(111) facet.

6.3.4 Microkinetic Modeling

A microkinetic model was developed using the results from the presented DFT calculations as initial guesses for the model parameters. With no adjustments to the DFT derived parameters, the microkinetic model predicts FA decomposition rates that are 11 and 5 orders of magnitude lower on the Au(111) and Au(100)/Au(211) surfaces, respectively, than the measured experimental rates on Au/SiC. The reaction is predicted to take place via the HCOO mediated route, that is, HCOOH (g) → HCOOH* → HCOO** + H* → CO_2* + 2H* → CO_2 (g) + H_2 (g), on all three studied facets, with 100% selectivity toward the dehydrogenation products; the rate of CO production is in all cases predicted to be negligible. Following this we carried out studies in which the kinetic parameters were adjusted from the initial values on these three Au facets in an attempt to best describe the results from reaction kinetic measurements (Table 6.3). The adjustable parameters that are modified during this process are the BEs of all surface species and transition state energies of all activated elementary steps. While this procedure would give a total of 26 parameters for our complex reaction network, sensitivity analysis shows that only the BEs of HCOO**, H*, and the transition state energies of the HCOO** formation and direct decomposition steps (Steps (3) and (6) in Table 6.2) were sensitive parameters. Systematic adjustments in these parameters were made until reasonable agreement between the experimentally measured and model

predicted reaction rates was reached, and subsequently a gradient-based optimization algorithm in Matlab was used to obtain optimized values and confidence intervals for our adjustable parameters. The model predicted reaction orders and apparent activation energy barriers corresponding to the best-fitted solution are reported in Table 6.4, and as observed are in close agreement with their experimental counterparts. In addition, the experimentally observed apparent activation energy barrier (59.6 kJ mol^{-1}) in the zero-order kinetic regime is in good agreement with past experimental studies on numerous supported Au catalysts.[57, 58, 102] Figure 6.9 shows the PES for the best-fitted solution, compared with the DFT derived PESs for the three Au facets. Here, we only report the energetics of the closed catalytic cycle that is found to carry the entire reaction flux; the energetics of other elementary steps, which do not carry much flux from reactants to products are not included in the figure. We can see from this figure that the adjustments needed in the DFT derived initial guesses to obtain good fits are too large to be attributed to the computational errors in our calculations, which are typically on the order of 0.1–0.2 eV. With > 0.95 ML of the surface predicted to be vacant under all conditions, we can also rule out any potential stabilization that might result from lateral adsorbate–adsorbate interactions.[103] In particular, an additional stabilization of the transition states for the HCOO** formation and decomposition steps by more than 0.5 eV is required to obtain good fits with the experimental data, strongly suggesting that (1) the Au(111), Au(100), and Au(211) are likely not the most accurate representation of the active sites for this reaction and (2) the active site might be an even more under-coordinated environment that would stabilize the transition states to a much greater extent than these three facets. This conclusion is a quantitative confirmation of a previous proposal put forward by

Iglesia and Ojeda based on their experimental reactivity studies for the same reaction.[57] Importantly, similar suggestions for the reactivity of single metal atoms or very small metal nanoclusters have been made in the literature for other reactions as well.[104-107]

Table 6.3. Reaction Rates and Selectivities Obtained from the Kinetics Experiments on Au/SiC

	Temperature (K)	y(HCOOH)	y(He)	$y(H_2)$	$y(CO_2)$	Experimental Rates (μmol $gcat^{-1}$ min^{-1})	Experimental Selectivity ($CO_2/(CO_2+CO)$)
1	373	0.01	0.99	0.00	0.00	9.30	1.00
2	373	0.02	0.98	0.00	0.00	15.42	1.00
3	373	0.02	0.98	0.00	0.00	18.65	1.00
4	373	0.04	0.96	0.00	0.00	33.00	1.00
5	343	0.03	0.97	0.00	0.00	5.05	1.00
6	353	0.03	0.97	0.00	0.00	8.00	1.00
7	363	0.03	0.97	0.00	0.00	15.72	1.00
8	368	0.03	0.97	0.00	0.00	21.35	1.00
9	373	0.03	0.97	0.00	0.00	24.11	1.00
10	378	0.03	0.97	0.00	0.00	32.55	1.00
11	383	0.03	0.97	0.00	0.00	41.30	1.00
12	373	0.03	0.96	0.01	0.00	23.91	1.00
13	373	0.03	0.94	0.04	0.00	24.09	1.00
14	373	0.03	0.92	0.06	0.00	24.32	1.00
15	373	0.03	0.96	0.00	0.01	23.69	1.00
16	373	0.03	0.95	0.00	0.03	23.76	1.00
17	373	0.03	0.92	0.00	0.06	23.97	1.00

y denotes mole fraction in the inlet feed. The catalyst sample used in these studies was reduced *in situ*, prior to the reaction, at 623 K under pure hydrogen flow (30 cm^3 STP min^{-1}) for 4 h. All the reaction rates reported here correspond to the steady-state values. The reaction was allowed to run for at least an hour after changing the conditions and before taking any measurements, and the steady state was confirmed by taking several readings over the next hour; hence, each data point is an average of several experimental runs.

Table 6.4. Experimental and Model Predicted Reaction Orders and Apparent Activation Energy Barriers

	Experiment	Model
HCOOH	0.95 ± 0.06	0.99
CO_2	0.01 ± 0.003	0.00
H_2	0.01 ± 0.003	0.00
E_A	59.6 ± 1.6 kJ mol^{-1}	60.2 kJ mol^{-1}

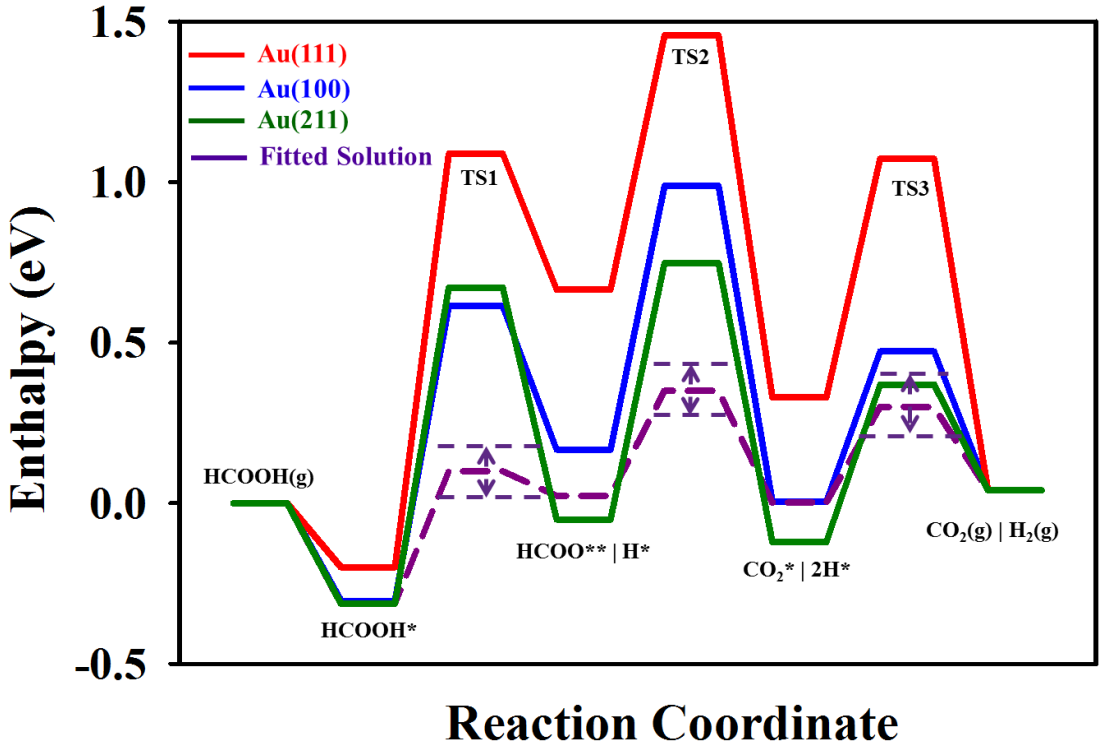

Figure 6.9. Enthalpy surfaces for FA decomposition via the HCOO** mediated pathway on Au(111), Au(100), and Au(211) facets (red, blue, green, respectively) as obtained directly from DFT calculations, and that corresponding to the best fitted solution (violet) along with the confidence intervals for the transition states. TS denotes the transition state for the respective elementary step. This sequence of elementary steps car- ries almost the entire flux from reactants to products for all experimental conditions studied.

6.3.4.1 Rate Determining Step

The individual reaction fluxes of the elementary steps have revealed that the overall reaction proceeds entirely through the "direct HCOO**" route, and no reaction flux is observed through any of the COOH* mediated pathways. The reaction mechanism and the rate determining steps in the reaction scheme were further analyzed using Campbell's degree of rate control,[108-110] which quantifies the kinetic importance of an elementary step in a reaction scheme by computing the relative change in the overall reaction rate upon changing the forward and reverse rate constants for that step, while holding the equilibrium constant for that step as well as the rate constants for all other

steps constant. In this formalism, the degree of rate control (X_{RC}) of each elementary step can be evaluated using the following relation

$$X_{RC,i} = \frac{k_i}{r}\left(\frac{\delta r}{\delta k_i}\right)_{K_{i,eq}k_j}$$

where k_i is the rate constant for step i, $K_{i,eq}$ is the equilibrium constant for this step, and r is the overall reaction rate. For all equilibrated steps (including the adsorption/desorption steps that were assumed to be quasiequilibrated), $X_{RC,i}$ is 0. Table 6.5 gives the $X_{RC,i}$ for the kinetically relevant steps in our reaction mechanism. For the "best-fitted solution," Step 6 exhibits the highest degree of rate control for all reaction conditions and, hence, is the most rate controlling.

Table 6.5. Campbell's Degree of Rate Control for Kinetically Relevant Steps

Step #	Elementary Step	X_{RC}
3	HCOOH* + 2* ↔ HCOO** + H*	0.25
6	HCOO** ↔ CO_2* + H*	0.64
14	2H* ↔ H_2 + 2*	0.10

These numbers are reported for the reaction condition # 9 of Table 6.3

6.3.5 Active Sites

The results from our microkinetic model all suggest that Au(111), Au(100), and Au(211) are, in all likelihood, not the best representation of active sites for this reaction on SiC-supported Au catalysts. In view of this, the major contributors to the overall rates could potentially be the Au atoms with lower (< 7) Au–Au coordination that can therefore exhibit even greater stabilization of reaction intermediates and transition states

than the more open facets studied here [(100) and (211)]. To gain further insights into the nature of the active sites, a series of catalysts made to possess varying degrees of Au dispersion were synthesized by treating the initial catalyst in flowing H_2 at different reduction temperatures (623, 673, 723, 973, and 1073 K) for 8 h, prior to using these materials as catalysts for reaction kinetic studies. Typically, the catalysts that are prereduced at low temperatures are more highly dispersed (and less sintered) than the materials that are prereduced at high temperatures.

6.3.5.1 Particle Size Distributions

Figure 6.10 shows STEM images that represent the particles typically observed in each of the five catalysts. Sets of images for each catalyst were used to determine the Au particle size distribution (Figure 6.11) in the samples. This technique allows for imaging Au nanoparticles as low as 0.3 nm in size. It was observed that reducing the catalysts under a H_2 stream at increasingly elevated temperatures resulted in increased averaged Au particle sizes, as reported in Table 6.6.

Table 6.6. Average Particle Size (as Determined by STEM) and Experimentally Measured Reaction Rates on the Five Different Au/SiC Catalysts

Catalyst Sample #	Prereduction Temperature (K)	Number of Total/Subnanometer sized Au Clusters Analyzed	Number Average Particle Size (d [nm])	Experimental Observed Reaction Rate (μmol $gcat^{-1}$ min^{-1})
1	623	6860/1248	2.55	178.58
2	673	4837/636	3.09	129.93
3	723	3887/213	3.23	97.84
4	973	1119/0	7.53	9.02
5	1073	1153/0	10.74	2.64

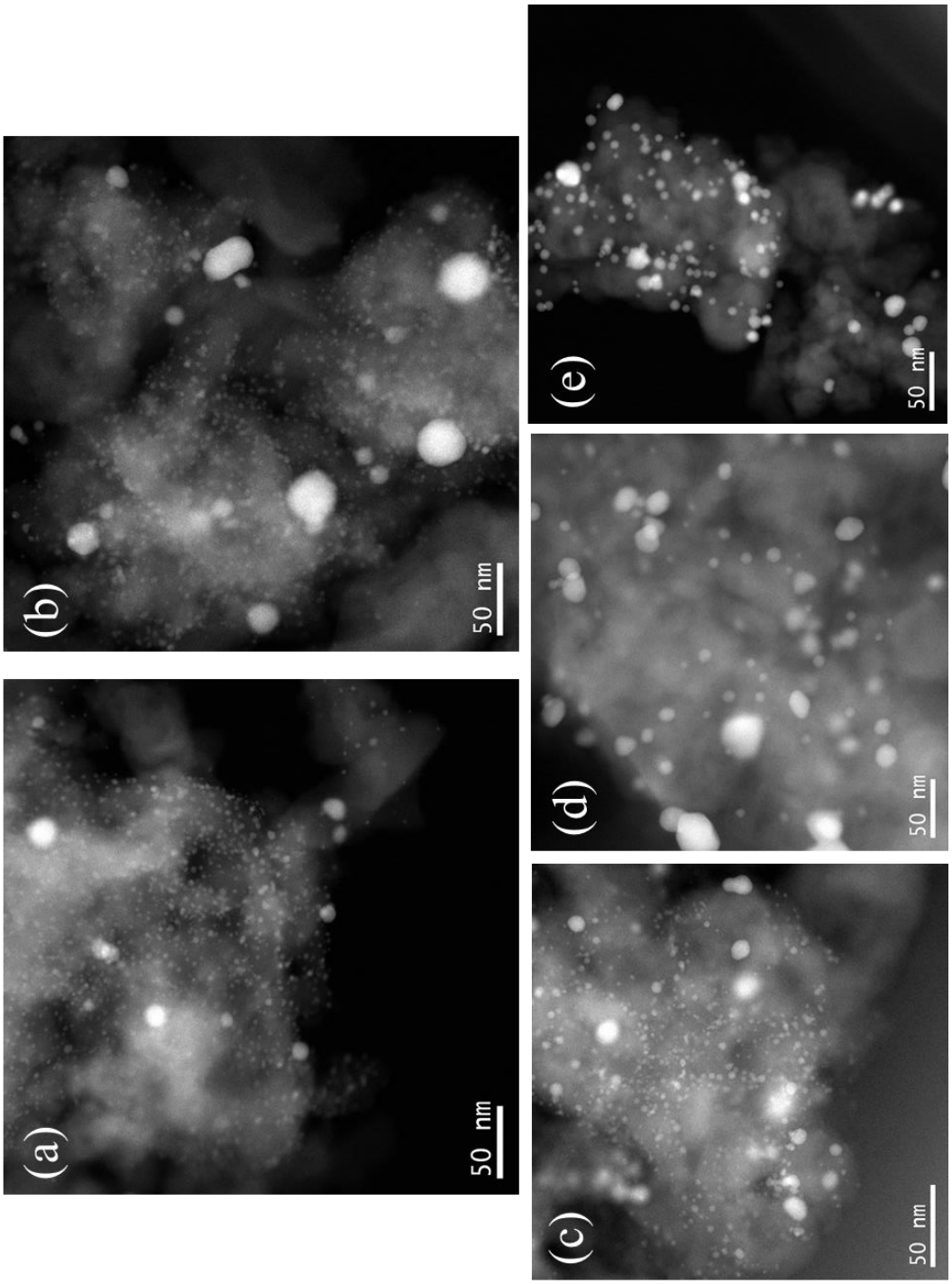

Figure 6.10. Typical STEM images of Au/SiC catalysts used to determine the Au particle-size distributions.

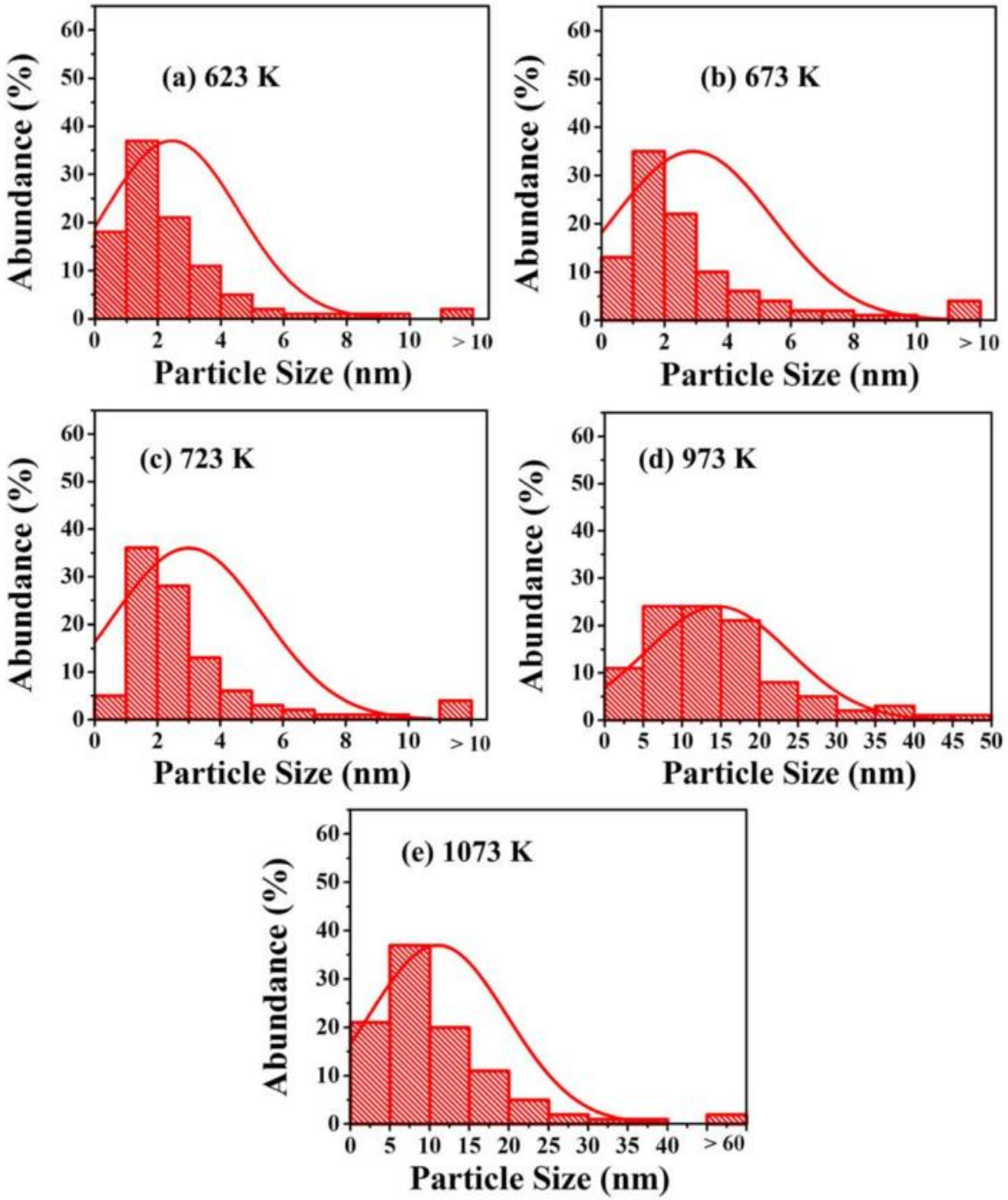

Figure 6.11. Histograms depicting the Au particle-/cluster-size distributions for the Au/SiC catalysts prereduced at 623–1073 K for 8 h.

6.3.5.2 Kinetic Reaction Rate Measurements

Reaction kinetic measurements were performed to obtain the FA decomposition rates on five catalysts under the same operating conditions (T = 413 K, Total inlet flow rate = 100 mL min^{-1}, Inlet feed composition = 2.5% FA and 97.5% He). A monotonic decrease in the reaction rates with an increase in the prereduction temperature (and the average particle size) was observed, as shown in Table 6.6.

Importantly, it was observed that the number (and relative abundance) of subnanometer sized Au clusters decreases sharply upon increasing the calcination temperature. As a result, these reactivity trends provide a first indication that the number of subnanometer sized Au clusters in the catalyst may be correlated with the overall reaction rate. This hypothesis is consistent with past experimental studies[56, 57, 102] that have postulated that this remarkable activity on supported Au catalysts arises from subnanometric Au clusters that are undetected in TEM micrographs. To quantify the contributions of different Au atoms in the catalytic particles/clusters to the overall reaction rate, we first classify the different kinds of Au atoms that are present in any given cluster into four categories: (1) Corner (C) atoms: CN = 1–4, (2) Perimeter (P) atoms: CN = 5 and 6, (3) Terrace (T) atoms: CN = 7–9, and (4) Bulk (B) atoms: CN $\geq$ 9, where CN refers to the Au–Au coordination number. The surface (S) atoms are defined as the sum total of the C, P, and T atoms.

In their work on the WGS reaction on supported Au catalysts, Ribeiro and coworkers[111-113] used physical models of Au clusters as truncated cuboctahedra to develop relations used to determine the variation of the C, P, and T sites with the number averaged Au particle size. However, these relations hold true only for particles with

diameter (d) > ≈ 1.6 nm. Therefore, and given our STEM data, we attempted to develop physical models of Au clusters with d < 1.6 nm to obtain the corresponding relations that provide the dependence of the C, P, and T sites on the average Au particle size. For that purpose, we used the results of past computational studies, which used DFT to identify the most stable configurations of Au_n clusters (with 2 < n < 20) in the gas phase,[114-117] along with our physical models. The relative abundance of the C, P, and T sites is highly dependent on the choice of the cluster shape for d < 1.6 nm. As there is no general agreement in the literature on the most stable structures for these small clusters, a computational methodology must be adopted to this end. This approach would involve modeling a SiC support, performing ab initio molecular dynamics[118-120] simulations to determine the most stable configurations of different sized Au clusters on this support under reaction conditions, and finally counting the number of C, P, and T sites in these configurations to develop the structure-site density relations for quantifying the contributions from each of these sites toward the overall rates. However, as a first approximation, we treat these sites together as the total number/fraction of surface (S) atoms (i.e., C + P + T) is invariant of the actual distribution. In particular, all atoms in clusters of d < 1.6 nm can be assumed to be surface atoms (100% dispersion) without loss of accuracy.

The total moles of surface Au in the catalysts can then be calculated using the following relation

$$\text{Total moles of surface Au} = \left(\frac{\sum_n f(d)t(d)}{\sum_n t(d)}\right) * \text{Total moles of Au in the catalyst}$$

where, f(d) is the fraction of surface atoms in the cluster of diameter d (Table 6.7), t(d) is the total number of atoms in that cluster, and the summation is performed over all the Au

clusters that were identified from the STEM image of that catalyst, that is, the full particle-size distribution was used for each sample. The TOFs normalized to the surface Au moles and total Au moles are plotted against the average particle size in Figure 6.12, and these plots can be used to draw the following key conclusions:

1. A decreasing trend in the rate per surface site with average Au particle size (Figure 6.12a) indicates the heterogeneity of the surface Au sites, that is, all surface sites do not contribute equally to the overall reaction rate.
2. Figure 6.12b shows that the rate per total mole of Au catalysts varies as $d^{-2.95}$, whereas Table 6.7 suggests that the fraction of terrace, perimeter, and corner sites vary as $d^{-0.7}$,$d^{-1.8}$, and $d^{-2.9}$, respectively. Thus, the variation in FA decomposition rate per total mole of Au seems to correlate with the "corner model," that is, the rate per corner site is independent of the Au particle size, thereby implying that corner sites might be the dominant active sites for this reaction. As mentioned earlier, this conclusion is based on the assumption that the $d^{-2.9}$ dependence of the corner sites will be valid over the entire particle size range, and further studies to confirm this for smaller clusters (d < 1.6 nm) will be needed.

Table 6.7. Relations Used to Determine the Fraction of Different Sites from the Number-Average Particle Size Obtained From the STEM Images

Type of Surface Site → / Particle Size ↓	Terrace (T)	Perimeter (P)	Corner (C)	Surface (S)
< 1.6 nm	#	#	#	1.0
≥ 1.6 nm	$0.90\ d^{-0.7}$	$0.46\ d^{-1.8}$	$0.54\ d^{-2.9}$	$0.90\ d^{-0.7} + 0.46\ d^{-1.8} + 0.54\ d^{-2.9}$

The actual relations for C, P, and T sites for d < 1.6 nm are currently unavailable. All the relations presented here give the ratio of that particular site to the total Au atoms in the catalyst. For instance, for d > 1.6 nm, (Number of terrace atoms/Total Au atoms) = $0.90\ d^{-0.7}$ and so forth.

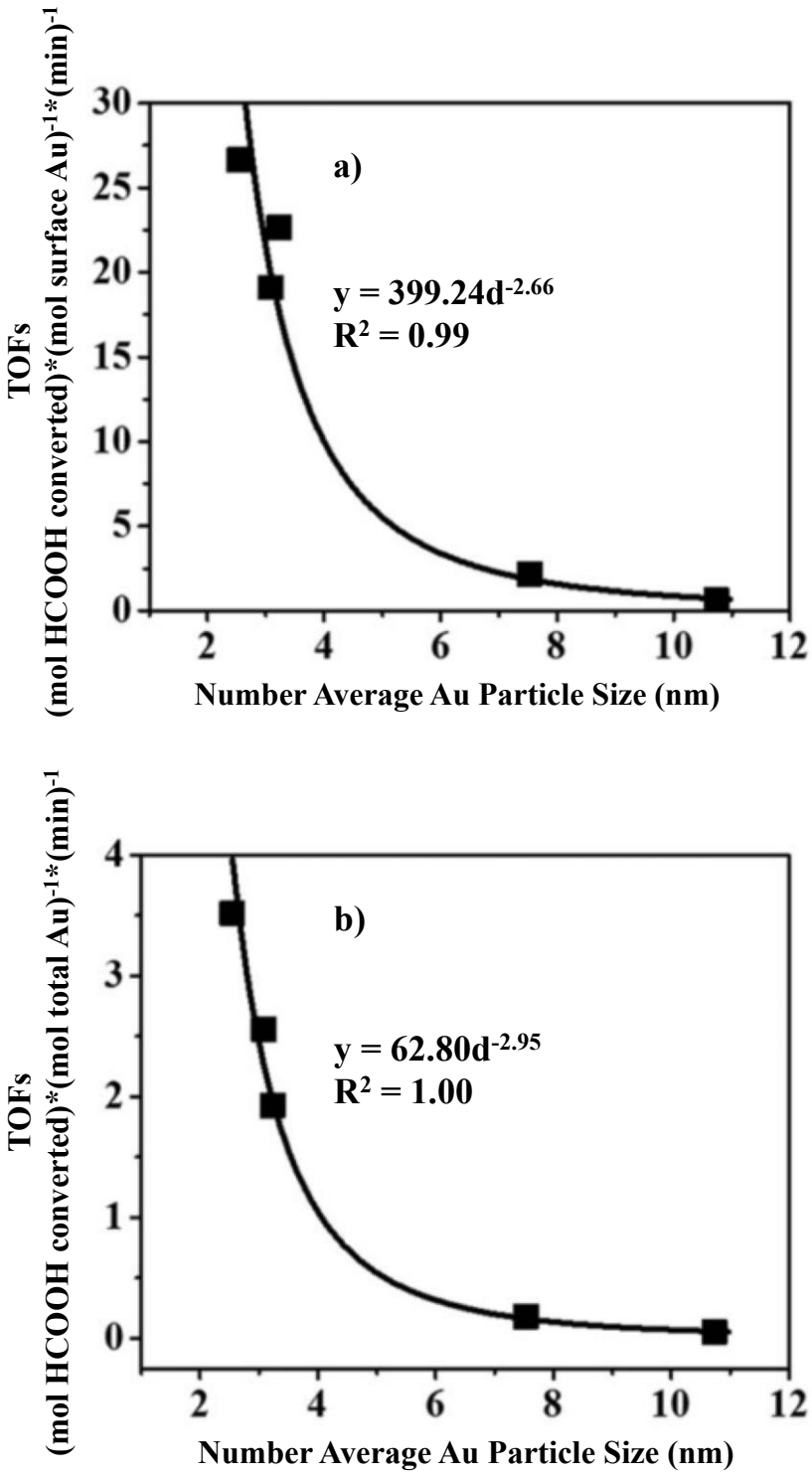

Figure 6.12. FA decomposition rate normalized by (a) surface Au moles and (b) total Au moles (2% FA inlet feed at 413 K, 1 atm) on Au/ SiC catalysts.

6.4 Conclusions

Periodic, self-consistent DFT calculations were performed to determine the energetics of 13 adsorbed intermediates for FA decomposition, as well as the activation energy barriers and pre-exponential factors of 13 activated elementary steps on Au(111), Au(100), and Au(211) surfaces, which were chosen as the representative stable model facets of Au nanoparticles on SiC support. The DFT results suggest that the surface species and transition states are stabilized as the Au–Au coordination of surface atoms decreases, and the reaction rates follow the order: Au(211) > Au(100) > Au(111).

A mean-field microkinetic model was used to describe the experimental rate and selectivity data that were collected under realistic conditions on Au/SiC. Our "best fitted solution" from the microkinetic model shows a good description of the experimental data (R^2 = 0.98), and good agreement between the model predicted apparent activation energy barriers and reaction orders with their experimental counterparts. The reaction is predicted to proceed via the formate mediated route. Importantly, the closed catalytic cycle that adequately describes the FA decomposition mechanism on Au catalysts is found to be comprised of three elementary steps: HCOOH* → HCOO** + H*, HCOO** → CO_2* + H*, and 2H* → H_2(g).

A comparison of the DFT derived BEs and EAs with the parameters obtained upon fitting the microkinetic model to the experimental data suggests that Au(111), Au(100), and Au(211) might not provide the most accurate representation of the active site on supported Au catalysts. Further reaction rate experiments and measurements of the Au particle-size distribution using STEM corroborated this claim that the coordinatively unsaturated corner sites, with Au–Au coordination of ≤ 4, are most likely

the dominant active sites for this reaction. Further DFT studies on Au clusters that possess atoms with Au–Au coordination number ≤ 4 will be needed to identify the exact nature of active site for FA decomposition on supported Au nanoparticles.

In applying this computational-experimental approach to the study of Au catalysts fundamental knowledge on the nature of the active site has been uncovered. This is especially important to the field of Au catalysis where standard chemisorption techniques to characterize metallic sites are not generally applicable and characterization methods are lagging compared to other metals such as Pt or Pd. Interestingly, The results parallel those in Chapter 5, where Pt was used, in as much as they serve as a guide for rational catalyst design and improved catalyst synthesis. It is important to state that this multi-pronged approach was crucial to arrive at the conclusions presented above and the individual contributions from each characterization technique were indispensable pieces in evaluating the role of the different Au sites (i.e. atoms with different coordination) for this catalytic reaction. Specific to the activity of the metallic Au it is now clear that a highly active catalyst for formic acid decomposition should attempt to maximize the amount of undercoordinated Au sites. That is, an efficient synthesis protocol for a Au catalyst will yield supported Au clusters but not larger nanoparticles.

6.5 Acknowledgments

The research work presented in this chapter was previously published in 2014, and is adapted here with permission from the AIChE Journal.[121]

6.6 References

1. J. J. Bozell and G. R. Petersen, *Green Chemistry*, 2010, **12**, 539-554.
2. A. Boddien, B. Loges, H. Junge, F. Gartner, J. R. Noyes and M. Beller, *Adv. Synth. Catal.*, 2009, **351**, 2517-2520.
3. C. Fellay, N. Yan, P. J. Dyson and G. Laurenczy, *Chem. Eur. J.*, 2009, **15**, 3752-3760.
4. C. Fellay, P. J. Dyson and G. Laurenczy, *Angew. Chem. Int. Ed.*, 2008, **47**, 3966-3968.
5. W. Gan, P. J. Dyson and G. Laurenczy, *React. Kinet. Catal. Lett.*, 2009, **98**, 205-213.
6. S. Fukuzumi, *Eur. J. Inorg.Chem.*, 2008, 1351-1362.
7. A. Boddien, F. Gartner, R. Jackstell, H. Junge, A. Spannenberg, W. Baumann, R. Ludwig and M. Beller, *Angew. Chem. Int. Ed.*, 2010, **49**, 8993-8996.
8. T. C. Johnson, D. J. Morris and M. Wills, *Chemical Society Reviews*, 2010, **39**, 81-88.
9. T. Y. Zhang and C. E. Wyman, *Abstracts of Papers of the American Chemical Society*, 2011, **241**, 1.
10. B. Girisuta, L. P. B. M. Janssen and H. J. Heeres, *Ind. Eng. Chem. Res.*, 2007, **46**, 1696-1708.
11. J. Bond, D. Alonso, D. Wang, R. West and J. Dumesic, *Science*, 2010, **327**, 1110-1114.
12. D. J. Braden, C. A. Henao, J. Heltzel, C. T. Maravelias and J. A. Dumesic, *Green Chemistry*, 2011, **13**, 1755-1765.
13. J. Serrano-Ruiz, D. Braden, R. West and J. Dumesic, *App. Catal., B*, 2010, **100**, 184-189.
14. M. R. Columbia and P. A. Thiel, *Journal of Electroanalytical Chemistry*, 1994, **369**, 1-14.
15. R. J. Madix, J. L. Gland, G. E. Mitchel and B. A. Sexton, *Surface Science*, 1983, 481-489.
16. R. J. Madix, *Abstracts of Papers of the American Chemical Society*, 1980, **180**, 26-PHYS.
17. Y.-K. Sun and W. H. Weinberg, *J. Chem. Phys.*, 1991, **94**, 4587-4599.
18. S. W. Jorgensen and R. J. Madix, *Journal of the American Chemical Society*, 1988, **110**, 397-400.
19. D. A. Bulushev, S. Beloshapkin and J. R. H. Ross, *Catalysis Today*, 2010, **154**, 7-12.
20. F. Solymosi, A. Koos, N. Liliom and I. Ugrai, *Journal of Catalysis*, 2011, **279**, 213-219.
21. D. H. S. Ying and R. J. Madix, *Journal of Catalysis*, 1980, **61**, 48-56.
22. A. Boddien, D. Mellmann, F. Gartner, R. Jackstell, H. Junge, P. J. Dyson, G. Laurenczy, R. Ludwig and M. Beller, *Science*, 2011, **333**, 1733-1736.
23. A. Koos and F. Solymosi, *Catalysis Letters*, 2010, **138**, 23-27.
24. D. W. Flaherty, S. P. Berglund and C. B. Mullins, *Journal of Catalysis*, 2010, **269**, 33-43.
25. J. McCarty and R. J. Madix, *Journal of Catalysis*, 1975, **38**, 402-417.

26. J. Kubota, A. Bandara, A. Wada, K. Domen and C. Hirose, *Surface Science*, 1996, **368**, 361-365.
27. P. A. Dilara and J. M. Vohs, *J. Phys. Chem.*, 1993, **97**, 12919-12923.
28. R. Larsson, M. H. Jamroz and M. A. Borowiak, *Journal of Molecular Catalysis a-Chemical*, 1998, **129**, 41-51.
29. S. D. Senanayake and D. R. Mullins, *Journal of Physical Chemistry C*, 2008, **112**, 9744-9752.
30. X. D. Peng and M. A. Barteau, *Langmuir*, 1991, **7**, 1426-1431.
31. D. A. Outka and R. J. Madix, *Surface Science*, 1987, **179**, 361-376.
32. C. H. Lin, C. L. Chen and J. H. Wang, *Journal of Physical Chemistry C*, 2011, **115**, 18582-18588.
33. G. Jacobs, P. M. Patterson, U. M. Graham, A. C. Crawford and B. H. Davis, *International Journal of Hydrogen Energy*, 2005, **30**, 1265-1276.
34. A. A. Gokhale, J. A. Dumesic and M. Mavrikakis, *Journal of the American Chemical Society*, 2008, **130**, 1402-1414.
35. C. T. Liu, M. Chen, C. Y. Du, J. Zhang, G. P. Yin, P. F. Shi and Y. R. Sun, *International Journal of Electrochemical Science*, 2012, **7**, 10592-10606.
36. C. Rice, S. Ha, R. I. Masel and A. Wieckowski, *Journal of Power Sources*, 2003, **115**, 229-235.
37. X. W. Yu and P. G. Pickup, *Journal of Power Sources*, 2011, **196**, 7951-7956.
38. Y. H. Pan, R. M. Zhang and S. L. Blair, *Electrochemical and Solid State Letters*, 2009, **12**, B23-B26.
39. N. M. Markovic and P. N. Ross, *Surface Science Reports*, 2002, **45**, 121-229.
40. X. W. Yu and P. G. Pickup, *Journal of Power Sources*, 2008, **182**, 124-132.
41. J. H. Choi, K. J. Jeong, Y. Dong, J. Han, T. H. Lim, J. S. Lee and Y. E. Sung, *Journal of Power Sources*, 2006, **163**, 71-75.
42. N. P. Brandon, S. Skinner and B. C. H. Steele, *Annual Review of Materials Research*, 2003, **33**, 183-213.
43. J. B. Xu, T. S. Zhao and Z. X. Liang, *Journal of Power Sources*, 2008, **185**, 857-861.
44. S. Zhang, Y. Y. Shao, G. P. Yin and Y. H. Lin, *Journal of Power Sources*, 2010, **195**, 1103-1106.
45. M. Haruta, T. Kobayashi, H. Sano and N. Yamada, *Chemistry Letters*, 1987, 405-408.
46. G. J. Hutchings, *Journal of Catalysis*, 1985, **96**, 292-295.
47. J. Sa, A. Goguet, S. F. R. Taylor, R. Tiruvalam, C. J. Kiely, M. Nachtegaal, G. J. Hutchings and C. Hardacre, *Angewandte Chemie-International Edition*, 2011, **50**, 8912-8916.
48. J. Guzman and B. C. Gates, *Nano Letters*, 2001, **1**, 689-692.
49. T. V. W. Janssens, B. S. Clausen, B. Hvolbaek, H. Falsig, C. H. Christensen, T. Bligaard and J. K. Norskov, *Topics in Catalysis*, 2007, **44**, 15-26.
50. J. L. Gong, *Chemical Reviews*, 2012, **112**, 2987-3054.
51. R. Coquet, K. L. Howard and D. J. Willock, *Chemical Society Reviews*, 2008, **37**, 2046-2076.
52. R. J. Davis, *Science*, 2003, **301**, 926-927.

53. G. C. Bond and D. T. Thompson, *Catalysis Reviews-Science and Engineering*, 1999, **41**, 319-388.
54. A. S. K. Hashmi and G. J. Hutchings, *Angewandte Chemie-International Edition*, 2006, **45**, 7896-7936.
55. J. Guzman, B. G. Anderson, C. P. Vinod, K. Ramesh, J. W. Niemantsverdriet and B. C. Gates, *Langmuir*, 2005, **21**, 3675-3683.
56. N. Yi, H. Saltsburg and M. Flytzani-Stephanopoulos, *Chemsuschem*, 2013, **6**, 816-819.
57. M. Ojeda and E. Iglesia, *Angew. Chem. Int. Ed.*, 2009, **48**, 4800-4803.
58. A. Gazsi, T. Bansagi and F. Solymosi, *Journal of Physical Chemistry C*, 2011, **115**, 15459-15466.
59. B. Hammer, L. B. Hansen and J. K. Norskov, *Physical Review B*, 1999, **59**, 7413-7421.
60. J. Greeley, J. K. Norskov and M. Mavrikakis, *Annu Rev Phys Chem*, 2002, **53**, 319-348.
61. J. Neugebauer and M. Scheffler, *Physical Review B*, 1992, **46**, 16067-16080.
62. L. Bengtsson, *Physical Review B*, 1999, **59**, 12301-12304.
63. D. J. Chadi and M. L. Cohen, *Physical Review B*, 1973, **8**, 5747-5753.
64. H. J. Monkhorst and J. D. Pack, *Physical Review B*, 1976, **13**, 5188-5192.
65. D. Vanderbilt, *Phys Rev B Condens Matter*, 1990, **41**, 7892-7895.
66. J. P. Perdew, J. A. Chevary, S. H. Vosko, K. A. Jackson, M. R. Pederson, D. J. Singh and C. Fiolhais, *Phys Rev B Condens Matter*, 1992, **46**, 6671-6687.
67. J. A. White and D. M. Bird, *Phys Rev B Condens Matter*, 1994, **50**, 4954-4957.
68. G. Kresse and J. Furthmuller, *Computational Materials Science*, 1996, **6**, 15-50.
69. J. Donohue, Wiley, New York, 1974, p. 222.
70. G. Henkelman, B. P. Uberuaga and H. Jonsson, *Journal of Chemical Physics*, 2000, **113**, 9901-9904.
71. G. Henkelman and H. Jonsson, *Journal of Chemical Physics*, 2000, **113**, 9978-9985.
72. J. Greeley and M. Mavrikakis, *Surface Science*, 2003, **540**, 215-229.
73. L. C. Grabow and M. Mavrikakis, *ACS Catal.*, 2011, **1**, 365-384.
74. J. A. Dumesic, A. A. Gokhale, S. Kandoi, J. P. Greeley and M. Mavrikakis, *Chemical Engineering Science*, 2004, **59**, 4679-4691.
75. L. C. Grabow, A. A. Gokhale, S. T. Evans, J. A. Dumesic and M. Mavrikakis, *J. Phys. Chem. C*, 2008, **112**, 4608-4617.
76. S. D. Chakarova-Kack, E. Schroder, B. I. Lundqvist and D. C. Langreth, *Physical Review Letters*, 2006, **96**, 4.
77. J. Sauer, P. Ugliengo, E. Garrone and V. R. Saunders, *Chemical Reviews*, 1994, **94**, 2095-2160.
78. N. Lopez, T. Janssens, B. Clausen, Y. Xu, M. Mavrikakis, T. Bligaard and J. Norskov, *Journal of Catalysis*, 2004, **223**, 232-235.
79. H. Chaoquan, T. Siu-Wa, C. Kwong-Yu and H. Wei, *International Journal of Hydrogen Energy*, 2012, **37**, 15956-15965.
80. Y. L. Yu, X. Wang and K. H. Lim, *Catalysis Letters*, 2011, **141**, 1872-1882.
81. C. T. Campbell and K. A. Daube, *Journal of Catalysis*, 1987, **104**, 109-119.
82. T. Vanherwijnen and W. A. Dejong, *Journal of Catalysis*, 1980, **63**, 83-93.

83. J. F. Edwards and G. L. Schrader, *Journal of Physical Chemistry*, 1984, **88**, 5620-5624.
84. M. Bowker, R. A. Hadden, H. Houghton, J. N. K. Hyland and K. C. Waugh, *Journal of Catalysis*, 1988, **109**, 263-273.
85. S. G. Neophytides, A. J. Marchi and G. F. Froment, *Applied Catalysis a-General*, 1992, **86**, 45-64.
86. B. Sakakini, J. Tabatabaei, M. J. Watson, K. C. Waugh and F. W. Zemicael, *Faraday Discussions*, 1996, **105**, 369-376.
87. S. D. Senanayake, D. Stacchiola, P. Liu, C. B. Mullins, J. Hrbek and J. A. Rodriguez, *Journal of Physical Chemistry C*, 2009, **113**, 19536-19544.
88. F. C. Meunier, D. Reid, A. Goguet, S. Shekhtman, C. Hardacre, R. Burch, W. Deng and M. Flytzani-Stephanopoulos, *Journal of Catalysis*, 2007, **247**, 277-287.
89. K. Nishimura, K. Kunimatsu, K. Machida and M. Enyo, *Journal of Electroanalytical Chemistry*, 1989, **260**, 181-192.
90. Y. Chen, J. Cheng, P. Hu and H. F. Wang, *Surface Science*, 2008, **602**, 2828-2834.
91. S. Duan, Y. F. Ji, P. P. Fang, Y. X. Chen, X. Xu, Y. Luo and Z. Q. Tian, *Physical Chemistry Chemical Physics*, 2013, **15**, 4625-4633.
92. W. H. Zhong, Y. X. Liu and D. J. Zhang, *Journal of Physical Chemistry C*, 2012, **116**, 2994-3000.
93. J. Greeley and M. Mavrikakis, *Journal of Physical Chemistry B*, 2005, **109**, 3460-3471.
94. S. C. Huang, C. H. Lin and J. H. Wang, *Journal of Physical Chemistry C*, 2010, **114**, 9826-9834.
95. D. G. Barton and S. G. Podkolzin, *Journal of Physical Chemistry B*, 2005, **109**, 2262-2274.
96. D. C. Ford, A. U. Nilekar, Y. Xu and M. Mavrikakis, *Surface Science*, 2010, **604**, 1565-1575.
97. S. Jalili, A. Z. Isfahani and R. Habibpour, *Computational and Theoretical Chemistry*, 2012, **989**, 18-26.
98. Y. Xu and M. Mavrikakis, *J. Phys. Chem. B*, 2003, **107**, 9298-9307.
99. F. Mehmood, A. Kara, T. S. Rahman and C. R. Henry, *Physical Review B*, 2009, **79**, 6.
100. R. A. Ojifinni, N. S. Froemming, J. Gong, M. Pan, T. S. Kim, J. M. White, G. Henkelman and C. B. Mullins, *Journal of the American Chemical Society*, 2008, **130**, 6801-6812.
101. S. P. Liu, P. Jin, D. H. Zhang, C. Hao and X. M. Yang, *Applied Surface Science*, 2013, **265**, 443-451.
102. Q. Y. Bi, X. L. Du, Y. M. Liu, Y. Cao, H. Y. He and K. N. Fan, *Journal of the American Chemical Society*, 2012, **134**, 8926-8933.
103. L. C. Grabow, B. Hvolbaek and J. K. Norskov, *Topics in Catalysis*, 2010, **53**, 298-310.
104. .
105. Q. Fu, A. Weber and M. Flytzani-Stephanopoulos, *Catalysis Letters*, 2001, **77**, 87-95.

106. W. L. Deng, J. De Jesus, H. Saltsburg and M. Flytzani-Stephanopoulos, *Applied Catalysis a-General*, 2005, **291**, 126-135.
107. B. C. Gates, *Chemical Communications*, 2013, **49**, 7876-7877.
108. C. T. Campbell, *Journal of Catalysis*, 2001, **204**, 520-524.
109. C. T. Campbell, *Topics in Catalysis*, 1994, **1**, 353-366.
110. J. A. Dumesic, *Journal of Catalysis*, 1999, **185**, 496-505.
111. M. Shekhar, J. Wang, W. S. Lee, W. D. Williams, S. M. Kim, E. A. Stach, J. T. Miller, W. N. Delgass and F. H. Ribeiro, *J. Am. Chem. Soc.*, 2012, **134**, 4700-4708.
112. M. Shekhar, J. Wang, W.-S. Lee, M. Cem Akatay, E. A. Stach, W. Nicholas Delgass and F. H. Ribeiro, *Journal of Catalysis*, 2012, **293**, 94-102.
113. W. D. Williams, M. Shekhar, W. S. Lee, V. Kispersky, W. N. Delgass, F. H. Ribeiro, S. M. Kim, E. A. Stach, J. T. Miller and L. F. Allard, *J. Am. Chem. Soc.*, 2010, **132**, 14018-14020.
114. A. Sanchez, S. Abbet, U. Heiz, W. Schneider, H. Hakkinen, R. Barnett and U. Landman, *Journal of Physical Chemistry a*, 1999, **103**, 9573-9578.
115. W. Jinlan, W. Guanghou and Z. Jijun, *Physical Review B (Condensed Matter and Materials Physics)*, 2002, **66**, 035418/035411-035418/035416.
116. J. C. Idrobo, W. Walkosz, S. F. Yip, S. Ogut, J. Wang and J. Jellinek, *Physical Review B*, 2007, **76**, 12.
117. R. Ferrando, A. Fortunelli and R. L. Johnston, *Physical Chemistry Chemical Physics*, 2008, **10**, 640-649.
118. D. Marx and J. Hutter, *Modern methods and algorithms of quantum chemistry*, 2000, **1**, 301-449.
119. Y. Zhai, D. Pierre, R. Si, W. Deng, P. Ferrin, A. U. Nilekar, G. Peng, J. A. Herron, D. C. Bell, H. Saltsburg, M. Mavrikakis and M. Flytzani-Stephanopoulos, *Science*, 2010, **329**, 1633-1636.
120. C. Mager-Maury, C. Chizallet, P. Sautet and P. Raybaud, *Acs Catalysis*, 2012, **2**, 1346-1357.
121. S. Singh, S. Li, R. Carrasquillo-Flores, A. C. Alba-Rubio, J. A. Dumesic and M. Mavrikakis, *Aiche Journal*, 2014, **60**, 1303-1319.

Chapter 7: Reverse Water-Gas Shift on Interfacial Sites Formed by Deposition of Oxide Moieties onto Au Nanoparticles

7.1 Introduction

In this chapter the discussion of supported Au catalysts will be continued. In Chapter 6, the choice of the inert support, SiC, made it possible to disregard contributions to the reaction rates from the support and any interfacial active sites and therefore assign all the reactivity to the metallic Au sites. However, support materials are usually metal-oxides that can affect the surface reactions and in many cases play a great role in the selectivity and overall activity. In light of this, the study of Au catalysts should focus on studying the reactivity and state of the metal functionality as well as the metal-support interaction to truly understand the origin of the catalytic activity on supported Au catalysts.

Activation of reactants at the Au-metal oxide interface is widely proposed to be a key step for reactions such as H_2 dissociation,[1, 2] CO oxidation[3-8], WGS, and reverse water-gas shift (RWGS).[9-18] Rodriguez *et al.* studied WGS over Au/TiO_2(110), and on the basis of experiments and theoretical calculations they concluded that the metal-support interface is critical for the activation of water and the formation of a carboxyl intermediate which further decomposes into CO_2 and H_2.[10] Ribeiro and co-workers elucidated the effect of the interface on water activation and determined that the WGS reaction rate scales linearly with the number of under-coordinated Au atoms, estimated from physical models of Au clusters and particle size measurements.[19, 20] Under-coordinated perimeter and corner sites were found to dominate the reactivity, with corner sites being more active than perimeter sites.[20] These studies illustrate the importance of

determining the number of sites at the Au-metal oxide interface. Accordingly, in the present work we have explored an approach to identify and quantitatively assess the metallic and interfacial active sites involved in the RWGS reaction over supported Au catalysts. In these studies, we have used Au/SiO_2 catalysts to study the activity of under-coordinated Au sites, and we then have modified these catalysts with molybdenum oxide moieties using a recently described synthesis approach based on controlled surface reactions (CSR).[21] Using this methodology, Hakim *et al.* demonstrated it is possible to uniformly deposit Mo moieties on supported Pt nanoparticles with negligible deposition on the support.

Previous research has demonstrated that under-coordinated sites are involved in the chemistry for the majority of Au-catalyzed reactions, whereas the more close-packed facets are generally inert.[2, 19, 20, 22-28] Therefore, we hypothesize that the deposition of Mo will selectively occur on these under-coordinated sites during CSR to prepare AuMo catalysts. To study this hypothesis, we have utilized a variety of characterization tools to probe the effect of Mo on the reactivity of the catalyst, the state of Au and Mo, and the number of active sites under different conditions. Our results provide insight into the nature of the active sites on Au catalysts for RWGS, and in a more general sense, this work demonstrates the efficacy of CSR for AuMo catalysts to quantify and probe the activity of Au and interfacial sites.

7.2 Methods and Materials

7.2.1 Catalyst Preparation

A 4 wt% Au/SiO_2 catalyst was prepared by deposition-precipitation. 2.0 g of dry silica (Cab-o-Sil EH-5) was dispersed in 400 mL of a 2 mM chloroauric acid (Sigma-

Aldrich) solution at room temperature. The pH of the mixture was adjusted to 9 by drop-wise addition of 2.5 M ammonium hydroxide (Sigma-Aldrich). The mixture was aged for 6 h under stirring at room temperature, and the solid material was then filtered and washed with deionized water to remove chloride ions. The sample was dried overnight at 373 K in air. The dried catalyst was reduced in a flow-through cell at a temperature of 623 K (with a heating rate of 2 K min^{-1}) under hydrogen flow (30 cm^3 (STP) min^{-1}) for 4 h. The reduced sample was then transferred to an inert atmosphere glove box. AuMo/SiO_2 catalysts were prepared by a modified CSR method.[21] A solution of cycloheptatriene molybdenum tricarbonyl (Strem Chemicals) in n-pentane (1 mg precursor/g solvent) was added to the 4 wt% Au/SiO_2 catalyst inside the glove box. The mixture was stirred for 2 h inside the glove box and transferred to a vacuum oven where the sample was dried overnight at 318 K. The dried sample was stored inside the glove box until use. Hereafter, AuMo/SiO_2 samples will be referred to as AuMo X, where X = the Mo/Au atomic ratio. Mo/SiO_2 samples were prepared by depositing the organometallic Mo precursor following the same method as for AuMo/SiO_2.

7.2.2 Reactivity Measurements

RWGS reaction studies were conducted in a fixed-bed down-flow reactor containing 10-15 mg of catalyst packed between quartz wool and silica chips in a 1/4-inch outer diameter stainless steel tube. Control experiments without catalyst determined there was no reactivity from the packing materials and the reactor. The total pressure in the reactor was maintained at 8.1 bar using a back-pressure regulator. Catalysts were heated (2 K min^{-1}) in RWGS flowing gas mixture (H_2:CO_2 2:1 15 cm^3 STP min^{-1}) to the reaction temperature at 573 K. After the reactivity measurements were performed, the

reactor was cooled to room temperature and then calcined in flowing air at 573 K for 4 h (2 K min^{-1}) and again cooled to room temperature. RWGS reactivity measurements were then carried out at the same conditions as above. The temperature was measured using a K-type thermocouple attached to the outside of the reactor. The temperature of the reactor was adjusted by using a furnace connected to a variable autotransformer, which was controlled with a temperature controller. The reaction temperature was maintained at 573 K and conversions were maintained below 5% to achieve differential reactor operation. The flow rates for the reactant gases CO_2 and H_2 were fixed using calibrated mass-flow meters (Cole-Parmer FF-32907-59). Research grade CO_2 and ultra-high purity H_2 (Airgas) were used. The composition of the product gases was analyzed by an online gas chromatograph with a barrier discharge ionization detector (GC-BID) system equipped with an auto-sampling 6-port valve (Shimadzu). The BID uses helium plasma to detect permanent gases such as CO_2, CO, H_2 with high sensitivity. The GC-BID system was calibrated using Scott specialty gases (P/N 34507 and 34512).

7.2.3 Fourier Transform Infrared Spectroscopy

Catalyst samples were pressed into self-supporting pellets using a 1.2 cm die. Au/SiO_2 and $AuMo/SiO_2$ pellets were fixed in the sample holder of a transmission cell described elsewhere.[29] The cell was sealed and the sample was activated in a flowing RWGS gas mixture (H_2:CO_2 2:1) for 4 h at 573 K (2 K min^{-1}). After activation the sample was cooled under RWGS flow to room temperature then evacuated to 10^{-5} Torr and a background scan was recorded. Fourier transform infrared (FTIR) (Nicolet 6700) spectra of adsorbed CO were obtained in transmission mode in the presence of 1% CO in He (Airgas). The spectra were collected at temperatures ranging from 148 to 383 K, and

the cell was allowed to equilibrate for 5 min at each individual temperature. After the FTIR measurements were performed, the cell was evacuated and the same pellet was exposed to flowing air. The sample was calcined in air for 4 h at 573 K (2 K min^{-1}) and cooled to room temperature. The sample was reactivated in RWGS flow and analyzed as described above. The temperature was measured by a type-K thermocouple and heating was controlled by a PID controller (Love Controls Series 16A) connected to a variable autotransformer. The sample holder is designed for collecting spectra at sub-ambient temperatures using flowing liquid nitrogen, as described previously.[29] All data were collected by averaging 256 scans with a resolution of 4 cm^{-1}. Spectral deconvolutions were performed using Origin 9.1 to determine the areal contribution from each peak. The final spectrum of CO adsorbed on each catalyst could be represented by two superimposed Gaussian curves.

7.2.4 Raman Spectroscopy

Raman spectroscopy experiments were carried out using a high-performance Renishaw InVia Raman Spectrometer with a 325 nm (excitation) laser. The laser is a Kimmon IK3201R-F laser with an output of 20 mW and an approximate power of 4 mW at the sample. All measurements used a 2400, l mm^{-1} grating with an efficiency of approximately 30 % at 325 nm. *In situ* Raman studies used an OFR near-UV objective with 15x magnification and a working distance of 8.5 mm. Scattered light was filtered into a UV enhanced (lumogen coated) deep depleted array detector (Renishaw). The laser line was calibrated with a Ne calibration lamp. In addition to calibrating the laser, the Raman spectrograph was calibrated to a diamond standard at 1332 cm^{-1}. Raman measurements were taken over a range of 100-1200 cm^{-1} and a dispersion of 1.36565 cm^{-}

^{1} pixel^{-1}. *In situ* measurements were taken using a fully open aperture and an exposure time of 360 s, with four accumulations. Approximately 10 mg of sample was used for each *in situ* experiment. Experiments were performed in a high-temperature cell (Linkam CCR1000) designed for temperatures up to 1273 K using a quartz window with water-cooled O-rings. The temperature was controlled by a Linkam T95-HT system. Gas flows during *in situ* experiments were controlled by mass flow controllers (Bronkhorst EL-Flow) with maximum flow rates of 50, 100, and 40 cm^3 (STP) min^{-1} for hydrogen, helium, and oxygen/carbon dioxide, respectively. The mass flow controllers were connected to a digital readout system (Bronkhorst series E-7000) capable of mixing gases with variable flow rates. Catalysts were first activated for 2 h at 573 K (10 K min^{-1}), under RWGS flow (H_2:CO_2 2:1 15 cm^3 STP min^{-1}). The cell was then flushed with He for 10 minutes, and the sample was oxidized at 573 K under a flow of 16 cm^3 min^{-1} He (Airgas, UHP) and 4 cm^3 min^{-1} O_2 (Airgas, Research Grade). The sample was oxidized for two hours prior to obtaining a Raman spectrum. Samples were kept at 573 K for spectra acquisition.

7.2.5 Scanning Transmission Electron Microscopy

Particle size distributions were determined using Image J software to analyze micrographs obtained by scanning transmission electron microscopy (STEM), with at least 1000 nanoparticles considered for each analysis. Images were recorded with an FEI Titan scanning transmission electron microscope with a C_s probe aberration corrector operated at 200 kV with spatial resolution < 0.1 nm. The high-angle annular dark-field (HAADF) mode was used, with a HAADF detector angle ranging from 54 to 270 mrad, probe convergence angle of 24.5 mrad, and probe current of ~25 pA. Energy-dispersive

X-ray spectroscopy (EDS) results were obtained with a convergence angle of 24.5 mrad and beam current of 640 pA, with a spatial resolution of 0.5 nm. To prepare samples for STEM, the catalysts were previously activated in a Schlenk tube under RWGS flow at 573 K, cooled to room temperature, sealed, and then opened in a glove box under N_2 atmosphere to avoid contact with air. The samples were then suspended in ethanol and deposited on carbon-coated copper grids in a N_2 atmosphere. This procedure was previously reported to be an effective method to avoid leaching of oxidized oxophilic components into solution during the ethanol suspension process.[21] STEM samples were plasma cleaned for 15 min before loading into the microscope.

7.2.6 X-Ray Absorption Spectroscopy

Au L-edge (11.919 keV) and Mo K-edge (20.000 keV) x-ray absorption spectroscopy (XAS) measurements were performed on the beam lines of the Materials Research Collaborative Access Team (MRCAT, 10-BM and 12-BM) at the Advanced Photon Source (APS) at Argonne National Laboratory. Ionization chambers were optimized to provide maximum current with a linear response (~10^{10} photons detected s^{-1}). The x-ray beam was 0.25 mm^2 and data were collected in both transmission and fluorescence modes. A third detector in series was used to collect simultaneously a foil reference spectrum with each measurement for energy calibration. All catalysts were pretreated in a continuous-flow reactor, consisting of a quartz tube (1 inch OD, 10 inch length) sealed with Kapton windows by two Ultra-Torr fittings. A ball valve was welded to each Ultra-Torr fitting to enable gas flow through the reactor. An internal type-K thermocouple was fixed against the catalyst sample holder to monitor temperature. Catalyst samples were pressed into a cylindrical sample holder consisting of six wells,

each forming a self-supporting pellet. The mass of catalyst was selected to give an absorbance of approximately 1.0. The catalysts were reduced in flowing 3.5% H_2 in He (50 cm^3 (STP) min^{-1}) at 573 K, purged with flowing He for 10 min and then cooled to room temperature. Calcination treatments were performed by flowing air at 573 K, cooling to room temperature and performing the reduction procedure detailed above. XAS spectra were collected for the reduced samples before and after calcination. Traces of oxygen and moisture in the H_2 and He were removed by means of a purifier (Matheson PUR-Gas Triple Purifier Cartridge).

7.3 Results and Discussion

7.3.1 Infrared Spectroscopy

To gain insight into the nature of the surface sites present on the various catalysts, FTIR spectra were collected of CO adsorbed on Au and AuMo catalysts over a wide range of temperatures. The spectra in Figure 7.1 show two features for CO adsorption on two distinct surface sites of Au/SiO_2 activated under H_2 flow at 573 K. These features have been previously observed and have been assigned to the adsorption of CO on under-coordinated Au^0 (2111 cm^{-1}) and CO on under-coordinated $Au^{\delta+}$ (2122 cm^{-1}).[30-35] The spectra at low temperature, Figure 7.1b, reveal that the majority of the sites are Au^0 when Au is activated under H_2 flow. Spectral deconvolution of the bands collected at 173 K reveals that 74% of the total sites are Au^0, assuming that the extinction coefficients of the two bands are equal. CO pressures between 3 x 10^{-3} and 9 x 10^{-3} Torr were studied, from which we obtained adsorption isotherms (Figure 7.2). From these data it is possible to identify combinations of temperature and pressure that display the same absorbance (i.e., equal surface coverage), allowing the use of isosteres to perform a Clausius-Clapeyron

analysis, Figure 7.3. The isosteric heat of CO adsorption, ΔH_{ads}, can be derived from the slope of each isostere. For both Au^0 and $Au^{\delta+}$, the value of ΔH_{ads} increases with decreasing coverage, in agreement with previous work.[30, 31] Values of ΔH_{ads} at high coverage, $\theta > 70\%$, and low coverage, $\theta = 33\%$, are reported in Table 7.1. The value of ΔH_{ads} for Au^0 increases from -18 to -31 kJ mol^{-1} from high to low coverage, respectively. For $Au^{\delta+}$, the value of ΔH_{ads} increases from -44 to -64 kJ mol^{-1}. The value of ΔS_{ads}, derived from the equilibrium constant calculated from the Langmuir isotherm, is also reported at low coverage and was calculated to be -88 J mol^{-1} K^{-1} for Au^0 and -133 J mol^{-1} K^{-1} for $Au^{\delta+}$. The changes in ΔH_{ads} due to coverage effects are consistent with other infrared studies of CO adsorption on Au.[30, 31, 36] While both of these sites experience coverage effects, the values of ΔH_{ads} and ΔS_{ads} are higher for $Au^{\delta+}$ compared to Au^0 and indicate a more localized and stronger adsorption for adsorption on the former sites. Further, the coexistence of the Au^0 and $Au^{\delta+}$ sites explains why a two-site Langmuir adsorption model can provide a better representation of CO adsorption data on Au.[20, 36] Performing the same analysis of data collected using the AuMo catalysts revealed no significant difference in the values of ΔH_{ads} and ΔS_{ads} between AuMo and Au nanoparticles, indicating that the presence of Mo does not have an effect on the energetics of CO adsorption on Au.

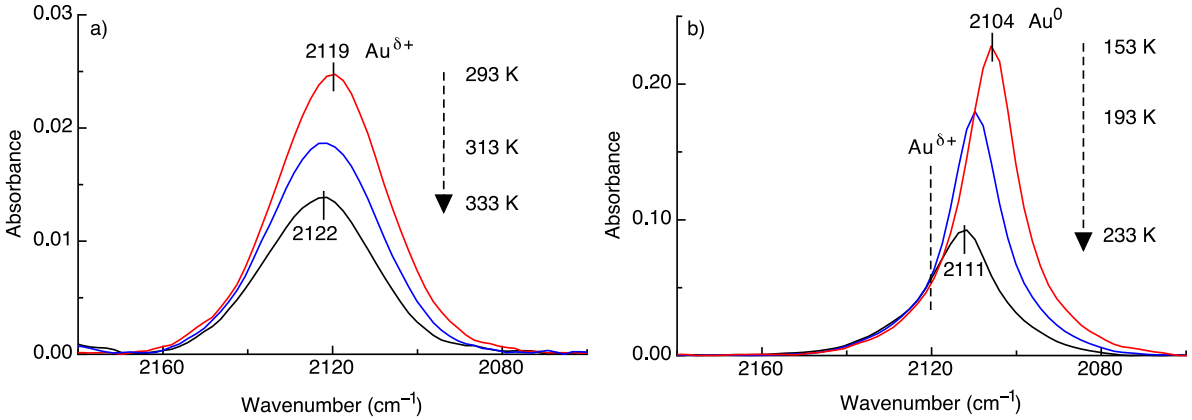

Figure 7.1. Representative IR spectra at 3 x 10^{-3} Torr of CO on Au/SiO_2 activated in flowing H_2 at 573 K, showing the a) $Au^{\delta+}$ band at temperatures higher than 293 K and the b) Au^0 and $Au^{\delta+}$ bands observed at cryogenic temperatures.

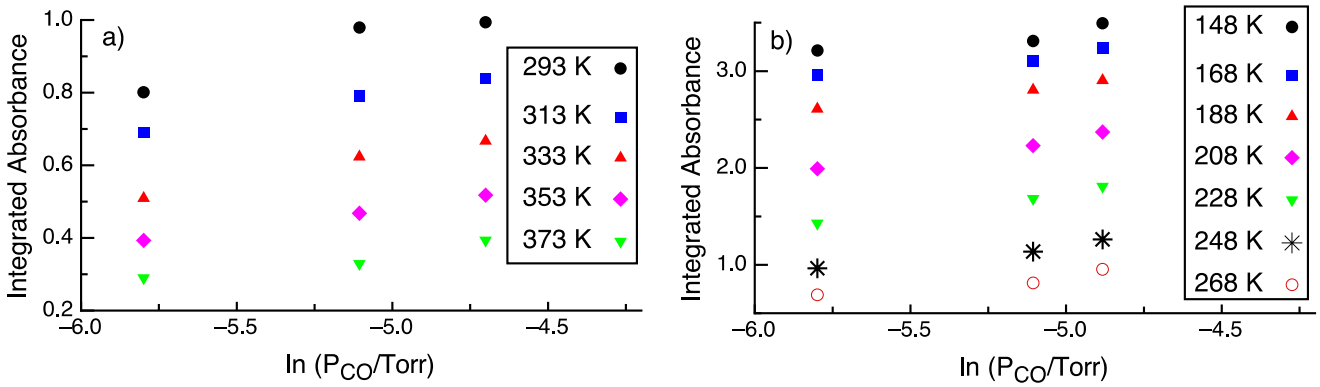

Figure 7.2. Representative CO adsorption isotherms on Au/SiO_2 activated in flowing H_2 at 573 K for the a) $Au^{\delta+}$ band and b) Au^0 band. The integrated absorbance of the Au^0 band was obtained by spectral deconvolution of the original spectrum.

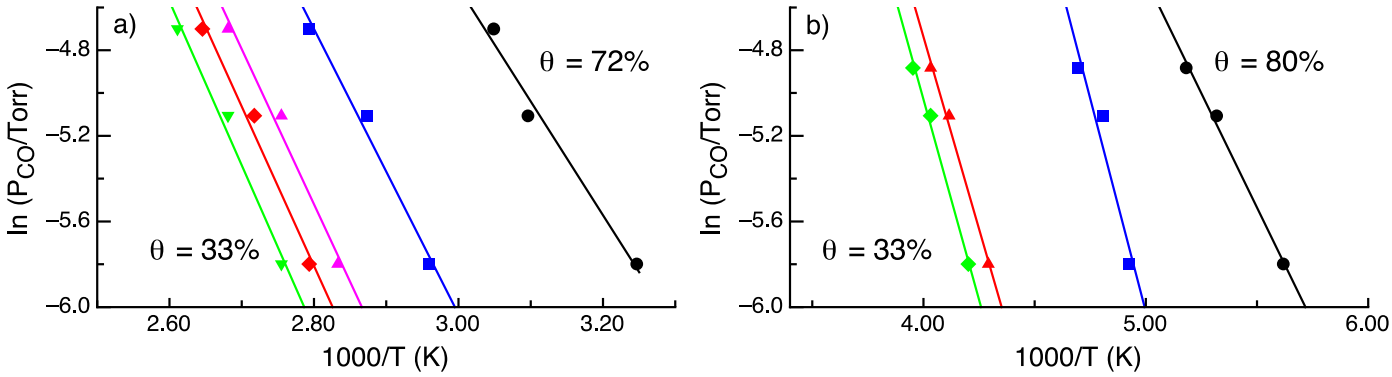

Figure 7.3. Isosteric plots for CO on Au/SiO_2 activated in flowing H_2 at 573 K for the a) $Au^{\delta+}$ band and b) Au^0 band. The surface coverage changes from left to right in a) as 33%, 36%, 40%, 49% and 72% and in b) as 33%, 36%, 63% and 80%. Constant coverage data points were identified from the full set of data represented by Figure 7.2. The coverage was calculated by normalizing the absorbance based on the maximum absorbance.

Table 7.1. Thermodynamic parameters determined by Clausius-Clapeyron treatment of CO adsorption FTIR data at a surface coverage of 33%

Site	ΔH_{ads} (kJ mol^{-1})	ΔS_{ads} (J mol^{-1} K^{-1})
Au^0	-31 ± 3 (-18 ± 1)[a]	-88 ± 3
$Au^{\delta+}$	-64 ± 8 (-44 ± 6)[a]	-133 ± 9

[a] Values in parenthesis are values of ΔH_{ads} at high coverage

FTIR spectra of the Au and AuMo catalysts activated under RWGS flow and collected at 3 $x10^{-1}$ Torr of CO are compared in Figure 7.4. For as-synthesized Au, Figure 7.4a, spectral deconvolution of the bands reveals that after RWGS activation only 10% of the sites are Au^0, in contrast with 74% for H_2 activation. This increase in the intensity of the $Au^{\delta+}$ band occurs at the expense of Au^0 sites that are oxidized from reaction with CO_2 present in the RWGS gas mixture.[34, 35, 37, 38] This behavior indicates that the original distribution of sites generated during catalyst reduction is altered under RWGS conditions. It is important to note that while these results provide insight into the nature of the working catalyst during reaction, the parent Au/SiO_2 catalyst was always pre-reduced before CSR addition of Mo, and therefore the majority of the sites are in a metallic state.

Addition of Mo to as-synthesized Au, Figure 7.4a, produces a decrease on the CO uptake at 173 K, indicating that the original number of Au sites available for CO binding has been decreased by addition of Mo. Calcination of the samples, Figure 7.4b, leads to an increase in CO uptake. One possible explanation for the increase in uptake could be a change in the Au particle morphology. Previous work has shown that O_3 treatments at cryogenic temperatures can roughen Au(111) surfaces and produce defects.[39] While O_2 is a weaker oxidizing agent than O_3, the activation of O_2 has been shown to have a lower activation barrier on step sites as opposed to extended surfaces.[40] In addition, the binding

of atomic oxygen is stronger on smaller Au nanoparticles.[41] From a particle size analysis of STEM micrographs, Figure 7.5, the average particle size was determined to be 1.7 ± 1.3 nm. Based on existing correlations,[42] the first-shell coordination number (obtained from XAS results) was used to estimate the average particle size as 1.3 nm, which is in agreement with our measurements. Therefore, it is possible that surface roughening may be facilitated by both the temperature at which we perform the calcination (573 K) and the high number of under-coordinated sites present on the small nanoparticles of the catalyst, which would account for the observed promotional effect of calcination. To further investigate the effect of the calcination, CSR of Mo onto Au (Mo:Au = 0.15) was performed using calcined Au/SiO_2 as the parent material (Figure 7.4b), as a method to increase the number of low coordination sites on the Au nanoparticles prior to deposition of Mo. The CO uptake for this catalyst was equal to that of the AuMo catalyst with Mo:Au = 0.1. This result suggests that the maximum amount of Mo that can be added to the Au/SiO_2 catalyst of the present study corresponds to Mo:Au = 0.15.

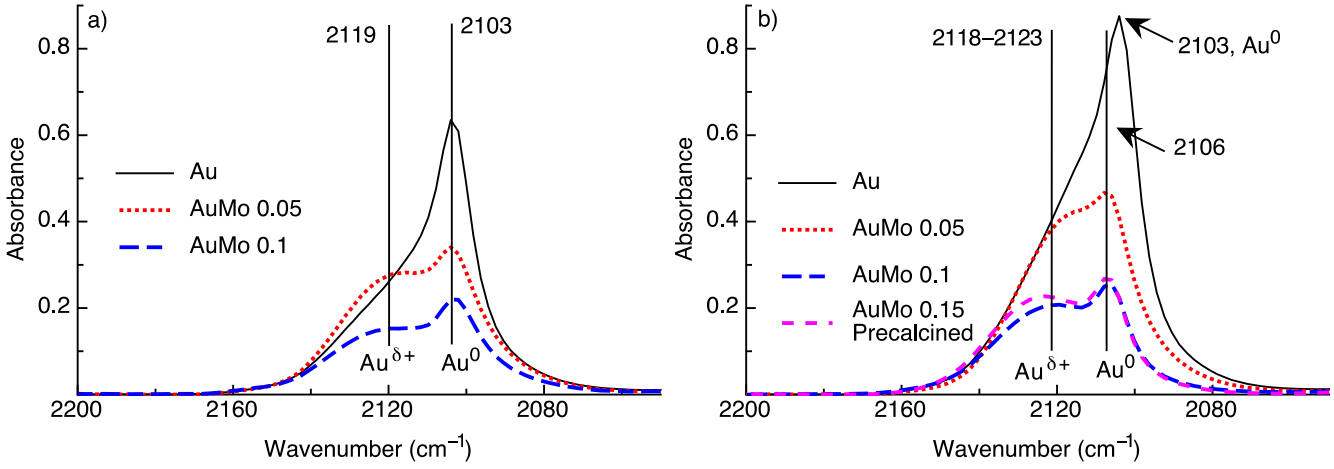

Figure 7.4. IR spectra for CO adsorbed on a) as-synthesized and b) calcined Au/SiO_2 and $AuMo/SiO_2$ at 173 K and 3 x 10^{-1} Torr of CO. The intensities are normalized by the pellet density. Catalysts were activated in flowing RWGS conditions at 573 K.

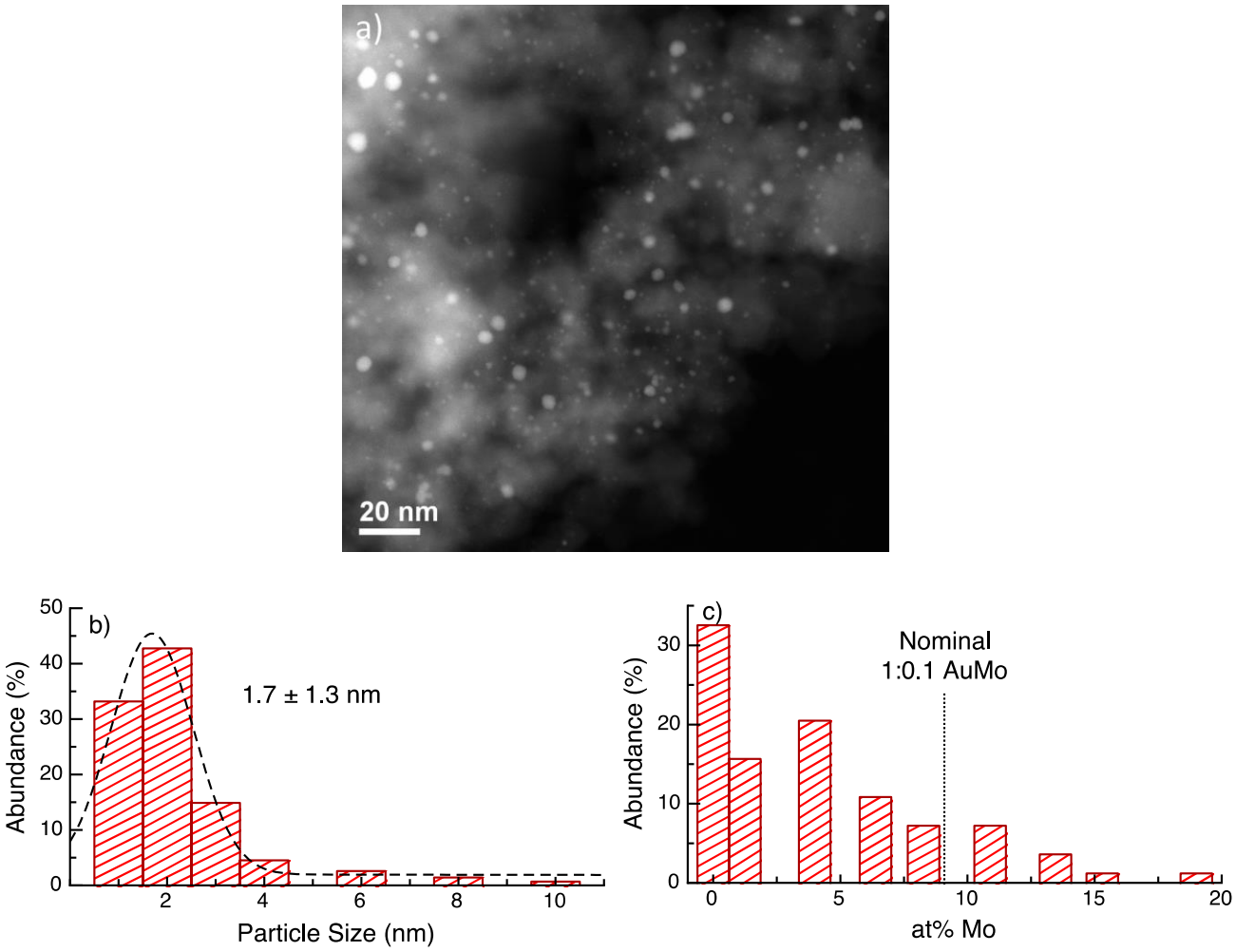

Figure 7.5. Representative a) HAADF-STEM image b) particle size distribution and c) EDS histogram of Mo content for AuMo 0.1 catalyst activated under H_2 flow.

7.3.2 Raman Spectroscopy and X-ray Absorption Spectroscopy

Figure 7.6 shows Raman spectra for all of the AuMo catalysts as well as for different Mo/SiO_2 samples. The feature at 975 cm^{-1}, present for all Mo/SiO_2 samples and increasing with Mo loading, corresponds to the symmetric stretch of $Mo(=O)_2$ from a dioxo $(O=)_2Mo(-O-Si)_2$ surface species commonly observed for samples consisting of MoO_3 dispersed on SiO_2.[43, 44] This feature is not present on SiO_2, Au/SiO_2 or the $AuMo/SiO_2$ catalysts. Furthermore, EDS analysis of the Mo content for AuMo 0.1,

Figure 7.5c, indicates that Mo species are associated with Au nanoparticles, in agreement with Raman results. Higher Mo loading samples were prepared, up to AuMo 1:0.5 (1 wt% Mo), to promote the evolution of the band. However, we did not observe the $Mo(=O)_2$ stretch even at these high Mo loadings. The presence of the $Mo(=O)_2$ stretch for the Mo/SiO_2 samples indicates that the sensitivity of the Raman spectrometer is sufficient to detect these species at the loadings employed in the present study. Importantly, the absence of this band for AuMo samples is strong evidence for the deposition of Mo on Au and not on SiO_2. Taken together with the FTIR results, these observations suggest the formation of AuMo sites via selective Mo deposition on Au.

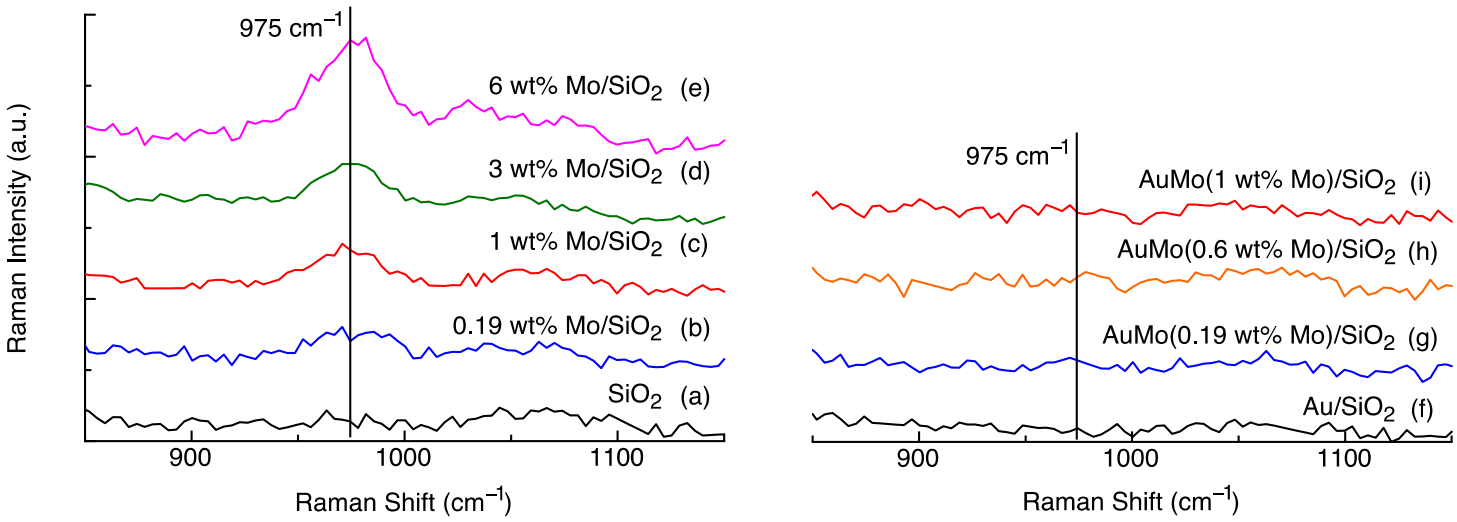

Figure 7.6. *In situ* Raman spectra (325 nm) of SiO_2 and SiO_2 supported Mo, Au and AuMo at 573 K under oxidizing conditions. The vertical line denotes the Raman shift corresponding to the symmetric stretch of a $Mo(=O)_2$ from a dioxo $(O=)_2Mo(-O-Si)_2$. (a) SiO_2, (b) 0.19 wt% Mo/SiO_2, (c) 1 wt% Mo/SiO_2, (d) 3 wt% Mo/SiO_2, (e) 6 wt% Mo/SiO_2, (f) Au/SiO_2, (g) AuMo 1:0.1, (h) AuMo 1:0.3, (i) AuMo 1:0.5.

X-ray absorption near edge spectroscopy (XANES) was used to determine the extent of Mo oxidation in the Mo/SiO_2 and $AuMo/SiO_2$ samples. Fluorescence data, Figure 7.7, were collected after the samples were calcined and reduced in H_2. According

to fits of the XANES curves, Mo in the analyzed Mo and AuMo samples is in a high oxidation state (e.g. Mo^{+6}). Importantly, this result suggests that Au and Mo exist as a metal-metal oxide combination, and not as a bimetallic alloy, as has been observed for the case of PtMo.[45] Transmission spectra for samples with higher Mo loading, Figure 7.8, indicate a slightly different behavior for these materials. In particular, when the AuMo samples are only pretreated in hydrogen, the Mo is in a slightly reduced state, existing as a mixture of Mo^{+4} and Mo^{+6}. Calcination of this same sample, however, leads to oxidation of the Mo, and only Mo^{+6} was observed. Altogether, the XANES results indicate that the Au-Mo interactions observed in FTIR and Raman spectroscopy results stem from Au-MoO_x species.

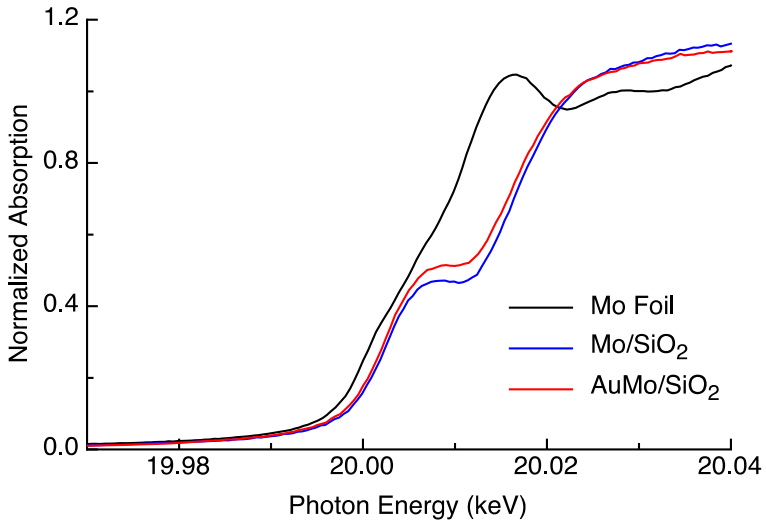

Figure 7.7. XANES fluorescence data characterizing reduced (573 K) Au/SiO_2-and $AuMo/SiO_2$ after calcination at 573 K. The Mo loading for all samples was 0.2 wt% (AuMo 0.1).

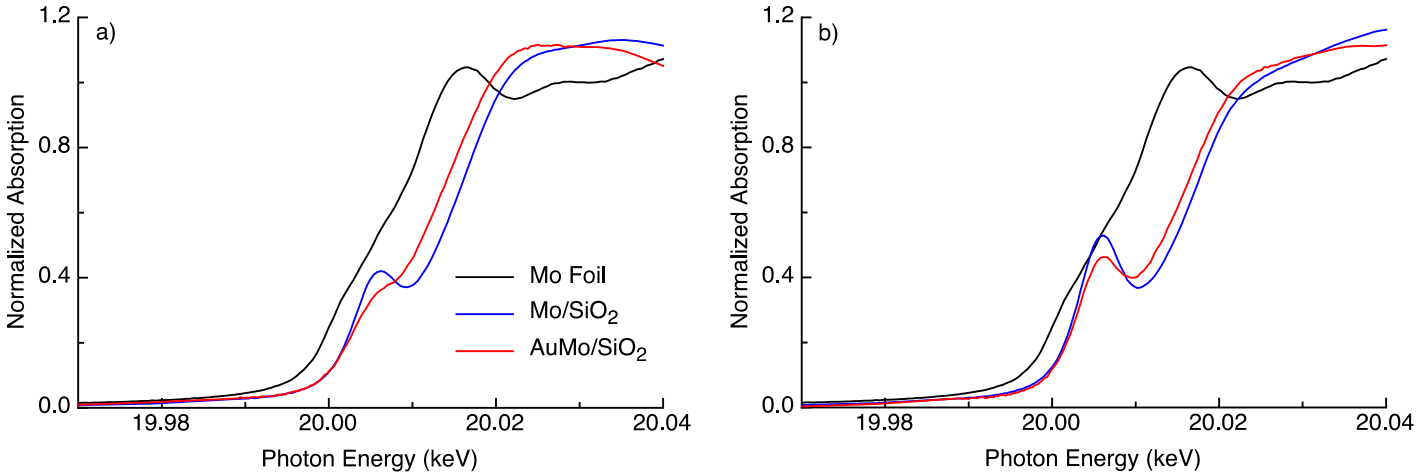

Figure 7.8. XANES transmission data characterizing reduced SiO_2-supported samples after a) reduction and b) calcination at 573 K. The Mo loading for all samples was 1 wt% (AuMo 0.5).

7.3.3 Reactivity Measurements

The catalytic properties of Au/SiO_2 and $AuMo/SiO_2$ were studied for the RWGS reaction (573 K, 8.1 bar) in a packed bed reactor. Figure 7.9 shows the reactivity of the Au and AuMo catalysts. Deposition of Mo onto Au/SiO_2 by CSR increases the rate at all Mo levels as compared to Au/SiO_2. Calcination of the catalysts increases the rate measured for all of the catalysts, but the effect of the calcination is more marked at lower Mo levels. This result agrees with the infrared measurements shown in Figure 7.4, where the CO uptake after calcination shows a higher increase at low Mo loadings. Importantly, while calcined Au shows the highest increase in the rate compared to its as-synthesized counterpart (by a factor of 3), the rate for as-synthesized AuMo 0.1 is an order of magnitude higher than that of as-synthesized Au. This result indicates that a combination of Au and interfacial AuMo sites formed during CSR is more active than Au sites alone.

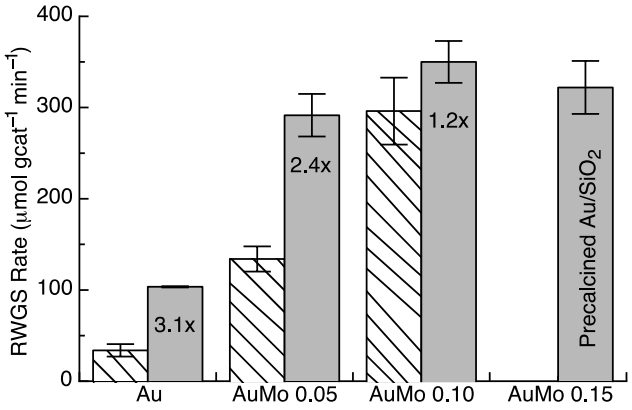

Figure 7.9. RWGS at 573 K and 8.1 bar of H_2:CO_2 (2:1) for as-synthesized (hashed bars) and calcined (gray bars) Au/SiO_2 and AuMo/SiO_2. Numbers inside the gray bars show the increase in the rate after calcination.

7.3.4 Active Sites

The FTIR, Raman, XANES and reactivity data for our catalysts provide information about the species present during synthesis conditions and reactions. First, Au sites in the studied catalysts exist in the form or Au^0 and $Au^{\delta+}$ species, and the abundance of each site is related to the conditions under which the catalyst is treated. Second, Au sites can bind Mo during our CSR method of deposition, preventing CO uptake on these sites and forming interfacial AuMo sites. Third, the Mo bound to under-coordinated Au is in a high oxidation state. And finally, a combination of Au sites and interfacial AuMo sites is more active for RWGS than Au sites alone. From this information, two types of active sites for RWGS are present and are designated as Au sites, including Au^0 and $Au^{\delta+}$, and AuMo interfacial sites. We can estimate the number of each type of site using a combination of STEM and FTIR spectroscopy of adsorbed CO. The average particle sized obtained from STEM micrographs, Figure 7.5, is 1.7 ± 1.3 nm and can be used to estimate the number of terrace, perimeter and corner sites based on physical models of Au clusters described in the literature.[20, 25, 26] It has previously been shown that WGS

activity using Au/Al_2O_3 catalysts correlated with the number of perimeter and corner sites (i.e., the number of under-coordinated sites);[8] therefore, we will assume that this value corresponds to the number of active Au sites on our catalysts. Based on this approach, the number of Au sites that adsorb CO is estimated to be 59.5 μmol $gcat^{-1}$.

Table 7.2. Results from FTIR spectroscopy of CO adsorbed on SiO_2-supported Au and AuMo catalysts

Sample	Au:Mo (mole:mole)	Pretreatment	Mo deposited (μmol□$gcat^{-1}$)	Normalized CO FTIR Area[b]	Adsorbed CO (μmol□$gcat^{-1}$)[c]
Au	1:0	RWGS	0	1	41.5
AuMo	1:0.05	RWGS	10.2	0.83	34.4
AuMo	1:0.1	RWGS	20.3	0.52	21.6
Au	1:0	Calcined	0	1.4	58.1
AuMo	1:0.05	Calcined	10.2	0.99	41.1
AuMo	1:0.1	Calcined	20.3	0.57	23.7
AuMo[a]	1:0.15	Calcined	30.5	0.63	26.1

[a] Au/SiO_2 was calcined at 573 K before Mo deposition was performed
[b] Combined integrated area of CO on Au^0 and $Au^{\delta+}$ sites.
[c] Calculated from the total number of perimeter and corner sites for a 2 nm average particle size catalyst, 41.5 μmol□$gcat^{-1}$, multiplied by the normalized CO FTIR area

An alternative approach to estimate the number of under-coordinated Au sites is to assume that the deposition of Mo occurs on these sites with a 1:1 stoichiometry. Based on the change in the integrated CO FTIR area with the addition of increasing amounts of Mo, as shown in Table 7.2, it is necessary to have approximately 40 umol $gcat^{-1}$ of under-coordinated Au sites on the as-synthesized Au/SiO_2 sample. Using this value along with the previously used particle size correlations, we estimate a Au particle size of 2 nm, which is within the error of our microscopy measurements. Using this site density we can now calibrate the area of CO absorbance in the FTIR experiments to provide an estimate for the number of under-coordinated Au sites for each catalyst, and these values are reported in Table 7.2. This analysis supports the selective deposition of Mo on under-

coordinated Au sites and in addition illustrates a method to quantify the sites on Au catalysts that is independent of particle size correlations.

Using the calculated values for the amount of adsorbed CO, the variation in the number of Au sites measured by FTIR spectra is plotted in Figure 7.10 versus the number of Mo species deposited onto the Au nanoparticles by our CSR method. These site measurements, in conjunction with the RWGS reaction rates, were then used to estimate the rate contributions from each site. The rate for each catalyst was calculated from the following equation:

$$R_{total} = S_{Au}R_{Au} + S_{AuMo}R_{AuMo}$$

Here S_{Au} is the total number of Au sites, including Au^0 and $Au^{\delta+}$, per gram of catalyst as measured by FTIR-CO measurements. Similarly, S_{AuMo} represents the number of AuMo sites (interfacial sites), as determined from the change in the amount of adsorbed CO relative to Au/SiO_2, either as-synthesized or calcined, respectively. R_{Au} and R_{AuMo} are the turnover frequencies (TOF) (mole CO produced per mole of Au or AuMo site per minute) relevant to each site. This model involved two parameters, R_{Au} and R_{AuMo}, which were linearly optimized with seven data points for $AuMo/SiO_2$ catalysts. The results from the model indicate that at the conditions studied R_{AuMo} is approximately 10 times greater than R_{Au}, where R_{AuMo} has a value of 10.4 min^{-1} and R_{Au} has a value of 1 min^{-1}. The rate predictions from our model are shown in Figure 7.11. A parity plot, indicating the goodness of the fit, is shown in Figure 7.12. Shekhar *et al.* have previously observed a similar result leading to higher rates of WGS catalyzed by Au/TiO_2 as

compared to Au/Al_2O_3.[20] Specifically, the promotion effect has been attributed to the capacity of the support/Au-support interface to activate H_2O, producing a higher coverage of hydroxyl species.[7, 20] Our Au/SiO_2 catalyst behaves much like Au/Al_2O_3 and exhibits only Au sites for RWGS, whereas our $AuMoO_x$ catalysts possess interfacial sites that complement the Au sites and are responsible for higher catalyst activity, analogous to when TiO_2 is used as the support.

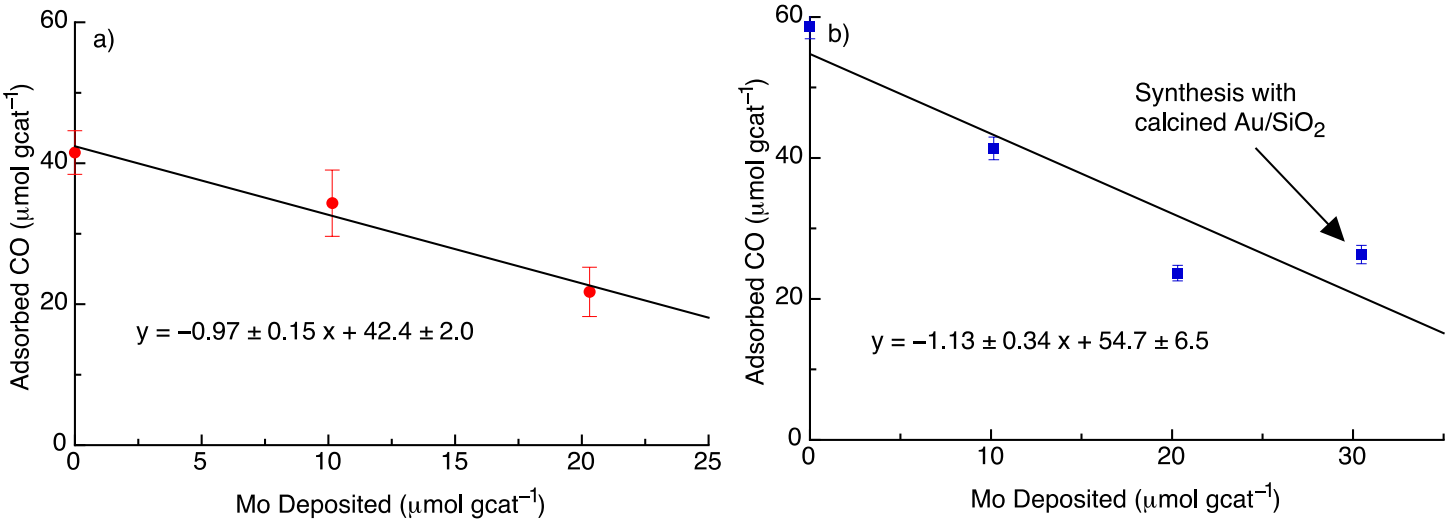

Figure 7.10. CO adsorption data for a) as-synthesized and b) calcined samples after Mo deposition.

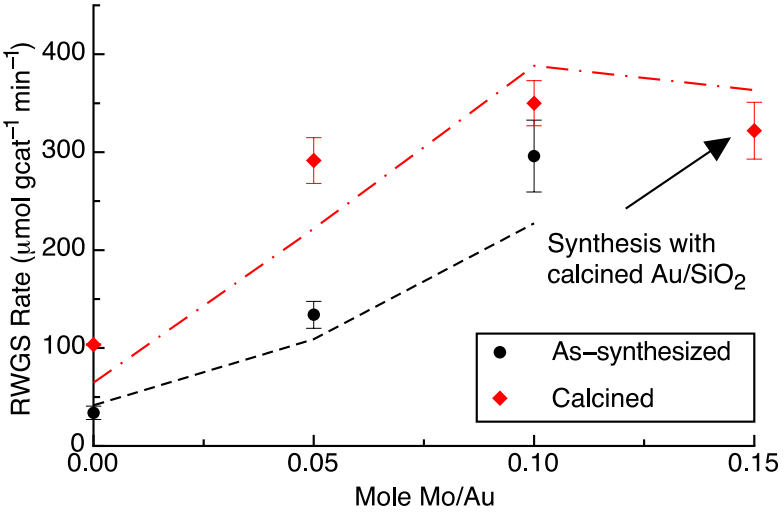

Figure 7.11. RWGS at 573 K and 8.1 bar of H_2:CO_2 (2:1) for as-synthesized and calcined Au/SiO_2 and $AuMo/SiO_2$. Dashed lines indicate the rates predicted by our model. The TOF of the AuMo sites are 10 times greater than those of Au sites. The model TOF predictions are $R_{Au} = 1\ min^{-1}$ and $R_{AuMo} = 10.4\ min^{-1}$.

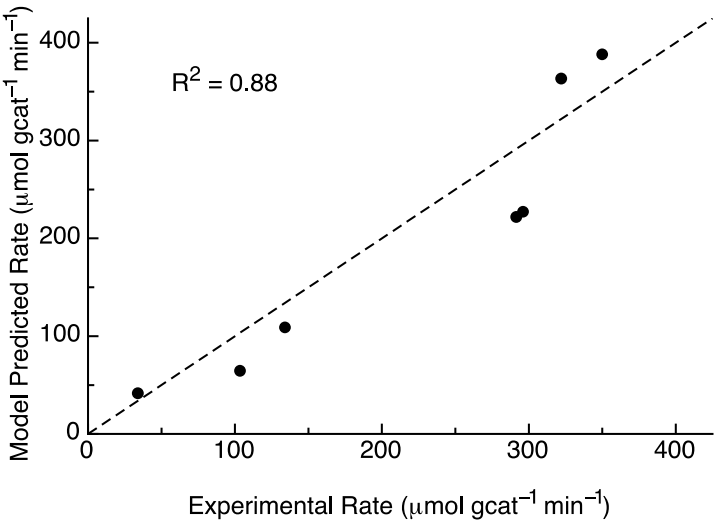

Figure 7.12. Calculated (model) versus experimental rates for the RWGS reaction.

7.4 Conclusions

Based on results from RWGS reactivity measurements, CO FTIR spectra, STEM studies, and Raman and XANES analyses, we have demonstrated that the deposition of Mo onto SiO_2 - supported Au catalysts occurs on under-coordinated sites of Au nanoparticles to form $AuMoO_x$ interfacial sites that are active for the RWGS reaction. The number of under-coordinated Au sites and the number of AuMo interfacial sites can be determined from FTIR experimental results of CO uptake, and it is shown that the interfacial sites are an order of magnitude more active than Au sites for the RWGS reaction. The presence of Au^0 and $Au^{\delta+}$ sites on Au/SiO_2 and $AuMo/SiO_2$ was observed, and it was determined that metallic sites are more abundant after reduction, whereas the oxidized sites prevail under RWGS reaction conditions. Calcination of the catalysts roughens the surface of Au nanoparticles and increases the quantity of under-coordinated Au sites, which is responsible for an increase in RWGS activity. Our strategy for catalyst synthesis by controlled deposition reactions, combined with FTIR measurements of

adsorbed CO at sub-ambient temperatures, opens the possibility for quantification of both Au active sites and the active interfacial sites. Moreover, this approach can be used to deposit small amounts of the metal-oxide moieties onto the surfaces of Au nanoparticles, demonstrating the potential for this approach to identify and ascribe changes in reactivity and selectivity observed with Au/metal-oxide catalysts for reactions where support effects may be important.

7.5 Acknowledgments

The research work presented in this chapter was submitted to the Journal of the American Chemical Society and is currently under review.

7.6 References

1. I. Nakamura, H. Mantoku, T. Furukawa and T. Fujitani, *J. Phys. Chem. C*, 2011, **115**, 16074-16080.
2. D. A. Panayotov, S. P. Burrows, J. T. Yates and J. R. Morris, *J. Phys. Chem. C*, 2011, **115**, 22400-22408.
3. L. B. Vilhelmsen and B. Hammer, *ACS Catal.*, 2014, **4**, 1626-1631.
4. M. M. Biener, J. Biener, A. Wichmann, A. Wittstock, T. F. Baumann, M. Baumer and A. V. Hamza, *Nano Lett.*, 2011, **11**, 3085-3090.
5. M. Kotobuki, R. Leppelt, D. A. Hansgen, D. Widmann and R. J. Behm, *J. Catal.*, 2009, **264**, 67-76.
6. T. Fujitani and I. Nakamura, *Angew. Chem.-Int. Ed.*, 2011, **50**, 10144-10147.
7. J. Saavedra, H. A. Doan, C. J. Pursell, L. C. Grabow and B. D. Chandler, *Science*, 2014, **345**, 1599-1602.
8. L. Li, A. Q. Wang, B. T. Qiao, J. Lin, Y. Q. Huang, X. D. Wang and T. Zhang, *Journal of Catalysis*, 2013, **299**, 90-100.
9. K. Mudiyanselage, S. D. Senanayake, L. Feria, S. Kundu, A. E. Baber, J. Graciani, A. B. Vidal, S. Agnoli, J. Evans, R. Chang, S. Axnanda, Z. Liu, J. F. Sanz, P. Liu, J. A. Rodriguez and D. J. Stacchiola, *Angew. Chem.-Int. Ed.*, 2013, **52**, 5101-5105.
10. J. A. Rodriguez, J. Evans, J. Graciani, J.-B. Park, P. Liu, J. Hrbek and J. Fdez Sanz, *J. Phys. Chem. C*, 2009, **113**, 7364-7370.
11. R. Burch, *Phys. Chem. Chem. Phys.*, 2006, **8**, 5483-5500.

12. J. B. Park, J. Graciani, J. Evans, D. Stacchiola, S. D. Senanayake, L. Barrio, P. Liu, J. F. Sanz, J. Hrbek and J. A. Rodriguez, *Journal of the American Chemical Society*, 2010, **132**, 356-363.
13. J. A. Rodriguez, S. Ma, P. Liu, J. Hrbek, J. Evans and M. Perez, *Science*, 2007, **318**, 1757-1760.
14. J. A. Rodriguez, P. Liu, J. Hrbek, J. Evans and M. Perez, *Angewandte Chemie-International Edition*, 2007, **46**, 1329-1332.
15. J. A. Rodriguez, *Catal. Today*, 2011, **160**, 3-10.
16. X. Wang, J. A. Rodriguez, J. C. Hanson, M. Perez and J. Evans, *Journal of Chemical Physics*, 2005, **123**.
17. J. A. Rodriguez, R. Liu, J. Hrbek, M. Perez and J. Evans, *Journal of Molecular Catalysis a-Chemical*, 2008, **281**, 59-65.
18. A. A. Upadhye, I. Ro, X. Zeng, H. J. Kim, I. Tejedor, M. A. Anderson, J. A. Dumesic and G. W. Huber, *Catalysis Science & Technology*, 2015, **5**, 2590-2601.
19. J. Wang, V. F. Kispersky, W. N. Delgass and F. H. Ribeiro, *J. Catal.*, 2012, **289**, 171-178.
20. M. Shekhar, J. Wang, W. S. Lee, W. D. Williams, S. M. Kim, E. A. Stach, J. T. Miller, W. N. Delgass and F. H. Ribeiro, *J. Am. Chem. Soc.*, 2012, **134**, 4700-4708.
21. S. H. Hakim, C. Sener, A. C. Alba-Rubio, T. M. Gostanian, B. J. O'Neill, F. H. Ribeiro, J. T. Miller and J. A. Dumesic, *J. Cat.*, Accepted.
22. S. Singh, S. Li, R. Carrasquillo-Flores, A. C. Alba-Rubio, J. A. Dumesic and M. Mavrikakis, *Aiche J.*, 2014, **60**, 1303-1319.
23. M. Ojeda and E. Iglesia, *Angew. Chem. Int. Ed.*, 2009, **48**, 4800-4803.
24. T. Fujitani, I. Nakamura, T. Akita, M. Okumura and M. Haruta, *Angew. Chem.-Int. Ed.*, 2009, **48**, 9515-9518.
25. M. Shekhar, J. Wang, W.-S. Lee, M. Cem Akatay, E. A. Stach, W. Nicholas Delgass and F. H. Ribeiro, *Journal of Catalysis*, 2012, **293**, 94-102.
26. W. D. Williams, M. Shekhar, W. S. Lee, V. Kispersky, W. N. Delgass, F. H. Ribeiro, S. M. Kim, E. A. Stach, J. T. Miller and L. F. Allard, *J. Am. Chem. Soc.*, 2010, **132**, 14018-14020.
27. T. Hayashi, K. Tanaka and M. Haruta, *J. Catal.*, 1998, **178**, 566-575.
28. E. E. Stangland, K. B. Stavens, R. P. Andres and W. N. Delgass, *J. Catal.*, 2000, **191**, 332-347.
29. J. Y. Shen, J. M. Hill, R. M. Watwe, B. E. Spiewak and J. A. Dumesic, *J. Phys. Chem. B*, 1999, **103**, 3923-3934.
30. D. C. Meier, V. Bukhtiyarov and A. W. Goodman, *Journal of Physical Chemistry B*, 2003, **107**, 12668-12671.
31. D. C. Meier and D. W. Goodman, *Journal of the American Chemical Society*, 2004, **126**, 1892-1899.
32. C. Ruggiero and P. Hollins, *Journal of the Chemical Society-Faraday Transactions*, 1996, **92**, 4829-4834.
33. M. L. Kottke, H. G. Tompkins and R. G. Greenler, *Surface Science*, 1972, **32**, 231-&.
34. D. J. C. Yates, *Journal of Colloid and Interface Science*, 1969, **29**, 194-&.

35. M. Mihaylov, E. Ivanova, Y. Hao, K. Hadjiivanov, B. C. Gates and H. Knozinger, *Chemical Communications*, 2008, 175-177.
36. H. Hartshorn, C. J. Pursell and B. D. Chandler, *Journal of Physical Chemistry C*, 2009, **113**, 10718-10725.
37. L. C. Wang, M. T. Khazaneh, D. Widmann and R. J. Behm, *Journal of Catalysis*, 2013, **302**, 20-30.
38. L. C. Wang, D. Widmann and R. J. Behm, *Catalysis Science & Technology*, 2015, **5**, 925-941.
39. B. K. Min, A. R. Alemozafar, D. Pinnaduwage, X. Deng and C. M. Friend, *Journal of Physical Chemistry B*, 2006, **110**, 19833-19838.
40. Y. Xu and M. Mavrikakis, *J. Phys. Chem. B*, 2003, **107**, 9298-9307.
41. V. A. Bondzie, S. C. Parker and C. T. Campbell, *Catalysis Letters*, 1999, **63**, 143-151.
42. A. I. Frenkel, C. W. Hills and R. G. Nuzzo, *Journal of Physical Chemistry B*, 2001, **105**, 12689-12703.
43. E. L. Lee and I. E. Wachs, *Journal of Physical Chemistry C*, 2007, **111**, 14410-14425.
44. E. L. Lee and I. E. Wachs, *Journal of Physical Chemistry C*, 2008, **112**, 6487-6498.
45. W. D. Williams, L. Bollmann, J. T. Miller, W. N. Delgass and F. H. Ribeiro, *Applied Catalysis B-Environmental*, 2012, **125**, 206-214.

Chapter 8: Conclusions and Future Work

8.1 Conclusions

Economic, political and environmental issues are currently driving the search for alternatives to fossil fuels in the production of fuels and chemicals. Biomass is an attractive option that is renewable and carbon-neutral and can be used to alleviate the current dependency on fossil fuels. One major challenge in the processing of biomass is the removal of excess oxygen functionalities. One possibility to accomplish this is to use hydrogen to reduce the carbon to oxygen ratio. Accordingly, this thesis focuses on strategies to efficiently convert the fractions of biomass using biomass-derived solvents and the study of heterogeneous catalysts that can be used to produce the hydrogen necessary in these conversions.

A study was performed to depolymerize the lignin present in biomass and produce a phenolic solvent. It was found that the solvent was able to extract a large portion of furanic compounds (e.g. furfural, 5-hydroxymethyl-furfural (HMF), etc.) in aqueous solutions. The affinity of the solvent for the furans was exploited using biphasic reactors where high yields for the production of furfural, HMF and levulinic acid where observed. The performance of the solvent produced in this study was comparable to other petroleum derived phenolic solvents used for these reactions.

Propyl guaiacol, a phenolic compound present in the solvent derived from lignin, was then used to perform biphasic reactions. In this case however, the biomass feedstock was processed in a ball mill depolymerizing it and producing C5 and C6 oligomers that are water-soluble. These oligomers were then converted into furfural and HMF with high yields due to the low concentrations of glucose and xylose, which are produced slowly

from the oligomers, and the prevention of product degradation into humins afforded by their isolation in the phenolic solvent.

Following the studies on biomass upgrading, the water-gas shift reaction on Pt-based catalysts was investigated. The addition of Re to Pt/C was found to increase the turnover frequency of the catalyst. Density functional theory (DFT) calculations and microkinetic modeling confirmed Pt is the main active site during the reaction. The CO coverage on the catalysts, 2/3 ML, remains unchanged after Re addition. In addition, Re is oxidized and the presence of Re facilitates the water activation step, which is the underlying rate-controlling step in the proposed mechanism for the water-gas shift reaction.

Another reaction with potential to provide renewable hydrogen is the decomposition of formic acid. We studied the decomposition of formic acid on a supported Au catalyst using DFT, experimental kinetic measurements, microkinetic modeling and electron microscopy. It was found that extended surfaces such as Au(111), Au(100) and Au(211) are largely inert for the decomposition. However, the reaction is more driven on more open, lower coordination surfaces. The reaction on Au is completely selective to the dehydrogenation products, CO_2 and H_2, and proceeds through a formate intermediate. Importantly, the reaction rate correlates with the amount of corner sites, that is the most undercoordinated sites and a highly active Au catalyst for formic acid decomposition should attempt to maximize these sites.

Finally, it was possible to study the metal-support interaction on Au catalysts in the frame of the reverse water-gas shift reaction. This was performed by depositing molybdenum moieties starting from an organometallic molybdenum precursor. CO

infrared spectroscopic measurements showed a decrease in the CO uptake indicating the deposition process occurs selectively at the undercoordinated Au sites to form interfacial sites. Raman spectroscopy confirmed the deposition of molybdenum occurs wholly on Au and not on the support. XANES spectra demonstrated Mo is in a high oxidation state and that the Au-Mo interaction is that of a metal-metal oxide pair, respectively. Quantification of the metallic and interfacial sites was performed and the results are in agreement with correlations obtained from electron microscopy particle size estimates. Importantly, the activity of the interfacial sites is an order of magnitude greater than that of the metallic sites.

The latter chapters of this thesis aim to address the disjoint between current catalyst preparation techniques and the fundamental understanding of the catalyst's moieities responsible for the high catalytic activity. Specifically, through the understanding of the complex interactions that underlie the activity observed in effective catalysts (i.e. metal, support and promoter) it will be possible to combine catalytic functionalities and produce new catalytic materials that are tailor made for a process. Overall, the goal is to promote a move "from catalyst preparation toward catalyst synthesis".

8.2 Recommendations for Future Work

8.2.1 Support Effects on Au Catalysts

The results from Chapter 7 indicate that it is possible to create localized interfacial sites on Au catalysts that can affect the catalyst activity and their formation can be monitored through a number of characterization techniques. While we have

demonstrated this using molybdenum, preliminary results using Ti and Ce show that this is not a unique effect and that other metals commonly used as metal oxide supports could be explored. This presents the opportunity to investigate support effects specific to Au catalysts that have been previously documented.

The same reaction studied in Chapter 7, the conversion of CO_2 and H_2, is coincidentally an appropriate probe reaction to the role of different supports as Sakurai and Haruta have previously shown the selection of support can shift the reaction selectivity from RWGS towards methanol production.[1] In their work they concluded that more acidic supports are more active for CO_2 conversion mainly through the RWGS reaction whereas more basic supports favor the production of methanol, where Au/ZnO and Au/Fe_2O_3 were identified as the most selective catalysts for methanol production. Interfacial sites were postulated as crucial to the observed methanol selectivities. More recently, Strunk *et al.*[2] and Hartadi *et al.*[3] have also identified the interfacial sites as the active sites for Au/ZnO catalysts. Specifically, Hartadi *et al.* proposed that Au particles could be partially covered by ZnO_x species similar to the work of Behrens *et al.* on Cu/ZnO.[4] Our synthetic protocol and characterization methods would be perfectly suited to verify these claims and provide further information on the nature of the active site for this type of catalyst as the expected final material from our synthesis would be a metal-oxide decorated Au/SiO_2 catalyst.

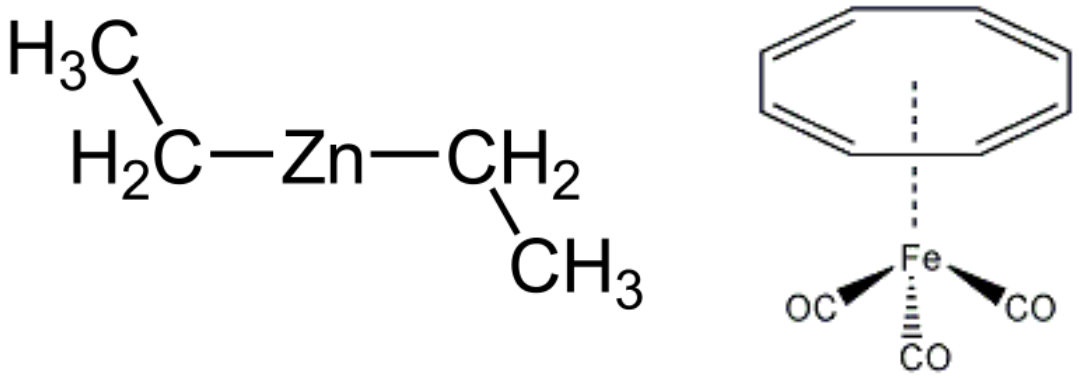

Figure 8.1. Organometallic precursors available for the synthesis of AuZn (diethylzinc (left)) and AuFe catalysts (Cyclooctatetraene iron tricarbonyl (right)).

Using organometallic precursors such as those shown in Figure 8.1 it would be possible to deposit moieities of the second metal onto the undercoordinated sites of Au/SiO_2 catalysts through controlled surface reactions. Initially, CO infrared experiments and reactivity measurements before and after deposition would suffice to assess the effectiveness of the synthesis and the effect on the selectivity and activity. The additional characterization techniques could later on be performed in order to elucidate the oxidation state of the secondary metal and to verify if any deposition takes place on the SiO_2 support. Zn and Fe have been identified as the supports that shift selectivity towards methanol most markedly, so these would be the most interesting starting points for this work. However, based on the literature, expanding the work to include other basic metal oxides could provide insight into the role of these supports for the reaction and if there is any relation between the basicity of the support and the selectivity towards methanol.

8.3 References

1. H. Sakurai and M. Haruta, *Catalysis Today*, 1996, **29**, 361-365.
2. J. Strunk, K. Kaehler, X. Y. Xia, M. Comotti, F. Schuth, T. Reinecke and M. Muhler, *Applied Catalysis a-General*, 2009, **359**, 121-128.
3. Y. Hartadi, D. Widmann and R. J. Behm, *Chemsuschem*, 2015, **8**, 456-465.

4. M. Behrens, F. Studt, I. Kasatkin, S. Kuhl, M. Havecker, F. Abild-Pedersen, S. Zander, F. Girgsdies, P. Kurr, B. L. Kniep, M. Tovar, R. W. Fischer, J. K. Norskov and R. Schlogl, *Science*, 2012, **336**, 893-897.